

UNIVERSIDADE FEDERAL DE SÃO CARLOS
CENTRO DE CIÊNCIAS EXATAS E DE TECNOLOGIA
DEPARTAMENTO DE QUÍMICA
PROGRAMA DE PÓS-GRADUAÇÃO EM QUÍMICA

**”Photoluminescence of the CaMoO_4 , MgTiO_3 and $\beta\text{-ZnMoO}_4$:
an theoretical study”**

Eduardo de Moraes

Tese apresentada como parte dos requisitos para obtenção do título de DOUTOR EM CIÊNCIAS, área de Concentração: FÍSICO-QUÍMICA.

orientador: Dr. Elson Longo
co-orientador: Dra. Valeria Longo Moraes
bolsista: CAPES

**São Carlos - SP
2015**

Ficha catalográfica elaborada pelo DePT da Biblioteca Comunitária UFSCar
Processamento Técnico
com os dados fornecidos pelo(a) autor(a)

M827p Moraes, Eduardo de
Photoluminescence of the CaMoO₄, MgTiO₃ and beta-
ZnMoO₄ : an theoretical study / Eduardo de Moraes. --
São Carlos : UFSCar, 2015.
142 p.

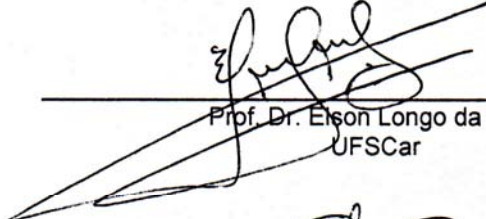
Tese (Doutorado) -- Universidade Federal de São
Carlos, 2015.

1. Fotoluminescência. 2. Ab-initio. 3. DFT. 4.
CRYSTAL - Quantum chemistry ab initio program. I.
Título.



Folha de Aprovação

Assinaturas dos membros da comissão examinadora que avaliou e aprovou a Defesa de Tese de Doutorado do candidato Eduardo de Moraes, realizada em 06/03/2015:



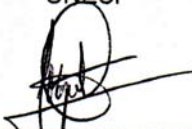
Prof. Dr. Eison Longo da Silva
UFSCar



Prof. Dr. Jose Divino dos Santos
UEG



Profa. Dr. Priscila Glauca Christianini Buzolin
UNESP



Prof. Dr. Miguel Angel San-Miguel Barrera
UNICAMP



Prof. Dr. Sergio Ricardo de Lazaro
UEPG

Da Vinci pintou uma única Mona Lisa. Beethoven compôs uma única Nona Sinfonia. E Deus fez uma única versão de você.

Max Lucado

Ao meus familiares, amigos, irmãos e meu Senhor e melhor amigo Jesus Cristo, dedico.

AGRADECIMENTOS

Quero agradecer ao meu orientador Prof Dr. Elson Longo, por todo o apoio, paciência e bom humor que tem tido comigo ao longo desses anos de doutorado. Quando cheguei em São Carlos, o Prof Elson me recebeu calorosamente e me ajudou muito, de modo que sem seu incentivo não teria conseguido fazer esse curso de doutorado.

A Prof(a) Dra. Valéria Moraes Longo por toda a ajuda e incentivo sempre com muita alegria e otimismo.

Aos queridos colegas de trabalho pela ajuda e companhia, Prof Dr. Laécio Santos Cavalcante, Prof Dr. Mario Lucio Moreira, Prof(a) Dra. Elídia Vetter Ferri, Prof(a) Dra. Tatiana Martelli Mazzo, Prof Dr. Maurício Roberto Bomio, Prof Dr. Felipe de Almeida La Porta, Prof Dr. Yuri Vinicius Bruschi de Santana, Prof(a) Dra. Cristiane Raubach Ratmann, Prof Dr. Marcio Almeida, Dra. Içamira Costa Nogueira, Dr. Julio César Sczancoski, Me. Mateus Ferrer, Ma. Amanda Fernandes Gouveia Dias, Ma. Gleice Lorena Gonçalves Tavares Botelho, Me. Francisco Nunes de Souza Neto, Me Pablo Santana Lemos, Me. Marcio Ferreira Douvel.

Aos Professores Dr. Julio Sambrano, Dr. Armando Beltrán e a Prof(a) Dra. Fernanda Gurgel pela ajuda e ensinamento.

Aos Professores da banca, Prof(a) Dra. Prescila Glaucia Christianini Buzolin, Prof Dr. José Divino dos Santos, Prof Dr. Miguel San Miguel e o Prof Dr. Sergio Ricardo de Lazaro, agradeço pela participação dessa defesa e suas contribuições.

Aos órgãos de fomento, CAPES, CNPq e FAPESP pelo apoio financeiro a mim e ao grupo de pesquisa.

Aos meus amigos e familiares que sempre me apoiaram em tudo.

Aos irmãos da igreja pela companhia e orações e finalmente a Deus pelo dom da vida e do conhecimento.

ABBREVIATION LIST

AFM - Atomic Force Microscopy

B3LYP - Becke's three-parameter hybrid nonlocal exchange functional combined with the Lee–Yang–Parr gradient-corrected correlation functional

CB - Conduction Band

CCCT - Cluster-to-Cluster Charge-Transfer

CRYSTAL - Quantum chemistry ab initio program

DFT - Density Function Theory

DOS - Density of States

DSC - Differential Scanning Calorimetry

FEG-SEM - Field-emission Gun Scanning Electron Microscopy

FT-Raman - Fourier transform Raman Absorption Spectroscopy

FT-IR - Fourier transform infrared Absorption Spectroscopy

HRTEM - High-resolution Transmission Electron Microscopy

JCPDS - Joint Committee on Powder Diffraction Standards

MH - Microwave-Hydrothermal Process

MS - Microwave-Solvothermal Processes

MTO - MgTiO₃

PL - Photoluminescence Measurements

SAED - Selected Area Electron Diffraction

STM - Scanning Tunneling Microscopy

STO - SrTiO₃

TEM - Transmission Electron Microscopy

UV-vis - Ultraviolet-visible Absorption Spectroscopy

VB - Valence Band

XANES - X-ray Absorption Near Edge Spectroscopy

XRD - Powder X-Ray Diffraction

List of Tables

2.1	Comparative Results between the Lattice Parameters and Unit Cell Volume of CaMoO_4 Obtained in This Work with Those Reported in the Literature by Different Synthesis Methods ^a	18
2.2	Atomic Coordinates Employed To Model the CaMoO_4 Unit Cell	19
2.3	Comparative Results between the Experimental Raman-Active Modes of CaMoO_4 Obtained in This Work and Those Reported in the Literature by Different Synthesis Methods ^a	23
2.4	Comparative Results between the Experimental Infrared Active Modes of CaMoO_4 Obtained in This Work and Those Reported in the Literature by Different Synthesis Methods ^a	25
2.5	Comparative Results between the Optical Band Gap Energy (Experimental and Theoretical) of CaMoO_4 Obtained in This Work and Those Reported in the Literature by Different Synthesis Methods ^a	40
3.1	Data Obtained by MR Spectra Analyses of MTO Thin Films Heat Treated at Different Temperatures in Comparison with Other Studies Reported in the Literature	72
4.1	Lattice parameters, unit cell volume, atomic coordinate obtained experimentally from the structural refinement by the Rietveld method and theoretically calculated from DFT method.	101

C.1	Positions of active Raman-modes (experimental and theoretical)	141
C.2	Positions of active IR-modes (experimental and theoretical) . . .	142

List of Figures

1.1	Esquema da excitação e decaimento em processos fotoluminescentes	5
1.2	Esquema do deslocamento do Átomo de Mo no cluster $[\text{MoO}_4]$.	7
2.1	(a) XRD patterns of CaMoO_4 meso- and nanocrystals prepared with different solvent ratios ($\text{H}_2\text{O}/\text{C}_2\text{H}_6\text{O}_2$) and processed in a microwave-assisted hydrothermal/solvothermal system at 140°C for 1 h and (b) a = b, and c lattice parameters as a function of different solvent ratios. The vertical bars show the standard mean error.	17
2.2	Schematic representation of the CaMoO_4 ($1 \times 1 \times 1$) unit cell illustrating the $[\text{MoO}_4]$ and $[\text{CaO}_8]$ clusters.	19
2.3	FT-Raman spectra in the range from 75 to 1000 cm^{-1} for the CaMoO_4 meso- and nanocrystals prepared with different solvent ratios ($\text{H}_2\text{O}/\text{C}_2\text{H}_6\text{O}_2$) and processed in a microwave-assisted hydrothermal/solvothermal system. The inset shows the $[\text{MoO}_4]$ clusters with symmetric stretching vibration.	21

2.4 FT-IR spectra in the range from 395 to 1000 cm^{-1} for the CaMoO_4 meso- and nanocrystals prepared with different solvent ratios ($\text{H}_2\text{O}/\text{C}_2\text{H}_6\text{O}_2$) and processed in a microwave-assisted hydrothermal/solvothermal system. The inset shows the $[\text{MoO}_4]$ clusters with antisymmetric stretching vibration. . . 24

- 2.5 (a) Low magnification FEG-SEM micrograph of several CaMoO_4 crystals. (b) High magnification FEG-SEM micrographs of selected area in part a (dotted white square). Inset shows the zoom in part b of CaMoO_4 nanocrystals and nano-octahedrons with well-defined faces prepared with 100 mL of H_2O as solvent. (c) Low magnification FEG-SEM micrograph of several CaMoO_4 crystals prepared with 75 mL of H_2O and 25 mL of $\text{C}_2\text{H}_6\text{O}_2$ as solvents. Pink and green rectangles in part c are illustrated individually by high magnification FEG-SEM micrographs in parts d and e. (f) Low magnification FEG-SEM micrograph of several spherical-like CaMoO_4 mesocrystals prepared with 50 mL of H_2O and 50 mL of $\text{C}_2\text{H}_6\text{O}_2$ as solvents. Blue squares and yellow rectangles in part f are illustrated individually by high magnification FEG-SEM micrographs in parts g and h. (i) Low magnification FEG-SEM micrograph of several quasispherical-like CaMoO_4 nanostructures prepared with 25 mL of H_2O and 75 mL of $\text{C}_2\text{H}_6\text{O}_2$ as solvents. (j) Medium magnification FEG-SEM micrographs of quasi-spherical-like CaMoO_4 nanostructures. Inset in part j (red square) illustrates individual quasi-spherical-like CaMoO_4 nanostructures. (k) Low magnification FEG-SEM micrograph of several CaMoO_4 nanocrystals prepared with 100 mL of $\text{C}_2\text{H}_6\text{O}_2$ as solvent. (l) High magnification FEG-SEM micrographs of CaMoO_4 nanocrystals. 26

- 2.6 (a) Low magnification TEM micrographs of CaMoO_4 crystals synthesized in aqueous solution. (b) HR-TEM micrograph performed on the edge of a crystal (dotted white square) (inset shows the corresponding SAED pattern). (c) TEM micrographs of CaMoO_4 crystals synthesized with different solvent volume ratios: 75 mL of H_2O /25 mL of $\text{C}_2\text{H}_6\text{O}_2$. (d) HR-TEM micrograph performed on the edge of a crystal (dotted white square) (inset shows the corresponding SAED pattern). (e) TEM micrographs of CaMoO_4 mesocrystals synthesized with different solvent volume ratios: (50 mL of H_2O /50 mL of $\text{C}_2\text{H}_6\text{O}_2$. (f) HR-TEM micrograph performed on the edge of a mesocrystal (dotted white square) (inset shows the corresponding SAED pattern). (g) TEM micrographs of CaMoO_4 crystals synthesized with different solvent volume ratios: 25 mL of H_2O /75 mL of $\text{C}_2\text{H}_6\text{O}_2$. (h) HR-TEM micrograph performed on the edge of a crystal (dotted white square) (inset shows the corresponding SAED pattern). (i) TEM micrographs of CaMoO_4 crystals synthesized with 100 mL of $\text{C}_2\text{H}_6\text{O}_2$. (j) HR-TEM micrograph performed on the two nanocrystals when aggregation oriented (dotted white square) (inset shows the corresponding SAED pattern). 30
- 2.7 Average size distribution of CaMoO_4 meso- and nanocrystals prepared with different solvent ratios ($\text{H}_2\text{O}/\text{C}_2\text{H}_6\text{O}_2$) and processed in a microwave-assisted hydrothermal/solvothermal system: (a) 100 mL of H_2O , (b) 75 mL of H_2O and 25 mL of $\text{C}_2\text{H}_6\text{O}_2$, (c) 50 mL of H_2O and 50 mL of $\text{C}_2\text{H}_6\text{O}_2$, (d) 25 mL of H_2O and 75 mL of $\text{C}_2\text{H}_6\text{O}_2$, and (e) 100 mL of $\text{C}_2\text{H}_6\text{O}_2$ 33

-
- 2.8 Schematic representation of the synthesis, processing, and growth mechanism of CaMoO_4 meso- and nanocrystals: (a) chemical synthesis (solvation and coprecipitation reaction), (b) increase of precipitation rate with NH_4OH and different types of hydrogen bonds between H_2O and/or $\text{C}_2\text{H}_6\text{O}_2$, (c) the different solvent ratios ($\text{H}_2\text{O}/\text{C}_2\text{H}_6\text{O}_2$) employed in preparation of CaMoO_4 meso-/nanocrystals and transference to a Teflon autoclave, (d) domestic microwave-assisted hydrothermal/solvothermal system employed in the processing of CaMoO_4 meso-/nanocrystals, (e) increase of the effective collision rates between the nano- and microcrystals with heating by action of the microwave irradiation and possible involvement of solvent molecules on the crystals, causing steric hindrance, orientation, and trapping of small nanocrystals, promoting anisotropic/isotropic growth, and (f) meso-/nanocrystal growth evolution as a function of processing in microwaves with different solvent ratios ($\text{H}_2\text{O}/\text{C}_2\text{H}_6\text{O}_2$). 35
- 2.9 UV–vis absorbance spectra of CaMoO_4 crystals prepared with different solvent ratios ($\text{H}_2\text{O}/\text{C}_2\text{H}_6\text{O}_2$) and processed in a microwave-assisted hydrothermal/solvothermal system: (a) 100 mL of H_2O , (b) 75 mL of H_2O and 25 mL of $\text{C}_2\text{H}_6\text{O}_2$, (c) 50 mL of H_2O and 50 mL of $\text{C}_2\text{H}_6\text{O}_2$, (d) 25 mL of H_2O and 75 mL of $\text{C}_2\text{H}_6\text{O}_2$, (e) 100 mL of $\text{C}_2\text{H}_6\text{O}_2$, and (f) optical band gap values as a function of different solvent ratios. 38
- 2.10 Calculated band structures of the crystalline CaMoO_4 phase without (a) and with (b) displacements on the Mo atoms. 41

2.11	Total DOS of crystalline structure CaMoO_4 without (a) and with (b) displacements on the Mo atoms.	43
2.12	(a) Schematic representation of the unit cell under microwave irradiation, (b) possible distortion sets on the $[\text{MoO}_4]$ clusters into the lattice caused by coupling with microwave irradiation, (c) wavelength employed in the excitation process of CaMoO_4 meso- and nanocrystals, (d) proposed wide band model before excitation with the presence of intermediary energy levels, (e) electronic transition from oxygen 2p orbitals (lower energy levels) to molybdenum 4d orbitals (higher energy levels) by absorption of $(h\nu)$ at room temperature, (f) emission process of photons $(h\nu')$ because of the radiative return processes of electrons situated at molybdenum 4d orbitals to oxygen 2p orbitals, and (g) PL spectra of CaMoO_4 meso- and nanocrystals prepared with different solvent ratios ($\text{H}_2\text{O}/\text{C}_2\text{H}_6\text{O}_2$). Inset shows the distorted MoO_4 clusters in the x, y, and z axes.	46
3.1	MTO-o model can be designated $[\text{TiO}_6]_o-[\text{TiO}_6]_o$ clusters because each titanium atom is surrounded by 6 O and $[\text{MgO}_6]_o-[\text{MgO}_6]_o$ cluster as 12 O surround the Mg atom. . . .	68
3.2	XRD patterns of MTO thin films on a Pt(111)/Ti/SiO ₂ /Si(100) substrate heat treated at (a) 400 °C; (b) 450 °C; (c) 500 °C; (d) 550 °C; (e) 600 °C; (f) 650 °C; and (g) 700 °C.	70

3.3	MR spectra of MTO thin films on a Pt(111)/Ti/SiO ₂ /Si(100) substrate heat treated at (a) 400 °C; (b) 450 °C; (c) 500 °C; (d) 550 °C; (e) 600 °C; (f) 650 °C; and (g) 700 °C. Insert: MR spectra of MTO thin films heat treated at (a) 400 °C; (b) 450 °C; (c) 500 °C; and (d) 550 °C.	71
3.4	FEG-SEM micrographs of the surface microstructure and cross section of MTO thin films on a Pt(111)/Ti/SiO ₂ /Si(100) substrate heat treated at (a) 400 °C; (b) 450 °C; (c) 500 °C; (d) 550 °C; (e) 600 °C; (f) 650 °C; and (g) 700 °C.	74
3.5	AFM micrographs of MTO thin films on a Pt(111)/Ti/SiO ₂ /Si(100) substrate heat treated at (a) 400 °C; (b) 550 °C; and (c) 700 °C.	75
3.6	UV–vis optical absorption edge for (a) 400 °C; (b) 450 °C; (c) 500 °C; (d) 550 °C; (e) 600 °C; (f) 650 °C; and (g) 700 °C. . . .	76
3.7	Calculated energy band structures for (a) MTO-o; (b) MTO-f; (c) MTO-m; and (d) MTO-fm.	78
3.8	Total and atom-projected DOS for (a) MTO-o; (b) MTO-f; (c) MTO-m; and (d) MTO-fm models.	81
3.9	Electron density maps of (a) MTO-o; (b) MTO-f; (c) MTO-m; and (d) MTO-fm.	83
3.10	PL spectra of MTO thin films on a Pt(111)/Ti/SiO ₂ /Si(100) substrate heat treated at (a) 400 °C; (b) 450 °C; (c) 500 °C; (d) 550 °C; (e) 600 °C; (f) 650 °C; and (g) 700 °C; excited with a 350.7 nm line of a krypton ion laser. (A) Two-dimensional graphic of PL spectra; (B) schematic representation of a MgTiO ₃ 1 × 1 × 1 unit cell rhombohedral structure; and (C) Three-dimensional graphic of PL spectra.	84

-
- 4.1 (a) XRD patterns, (b) Rietveld refinement plot of β -ZnMoO₄ microcrystals synthesized at 140°C for 8 h in HT system and (c) XRD patterns theoretically calculated, respectively. 100
- 4.2 Schematic representation of the monoclinic unit cells corresponding to β -ZnMoO₄ crystals projected at same axis: (a, c and e) experimental and (b, d and f) theoretical, respectively. . . 103
- 4.3 (a) FT-Raman spectrum of β -ZnMoO₄ microcrystals synthesized at 140 °C for 8 h in HT system and (b) comparative between the relative positions of theoretical and experimental Raman-active modes. 105
- 4.4 (a) FT-IR spectrum of β -ZnMoO₄ microcrystals synthesized at 140 °C for 8 h in HT system and (b) comparative between the relative positions of theoretical and experimental IR-active modes. 108
- 4.5 (a) UV-Vis spectra of β -ZnMoO₄ microcrystals synthesized at 140 °C for 8 h in HT system and (b) optimized band structure of β -ZnMoO₄ crystals. 112
- 4.6 (a) Projected partial DOS on the Mo orbitals and (b) projected total DOS on the Zn, Mo and O orbitals for the β -ZnMoO₄ crystals. 113
- 4.7 Electronic density map on the: (a) (2 0 0) plane, (b) (1 0 0) plane, (c) (4 0 0) plane, and (d) (0 0 4) plane of the β -ZnMoO₄ crystals (e) Possible mechanism of charge transference between the clusters and (f) PL spectra of β -ZnMoO₄ microcrystals synthesized at 140 °C for 8 h in HT system. Insets show the digital photographs of its corresponding PL emissions and FE-SEM image of individual microcrystal, respectively. 116

RESUMO

Fotoluminescência do CaMoO_4 , MgTiO_3 e $\beta\text{-ZnMoO}_4$: um estudo teórico

Neste trabalho, cristais de molibdato de cálcio (CaMoO_4), filmes finos de MgTiO_3 (MTO) e microcristais de beta molibdato de zinco ($\beta\text{-ZnMoO}_4$) foram sintetizados por diferentes métodos e estruturalmente caracterizados por Difração de Raios-X (DRX), refinamento Rietveld, espectroscopia por transformada de Fourier Raman (FT-Raman) e espectroscopia por transformada de Fourier de infravermelho (FT-IR).

Empregou-se o estudo teórico e experimental combinados na compreensão das propriedades de estrutura eletrônica e da fotoluminescência (FL) desses materiais.

Suas propriedades ópticas foram investigadas por (UV-vis) espectroscopia de absorção ultravioleta-visível e medidas de PL. Foram realizados cálculos de primeiros princípios da mecânica quântica com base na teoria do funcional da densidade (DFT) com o funcional B3LYP.

As emissões FL nas regiões do azul e verde observadas nos cristais de CaMoO_4 foram atribuídas aos níveis de energia intermediários decorrentes das distorções no cluster de $[\text{MoO}_4]$ devido a defeitos intrínsecos na estrutura de anisotrópicos/cristais isotrópicos. Estrutura de banda e densidade de estados descreveram os níveis energia e um gap direto ($\Gamma - \Gamma$). Em princípio, os dados teóricos sugeriram uma forte hibridização entre os orbitais 2p dos átomos O (acima da banda de valência) e dos orbitais 4d dos átomos de Mo (perto da banda de condução), respectivamente.

Resultados da estrutura de bandas indicam um gap indireto para os modelos ordenados e desordenado para o MgTiO_3 em diferentes regiões da zona Brillouin e a densidade de estados (DOS) mostram novos níveis de energia com o

átomo de Ti deslocado. Os mapas de carga foram utilizados nesta estrutura para verificar densidades de cargas distribuídas de forma assimétrica, contribuindo para a formação de densidades de elétrons e buracos na estrutura.

Com relação ao β -ZnMoO₄, os resultados calculados teoricamente das frequências Raman e IR estão de acordo com os resultados experimentais. Medições de absorção UV-vis mostram um valor gap de 3,17 eV, enquanto a estrutura de banda calculada tem um valor de 3,22 eV. A densidade de estados indica que os principais orbitais envolvidos na estrutura eletrônica dos cristais de β -ZnMoO₄ são orbitais 2p do oxigênio na banda de valência e orbitais 4d do Mo na banda de condução.

ABSTRACT

Photoluminescence of the CaMoO_4 , MgTiO_3 and $\beta\text{-ZnMoO}_4$: an theoretical study

In this work, calcium molybdate (CaMoO_4) crystals, MgTiO_3 (MTO) thin films and beta zinc molybdate ($\beta\text{-ZnMoO}_4$) microcrystals were synthesized by the different methods and structurally characterized X-ray diffraction (XRD), Rietveld refinement, Fourier transform Raman (FT-Raman) and Fourier transform infrared (FT-IR) spectroscopies.

A combined theoretical and experimental study on the electronic structure and photoluminescence (PL) properties these materials has been employed.

Their optical properties were investigated by ultraviolet-visible (UV-vis) absorption spectroscopy and PL measurements. First-principles quantum mechanical calculations based on the density functional theory at the B3LYP calculation level have been carried out.

The blue and green PL emissions observed in these crystals of the CaMoO_4 were ascribed to the intermediary energy levels arising from the distortions on the $[\text{MoO}_4]$ clusters due to intrinsic defects in the lattice of anisotropic/isotropic crystals. Band structure and Density of states described the levels energy and a direct gap ($\Gamma - \Gamma$). In principle, the theoretical data suggested a strong hybridization between the O 2p (above the VB) and Mo 4d orbitals (near the CB), respectively.

Band structure results indicate an indirect band gap for ordered and disordered models of the MgTiO_3 in different regions of the Brillouin zone and density of states (DOS) show creates new levels energy with the dislocated Ti atom. The charge maps were used in this structure to verify densities charge

distributed asymmetrically, contributing to the formation densities of electrons and holes in the structure.

With relation the β -ZnMoO₄, the theoretically calculated results of IR and Raman frequencies are in agreement with experimental results. UV-vis absorption measurements shows an optical band gap value of 3.17 eV, while the calculated band structure has a value of 3.22 eV. The density of states indicate that the main orbitals involved in the electronic structure of β -ZnMoO₄ crystals are oxygen 2p in the valence band and Mo 4d in the conduction band.

Contents

1	Introduction	2
1.1	Objetivo	2
1.2	Nanociência	3
1.3	Propriedades Óticas e Fotoluminescência	4
1.4	Calculos Teóricos	5
2	Paper 1 - Effect of Different Solvent Ratios (Water/Ethylene Glycol) on the Growth Process of CaMoO₄ Crystals and Their Optical Properties	8
2.1	Introduction	10
2.2	Experimental procedure	13
2.2.1	Synthesis and Microwave Processing of CaMoO ₄ Crystals	13
2.2.2	Characterization of CaMoO ₄ Crystals	14
2.2.3	Density Functional Theory for the Electronic Structure of CaMoO ₄	15
2.3	Results and Discussion	16
2.3.1	X-ray Diffraction Analyses	16
2.3.2	Representation of the CaMoO ₄ Unit Cell	18

2.3.3	Fourier Transform Raman/Infrared Spectroscopy Analyses	20
2.3.4	FEG-SEM Analyses of CaMoO₄ Crystals	25
2.3.5	TEM Analyses of CaMoO₄ Crystals	29
2.3.6	Average Size Distribution of CaMoO₄ Crystals	33
2.3.7	Growth Mechanism of CaMoO₄ Crystals	34
2.3.8	UV–Visible Absorption Spectroscopy Analyses of CaMoO₄ Crystals	38
2.3.9	Band Structures of the Crystalline CaMoO₄ Phase without and with Displacements Theoretically Induced on the Mo Atoms	41
2.3.10	Density of States for the Crystalline CaMoO₄ Structure without and with Displacements Theoretically Induced on the Mo Atoms.	42
2.3.11	Photoluminescence Properties Analyses: Distortions on the [MoO₄] Clusters in the Lattice by Microwave Irradiation and a Wide Band Model	44
2.4	Conclusions	48
2.5	References	52
3	Paper 2 - Very Intense Distinct Blue and Red Photoluminescence Emission in MgTiO₃ Thin Films Prepared by the Polymeric Precursor Method: An Experimental and Theoretical Approach	60
3.1	Introduction	62

3.2	Experimental Procedures	65
3.2.1	Synthesis of MTO Thin Films	65
3.2.2	Characterization Techniques	66
3.3	Computational Details, Models, and Mechanisms . . .	67
3.3.1	Packages, Functions, and Basis Sets	67
3.3.2	MTO Structure and Periodic Model Details . .	67
3.4	Results and Discussion	70
3.4.1	X-ray Diffraction Patterns	70
3.4.2	Micro-Raman Analysis	71
3.4.3	Field-Emission Gun Scanning Electron Mi- croscopy Analyses	72
3.4.4	Atomic Force Microscopy Analysis	74
3.4.5	Ultraviolet–Visible Absorption Spectroscopy Analysis	75
3.4.6	Energy Band Structure	77
3.4.7	Density of States	80
3.4.8	Electron Density Map	82
3.4.9	PL Emission at Room Temperature in MTO Thin Films	83
3.5	Conclusions	87
3.6	References	89
4	Paper 3 - A combined theoretical and experimental study of electronic structure and optical properties of β- ZnMoO₄ microcrystals	93
4.1	Introduction	94

4.2	Experimental details	96
4.2.1	Synthesis of β -ZnMoO ₄ microcrystals	96
4.2.2	Characterizations β -ZnMoO ₄ microcrystals	97
4.2.3	Computational Method and Periodic Model of β -ZnMoO ₄ microcrystals	98
4.3	Results and discussion	99
4.3.1	X-ray diffraction and Rietveld refinement analyses of β -ZnMoO ₄ crystals	99
4.3.2	Unit cell representations of β -ZnMoO ₄ crystals	102
4.3.3	Fourier-transform Raman/infrared Spectroscopies: Theoretical and experimental analyses of β -ZnMoO ₄ crystals	104
4.3.4	Ultraviolet-visible absorption spectroscopy and band structures of β -ZnMoO ₄ crystals	110
4.3.5	Density of states of β -ZnMoO ₄ crystals	113
4.3.6	Electron density maps and PL emission of β -ZnMoO ₄ crystals	114
4.4	Conclusions	119
4.5	References	120
5	Conclusions	127
6	Future perspective	129
A	Flowchart of the theoretical calculation of structures	132
B	Figures for the Supporting Information: Effect of differ-	

ent solvent ratios (water/ethylene glycol) on the growth process of CaMoO_4 crystals and its optical properties 133

C Support Information: A combined theoretical and experimental study of electronic structure and optical properties of $\beta\text{-ZnMoO}_4$ microcrystals 141

Chapter 1

Introduction

1.1 Objetivo

Neste trabalho aplicou-se cálculos teóricos, juntamente com a síntese e caracterização experimental, no estudo das características estruturais e eletrônicas de alguns materiais, entre os quais molibdato de cálcio (CaMoO_4), titanato de magnésio (MgTiO_3) e beta molibdato de zinco ($\beta\text{-ZnMoO}_4$), buscando a compreensão da fotoluminescência destes materiais. O trabalho está organizado em três artigos, na qual foi desenvolvido com outros colaboradores com o intuito de buscar a compreensão das propriedades óticas, com ênfase na fotoluminescência, em materiais sintetizados em várias metodologias distintas, no entanto, com a mesma teoria pode-se compreender melhor os mecanismos responsáveis pelas propriedades óticas. Através do modelo de ordem-desordem, pode-se relacionar as características estruturais com a organização eletrônica e estabelecer uma ligação entre estes e as propriedades óticas.

1.2 Nanociência

Recentemente, a nanociência tem sido muito importante em vários campos científicos para a descoberta de novas moléculas ou estruturas na escala nanométrica (1 a 100 nm). Por exemplo, buckytubes, silicon nanorods, e compound semiconductors quantum dots. Mas qual a relação entre o tamanho e formato da estrutura e as propriedades? É certo que muitas propriedades interessantes tem surgido desde compostos de escala nanométrica.[1]

Estas nanoestruturas tem sido aplicadas de diversas formas, nas quais, na farmácia em drogas terapêuticas, marcação de chips de DNA, armazenamento de informação, refrigeração, computadores ópticos/químicos, melhoramento de cerâmica e isoladores, metais mais duros, precursores de filmes, células solares, purificação de água, catálise, sensores, eletrodos e polímeros nanoestruturados melhorados.[2]

Nanociência surtiu com o advento de inúmeras técnicas de caracterização que têm sido aplicados para melhor estudar as nanoestruturas, como por exemplo, Microscopia Eletrônica de Transmissão de alta resolução (HRTEM), Microscopia de Tunelamento (STM) e Microscopia de Força Atômica (AFM), Difração de Raios X (XRD), Calorimetria de Varriemento Diferencial (DSC) entre outras técnicas.[2]

Os materiais a serem descobertos irá produzir um novo conjunto de propriedades, dependendo do tamanho, entre outros podem ser mencionados, propriedades ópticas, propriedades magnéticas e morfologias de cristal.[2]

Muitos materiais tem sido sintetizados por várias técnicas, possibilitando o descobrimento de uma ampla variedade de nano (e micro) materiais com propriedades e morfologias interessantes. Por exemplo, Perovskitas de

SrTiO₃ (STO)[3], Scheelitas de CaWO₄[4], e α -Ag₂WO₄[5] e β -Ag₂WO₄ com filamentos de prata.[6].

1.3 Propriedades Óticas e Fotoluminescência

Para uma melhor compreensão das propriedades do material, a Difracção de Raios-X é utilizado para informar as características estruturais a longa distância do material e a Espectroscopia de IR-Raman pode caracterizar a estrutura do cluster dentro da célula unitária, ou seja, a uma distância curta. Mas a Espectroscopia de Fotoluminescência é uma ferramenta muito importante na observação das características estruturais a média distância.[7]

A fotoluminescência é considerada uma ferramenta poderosa para a obtenção de informações sobre a estrutura eletrônica e organização estrutural de médio alcance de materiais. Em geral, acredita-se que as propriedades fotoluminescentes podem ser atribuído ao grau ordem-desordem, tal como a distorção na estrutura cristalina, ou eles podem ser explicados pelos estados eletrônicos dentro do intervalo de banda devido a vacâncias, defeitos e impurezas. Assim, a emissão fotoluminescente é considerado um processo típica de vários níveis e multifóton, isto é, um sistema em que o relaxamento ocorre ao longo de vários caminhos, que envolve vários estados intermédios para a diminuição do *bandgap* (zona proibida entra a banda de valência e a de condução)[8], desse modo, aumentando a possibilidade de transições entre estas banda e assim emitindo fótons (fotoluminescência) como ilustra o esquema da Figura 1.1.

De acordo com o modelo elétron/buraco, o material tem um defeito específico com a habilidade de gerar pares e^-h^\bullet (elétron-buraco). O efeito da fotoluminescência ao longo do cluster é criada pela distribuição de de-

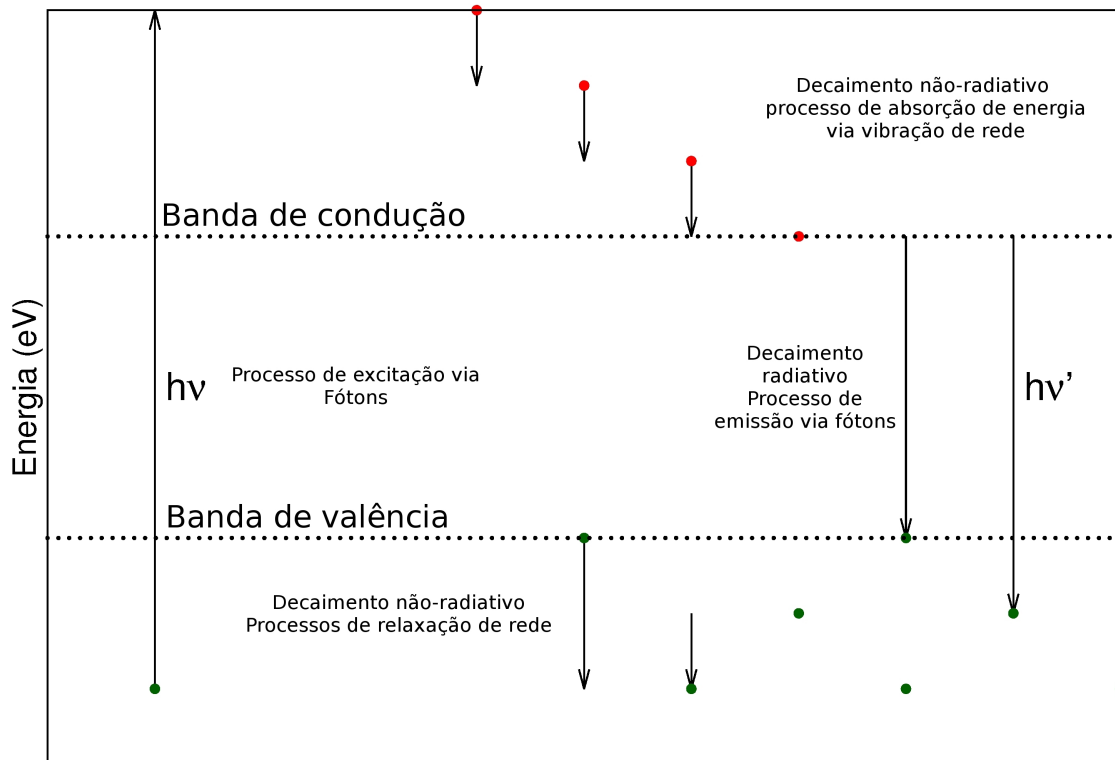


Figure 1.1: Esquema da excitação e decaimento em processos fotoluminescentes

feitos extrínsecos (superfície) e intrínsecos (bulk). Esses defeitos criam regiões de diferente distribuição de densidade eletrônica ao longo do cluster (CCCT - cluster-to-cluster charge transfer) possibilitando a formação dos níveis intermediários.[9]

1.4 Cálculos Teóricos

As Scheelitas CaMoO_4 , Perovskitas MgTiO_3 e Wolframita $\beta\text{-ZnMoO}_4$ são conhecidas por suas propriedades óticas e fotocatalíticas, no qual suas propriedades estão relacionado ao mecanismo de geração de pares e^-h^\bullet (elétron/buraco).

Para este estudo, utilizou-se calculos teóricos usando cálculos de Primeiros princípios da mecânica quântica baseados na Teoria Funcional de

Densidade (DFT).

O DFT (na formulação Kohn-Sham) tem sido considerado uma ferramenta eficiente para Química Teórica aplicada, incluindo as vantagens de métodos semi-empíricos, do uso de funções de onda monodeterminantal bem como corresponde com simplicidade a interpretação de propriedades que estão relacionadas com um conjunto simples de base (spin) orbitais.[10]

Os modelos criados neste trabalho foram definidos inicialmente a partir de dados de Difração de Raios-X(XRD) e do refinamento de Rietveld, e com esses dados, fez-se os calculos usando-se o pacote de programas CRYSTAL[11] (veja o Anexo A).

Para a simulação dos defeitos, fez-se um deslocamento no átomo formador de rede ou no modificador de rede. Esse deslocamento sempre foi em relação ao um oxigênio ligado ao átomo central de modo a aproxima-lo(ou afasta-lo) para que forme-se novos níveis intermediários e crie regiões de densidade eletrônicas diferentes para formação de pares de elétron/buraco.

A Figura 1.2 ilustra uma cela unitária de uma estrutura tetragonal (Scheelita) com um deslocamento do átomo formador de rede em relação ao oxigênio em 0.3\AA (as coordenadas i,j e k refere-se aos vetores decomposição do vetor principal de deslocamento de 0.3\AA de comprimento).

Para a descrição dos defeitos utilizou-se a notação de Kröger–Vink, no qual os elementos com carga efetiva positiva são representados por \bullet e os elementos com carga efetiva negativa por $'$. Os elementos neutros por um x [12].

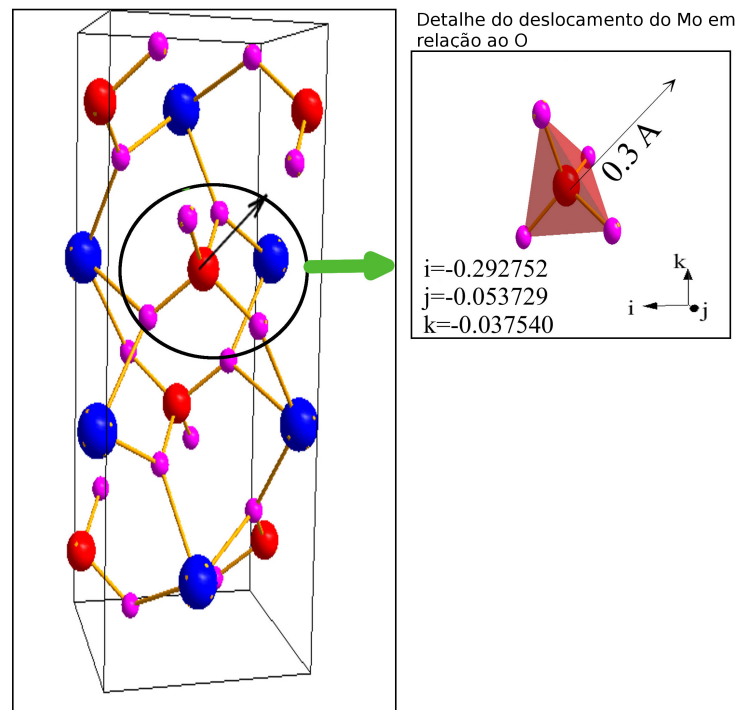


Figure 1.2: Esquema do deslocamento do Átomo de Mo no cluster $[\text{MoO}_4]$

Chapter 2

Paper 1 - Effect of Different Solvent Ratios (Water/Ethylene Glycol) on the Growth Process of CaMoO_4 Crystals and Their Optical Properties

V. S. Marques [†], L. S. Cavalcante [‡], J. C. Sczancoski [§], A. F. P. Alcântara [†], M. O. Orlandi [‡], E. Moraes [§], E. Longo [‡], J. A. Varela [‡], M. Siu Li ^{||}, and M. R. M. C. Santos [†]

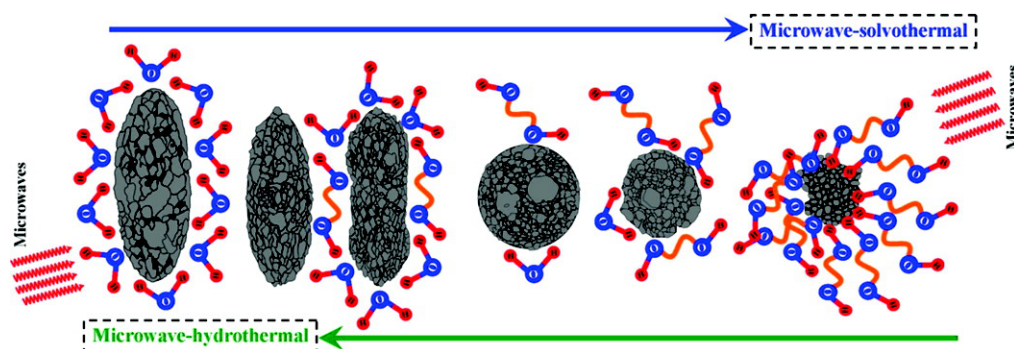
Cryst. Growth Des., **2010**, *10* (11), pp 4752–4768

[†] LIMAV-CCN-Química, UFPI—Universidade Federal do Piauí, 64049-550 Teresina, PI, Brazil

[‡] UNESP—Universidade Estadual Paulista, P.O. Box 355, 14801-907 Araraquara, SP, Brazil

[§] LIEC—Universidade Federal de São Carlos, P.O. Box 676, 13565-905 São Carlos, SP, Brazil

^{||} IFSC, Universidade de São Paulo, P.O. Box 369, 13560-970 São Carlos, SP, Brazil



Abstract

In this paper, calcium molybdate (CaMoO_4) crystals (meso- and nanoscale) were synthesized by the coprecipitation method using different solvent volume ratios (water/ethylene glycol). Subsequently, the obtained suspensions were processed in microwave-assisted hydrothermal/solvothermal systems at 140°C for 1 h. These meso- and nanocrystals processed were characterized by X-ray diffraction (XRD), Fourier transform Raman (FT-Raman), Fourier transform infrared (FT-IR), ultraviolet–visible (UV-vis) absorption spectroscopies, field-emission gun scanning electron microscopy (FEG-SEM), transmission electron microscopy (TEM), and photoluminescence (PL) measurements. XRD patterns and FT-Raman spectra showed that these meso- and nanocrystals have a scheelite-type tetragonal structure without the presence of deleterious phases. FT-IR spectra exhibited a large absorption band situated at around 827 cm^{-1} , which is associated with the Mo–O antisymmetric stretching vibrations into the $[\text{MoO}_4]$ clusters. FEG-SEM micrographs indicated that the ethylene glycol concentration in the aqueous solution plays an important role in the morphological evolution of CaMoO_4 crystals. High-resolution TEM micrographs demonstrated that the mesocrystals consist of several aggregated nanoparticles with electron diffraction patterns of monocrystal. In addition, the differences observed in the selected area electron diffraction patterns of CaMoO_4 crystals proved the coexistence of both nano- and mesostructures. First-principles quantum mechanical calculations based on the density functional theory at the B3LYP level were employed in order to understand the band structure and density of states for the CaMoO_4 . UV-vis absorption measurements evidenced a variation in optical band gap values (from 3.42 to 3.72 eV) for the distinct morphologies. The blue and green PL emissions observed in these crystals were ascribed to the intermediary energy

levels arising from the distortions on the $[\text{MoO}_4]$ clusters due to intrinsic defects in the lattice of anisotropic/isotropic crystals.

2.1 Introduction

Calcium molybdate (CaMoO_4) is an important material belonging to the scheelite family with tetragonal structure and space group $I4_1/a$. [1, 2a, 2b] In this structure, the Mo atoms are bonded to four oxygens, forming the $[\text{MoO}_4]$ clusters, while the Ca atoms are coordinated to eight oxygens, forming the $[\text{CaO}_8]$ clusters. [3-7] In recent years, this molybdate has attracted the attention of diverse scientific and technological fields because of its wide potential for applications in acousto-optic filters, [8] solid state lasers, [9, 10] white light-emitting diodes, [11] scintillators, [12] microwave dielectrics, [13, 14] fluorescent lamps, [15] negative electrodes for Li^+ -ion batteries, [16] and cryogenic scintillation detectors for search of ^{100}Mo double β decay, [17, 18] catalytic properties of propane ammoxidation, [19] and so on.

In terms of optical properties, this material exhibits green and/or blue luminescence emissions at room temperature when excited with wavelengths in the range from 240 to 537 nm. [19-22] However, few works in the literature have reported on the origin of the photoluminescence (PL) properties of CaMoO_4 . For example, Mikhailik et al. [23] explained that the short wavelength luminescence of this molybdate is usually caused by the intrinsic emission of the MoO_4^{2-} molecular complexes while its long wavelength luminescence arises from the MoO_3 oxygen-deficient defect centers. In another work, Mikhailik et al. [24] investigated the electronic transitions and lumines-

cence decay kinetics of CaMoO_4 at low temperatures (from -265 to 27°C) by means of ultraviolet excitation. According to these authors, the optical transitions occur in the MoO_4^{2-} molecular complexes, mainly involving the ($^1\text{A}_1$) ground, singlet ($^1\text{T}_1$, $^1\text{T}_2$), and triplet ($^3\text{T}_1$, $^3\text{T}_2$) levels. In this case, the electric dipole allowed $^1\text{A}_1 \rightarrow ^1\text{T}_2$ transitions contribute to the excitation process while the radiative transitions arise from the closely located lower-lying triplet states. Ryu et al.[25] mentioned that, besides the charge-transfer transitions within the MoO_4^{2-} complexes, the PL response can be influenced by morphology and particle size distribution. Marques et al.[26] attributed the origin of this optical property to the degree of structural order—disorder in the lattice. Recently, Longo et al.,[27] through the first-principles quantum mechanical calculations based on the density functional theory, reported that the green and blue PL emissions of disordered CaMoO_4 powders are linked to the intrinsic slight distortion of the $[\text{MoO}_4]$ tetrahedral clusters.

Considering the different chemical routes, the conventional hydrothermal systems are well-known due to their versatility in the formation and crystallization of ceramic oxides at low temperatures, enabling a good control of morphologies and particle sizes.[28] On the other hand, the long processing times exhibited by this synthesis method were overcome using microwave radiation as energy source for this system. This innovation resulted in the development of equipment currently known as microwave-hydrothermal.[28] In order to obtain a good efficiency of the microwave radiation with the liquid phase, it is necessary to use substances or solvents with high dielectric loss ($\tan \delta$).[29] In addition, according to Thongtem et al.,[29] compounds with large permanent dipole moments have large dielectric constants or relative permittivities. During the interaction with the microwave radiation, these dielectric properties can be considered key factors to get a faster heating to high temperatures at short times.

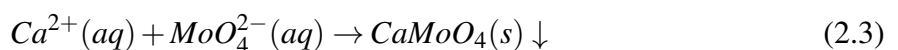
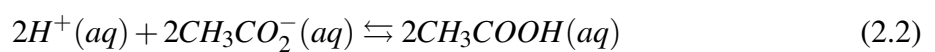
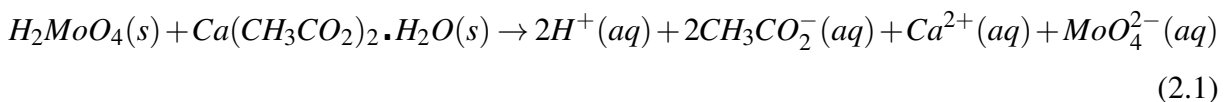
Hence, solutions in water (dielectric constant at 25°C = 78.4)[30] and ethylene glycol (dielectric constant at 25°C = 40.3)[29] are good candidates in order to be employed in microwave-assisted equipment operating at the frequency 2.45 GHz. The combination of microwave irradiation with the hydrothermal process was named the “microwave-hydrothermal” (MH) process. Similarly, the combination of microwave irradiation with solvothermal (not using water as a solvent) processes can be termed “microwave-solvothermal” (MS) processes, respectively. In relation to the utilization of different solvent ratios (water/ethylene glycol) for the preparation of CaMoO₄ oriented aggregate crystals and meso- and nanocrystals processed in a microwave, there are no works so far reported in the literature.

Therefore, in this paper, we report on the synthesis of CaMoO₄ oriented aggregate crystals and meso- and nanocrystals by the coprecipitation method with different solvent ratios (H₂O/C₂H₆O₂) and processed in a microwave-assisted hydrothermal/solvothermal system at 140°C for 1 h. These meso- and nanocrystals were analyzed by X-ray diffraction (XRD), Fourier transform Raman (FT-Raman), Fourier transform infrared (FT-IR), ultraviolet–visible (UV–vis) absorption spectroscopies, field-emission gun scanning electron microscopy (FEG-SEM), transmission electron microscopy (TEM), and photoluminescence (PL) measurements. Also, the experimental data were correlated with those obtained by the first-principles quantum mechanical calculations. The electronic structure (band structure and density of states) was theoretically calculated. The main aim is to understand the effect of different solvent ratios (H₂O/C₂H₆O₂) in volume on the growth process of CaMoO₄ crystals and its influence on the optical properties.

2.2 Experimental procedure

2.2.1 Synthesis and Microwave Processing of CaMoO₄ Crystals

The CaMoO₄ meso- and nanocrystals were synthesized by the coprecipitation method with different ratios of deionized water [H₂O] and ethylene glycol [C₂H₆O₂] (99.5% purity, J.T. Baker) and processed in a microwave-assisted hydrothermal/solvothermal system. The typical experimental procedure is described as follows: 0.0025 mol of molybdic acid [H₂MoO₄] (85% purity, Aldrich) and 0.0025 mol of calcium acetate monohydrate [Ca(CH₃CO₂)₂·H₂O] (99.5% purity, Aldrich) were added and dissolved in mixtures containing different solvent ratios (100 mL of H₂O; 75 mL of H₂O/25 mL of C₂H₆O₂; 50 mL of H₂O/50 mL of C₂H₆O₂; 25 mL of H₂O/75 mL of C₂H₆O₂ and 100 mL of C₂H₆O₂) in volume total. In the precipitation reaction, Ca²⁺ cations are the electron pair acceptor (Lewis acid), while the MoO₄²⁻ anions are the electron pair donor (Lewis base). The chemical reaction between these two species in solutions with different quantities of solvents (H₂O and C₂H₆O₂) results in formation of CaMoO₄, as shown below:



In order to increase the ionization rate, the solution pH was adjusted up to 10 by the addition of 5 mL of ammonium hydroxide [NH₄OH] (30% in NH₃, Mallinckrodt). In the sequence, these aqueous solutions with ethylene glycol, which has high affinity and solubility, due to formation of hydrogen bridges with water, were stirred for 30 min at room temperature. After the coprecipitation reaction, the solution was transferred into a Teflon autoclave, which was sealed and placed inside the microwave system (2.45 GHz, maximum power of 800 W). More details on this equipment have been reported in ref [31]. All these systems were processed at 140°C for 1 h. The heating rate in this system was fixed at 25°C/min, and the pressure in the autoclave was stabilized at 294 kPa. After processing, the autoclave was naturally cooled to room temperature. The resulting suspension was washed with deionized water several times to neutralize the solution pH (≈ 7). Finally, the white precipitates were collected and dried in a conventional furnace at 65°C for some hours.

2.2.2 Characterization of CaMoO₄ Crystals

The CaMoO₄ crystals were structurally characterized by X-ray powder diffraction (XRD) using a Rigaku-DMax/2500PC (Japan) with Cu K α radiation ($\lambda = 1.5406 \text{ \AA}$) in the 2θ range from 5° to 75° with a scanning rate of 0.2°/s. FT-Raman spectroscopy was recorded with a Bruker-RFS 100 (Germany). The spectra were obtained using a 1064 nm line of a Nd:YAG laser, keeping its maximum output power at 110 mW. FT-IR spectroscopies were performed in the range from 395 to 1000 cm⁻¹, using a Bruker-Equinox 55 (Germany) spectrometer in transmittance mode. The viscosity of solvents

were estimated at room temperature using a rheometer (Brookfield DV-III Ultra, USA). Nitrogen adsorption/desorption isotherms and specific surface area were recorded with an ASAP 2000 Phys/Chemisorption unit (Micromeritics, USA). In addition, the BET method (Brunauer, Emmett, and Teller)[32] was employed to estimate the specific surface area. The morphologies were investigated through a FEG-SEM of Carl Zeiss, model Supra 35-VP (Germany), operated at 6 kV and with a transmission electron microscope (TEM), model CM200 (Philips, USA), operated at 200 kV. In the preparation of TEM samples, the obtained powders were first dispersed in acetone using an ultrasonic bath for 20 min. Afterward, the suspensions were deposited on the copper grids via fast immersion. The crystallographic organizations as well as growth directions of CaMoO_4 crystals were investigated by means of high resolution transmission electron microscopy (HR-TEM) and selected-area electron diffraction (SAED). UV–vis spectra were taken using a spectrophotometer of Varian, model Cary 5G (USA), in diffuse reflection mode. PL measurements were performed with a Monospec 27 monochromator of Thermal Jarrel Ash (USA) coupled to a R446 photomultiplier of Hamamatsu Photonics (Japan). A krypton ion laser of Coherent Innova 90K (USA) ($\lambda = 350$ nm) was used as an excitation source, keeping its maximum output power at 200 mW. All measurements were performed at room temperature.

2.2.3 Density Functional Theory for the Electronic Structure of CaMoO_4

The periodic density functional theory (DFT) calculations were performed with the Becke's three-parameter hybrid nonlocal exchange func-

tional, combined with the Lee-Yang-Par gradient-corrected correlation function B3LYP, which has proven to be a very effective tool to deal with the present challenging problem. According to the literature,[35] the B3LYP functional is able to simulate the energetic, geometric, and electronic properties of materials with acceptable accuracy. In particular, considering the scheelite-type tetragonal structure, this functional has been successfully employed in investigations on the electronic structure.[27] In this work, the atomic centers were described by the following electronic basis sets: 86-511d3G for calcium, 311(d31)G for molybdenum, and 8-411d11G for oxygen atoms.[36] The electronic structures were calculated with the CRYSTAL06 software[37] using the numerical second derivatives of the total energies. The band structures were obtained for 200 K points along the high-symmetry paths on the adequate Brillouin zone. The density of states (DOS) was calculated through the electronic structure analyses. The band structures and DOS diagrams were modeled by the XCRYSDEN program.[38]

2.3 Results and Discussion

2.3.1 X-ray Diffraction Analyses

Figure 2.1 illustrates the XRD patterns and lattice parameter values of CaMoO_4 crystals prepared with different solvent volume ratios ($\text{H}_2\text{O}/\text{C}_2\text{H}_6\text{O}_2$) and processed in a microwave-assisted hydrothermal/solvothermal system at 140°C for 1 h, respectively.

All XRD patterns can be indexed to the tetragonal structure with space group $I4_1/a$, in agreement with the respective Joint Committee on Pow-

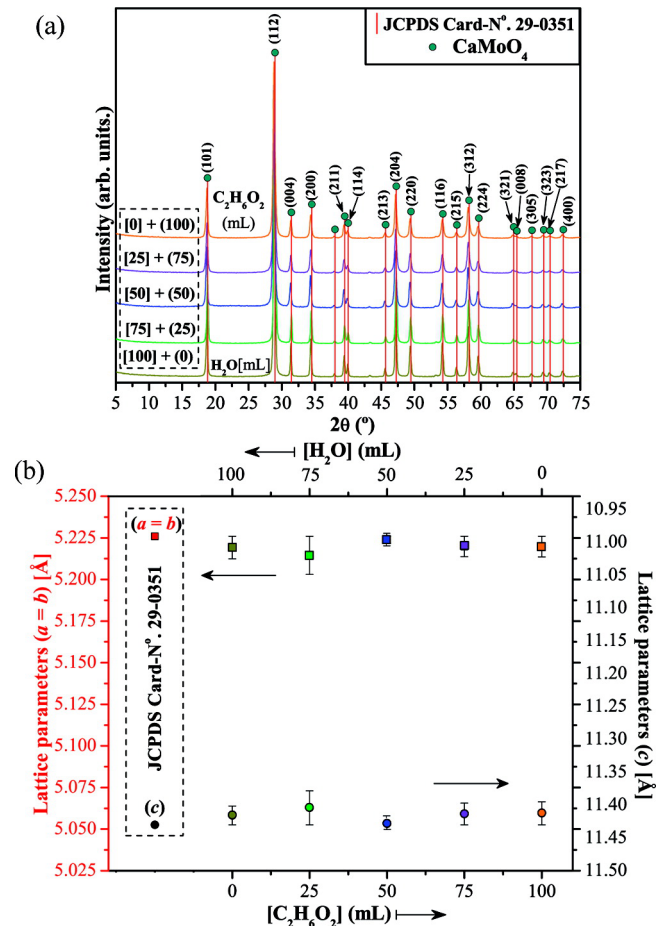


Figure 2.1: (a) XRD patterns of CaMoO₄ meso- and nanocrystals prepared with different solvent ratios (H₂O/C₂H₆O₂) and processed in a microwave-assisted hydrothermal/solvothermal system at 140°C for 1 h and (b) a = b, and c lattice parameters as a function of different solvent ratios. The vertical bars show the standard mean error.

der Diffraction Standards (JCPDS) No. 29-0351.[39] Diffraction peaks related to the secondary phases were not detected, indicating the formation of a pure single phase. Also, it is possible to note that these peaks are intense and well-defined, suggesting a good degree of crystallization or structural ordering at long-range. The experimental lattice parameters and unit cell volume were calculated using the least-squares refinement from the UnitCell-97 program.[40] The obtained values are shown in Figure 1b and displayed in Table 2.1.

Table 2.1: Comparative Results between the Lattice Parameters and Unit Cell Volume of CaMoO_4 Obtained in This Work with Those Reported in the Literature by Different Synthesis Methods^a

method	T(°C)	time(h)	lattice a	parameter b	c(Å)	unit cell volume (Å ³)	ref
MEHT	160	16	5.19	5.19	11.25	303.031	[41]
CZ	1200	24	5.1987	5.1987	11.4584	309.6802	[42]
CP	600	2	5.2231	5.2231	11.3973	310.9271	[43]
SSR	800	2	5.226	5.226	11.43	312.165	[44]
MH	140	1	5.219(2)	5.219(2)	11.415(8)	310.966(9)	[□]
MH	140	1	5.214(5)	5.214(5)	11.404(1)	310.088(9)	[□]
MSH	140	1	5.223(8)	5.223(8)	11.428(4)	311.859(1)	[□]
MS	140	1	5.219(8)	5.219(8)	11.413(5)	310.975(7)	[□]
MS	140	1	5.219(7)	5.219(7)	11.412(5)	310.936(6)	[□]
JCPDS			5.226	5.226	11.43	312.165(5)	[39]

^aT = temperature, ref = references, MEHT = microemulsion-hydrothermal, CZ = Czochralski, CP = complex polymerization; SSR = solid state reaction; MH = microwave-hydrothermal, MHS = microwave-hydrothermal-solvothermal, MS = microwave-solvothermal, and [□] = this work.

As can be seen in Figure 1b and Table 2.1, the lattice parameters and unit cell volume obtained in this work are very close to those reported in the literature[41-44] and with the respective JCPDS card No. 29-0351.[39] However, the slight variations or differences in these values can be directly related to the types of synthesis methods and experimental conditions (temperature, time, heating rate, atmosphere) as well as a consequence of the volumetric proportions ($\text{H}_2\text{O}/\text{C}_2\text{H}_6\text{O}_2$) in the nucleation or growth stages of the particles. Also, we demonstrate in previous papers that the lattice parameters are susceptible to modifications when there are residual stresses and/or distortions in the lattice.[45, 46]

2.3.2 Representation of the CaMoO_4 Unit Cell

Figure 2.2 shows the schematic representation of the tetragonal CaMoO_4 unit cell with space group $I4_1/a$.

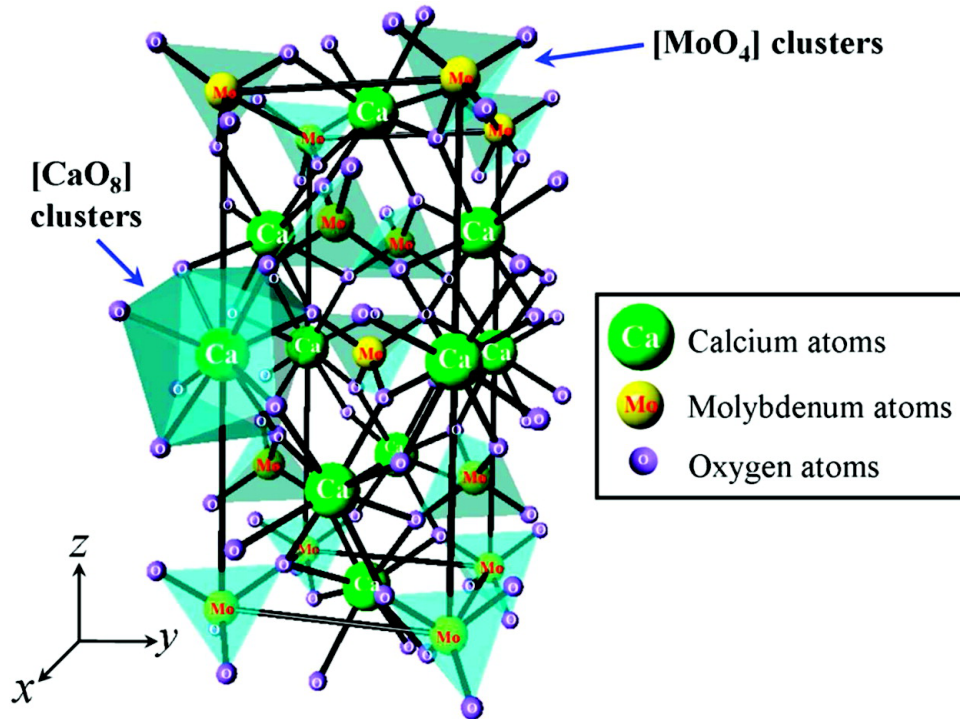


Figure 2.2: Schematic representation of the CaMoO_4 ($1 \times 1 \times 1$) unit cell illustrating the $[\text{MoO}_4]$ and $[\text{CaO}_8]$ clusters.

Table 2.2: Atomic Coordinates Employed To Model the CaMoO_4 Unit Cell

atom	site	x	y	z
calcium	4b	0	0	0.5
molybdenum	4a	0	0	0
oxygen	16f	0.233	0.14	0.082

This ideal unit cell was modeled using the Java Structure Viewer Program (version 1.08lite for Windows) and VRML-View (version 3.0 for Windows)[47, 48] by means of the atomic coordinates listed in Table 2.2. The CaMoO_4 crystals belong to the scheelite-type tetragonal structure (space group $I4_1/a$, No. 88, in the international tables of crystallography, and point-group symmetry C_{4h}^6).[49] In this structure, the molybdenum atoms are coordinated to four oxygens, forming $[\text{MoO}_4]$ clusters with tetrahedral configuration and tetrahedral polyhedra (4 vertices, 4 faces, and 6 edges).[50] These $[\text{MoO}_4]$ clusters are slightly distorted into the matrix, as a consequence of the O–Mo–O bond angles (108.3° and 111.8°), while the calcium atoms are bonded to eight oxy-

gens, resulting in $[\text{CaO}_8]$ clusters with scalenohedral configuration and snub dispenoide polyhedra (8 vertices, 12 faces, and 18 edges).[51] For the construction of the unit cell, lattice parameters were used that showed the smallest deviations related to CaMoO_4 crystals prepared with 50 mL of H_2O and 50 mL of $\text{C}_2\text{H}_6\text{O}_2$. For visual effect, some bonds between the $\text{O}-\text{Ca}-\text{O}$ and $\text{O}-\text{Mo}-\text{O}$ atoms were highlighted in the unit cell.

2.3.3 Fourier Transform Raman/Infrared Spectroscopy Analyses

The group theory calculations showed the presence of 26 different vibrations for the CaMoO_4 crystals, which are represented by equation 2.4 below:[52, 53]

$$\Gamma = 3A_g + 5A_u + 5B_g + 3B_u + 5E_g + 5E_u \quad (2.4)$$

where the A_g , B_g , and E_g are Raman-active vibration modes and the A and B modes are nondegenerate, while the E modes are doubly degenerate. The subscripts (g) and (u) indicate the parity under inversion in centrosymmetric CaMoO_4 crystals. The A_u and E_u modes correspond to the zero frequency of acoustic modes, while the others are optic modes. In addition, the A_g , B_g , and E_g modes arise from the same motion of the CaMoO_4 crystal. Therefore, 13 zone-center Raman-active modes are expected for the CaMoO_4 , as presented by equation 2.5:[54, 55]

$$\Gamma_{(Raman)} = 3A_g + 5B_g + 5E_g \quad (2.5)$$

According to the literature,[56,57] the vibrational modes observed in Raman spectra of molybdates can be classified into two groups: external and internal modes. The vibrational external modes are related to the lattice phonon, which corresponds to the motion of $[\text{CaO}_8]$ clusters and the rigid cell

units. The vibrational internal modes are correspondent to the vibration inside $[\text{MoO}_4]$ cluster units, considering the center of mass in the stationary state. In isolated $[\text{MoO}_4]$, tetrahedrons have a cubic symmetry point (T_d),[58] and its vibrations are composed of four internal modes ($\nu_1(A_1)$, $\nu_2(E_1)$, $\nu_3(F_2)$) and $\nu_4(F_2)$), one free rotation mode $\nu_{f.r.}(F_1)$, and one translation mode (F_2). On the other hand, when a $[\text{MoO}_4]$ tetrahedron is located in the scheelite structure, its point symmetry is reduced to S_4 . [56]

In equation 2.5 the $1A_u$ and $1E_u$ are acoustic or infrared inactive modes, while those for $3B_u$ are forbidden infrared modes. In this situation, only eight infrared-active vibration modes remain, as presented by equation 2.6 [59,60]

$$\Gamma_{(Infrared)} = 4A_u + 4E_u \quad (2.6)$$

Figure 2.3 shows the FT-Raman spectra of CaMoO_4 crystals synthesized by the coprecipitation method with different solvent volume ratios ($\text{H}_2\text{O}/\text{C}_2\text{H}_6\text{O}_2$) and processed in a microwave-assisted hydrothermal/solvothermal system at 140°C for 1 h.

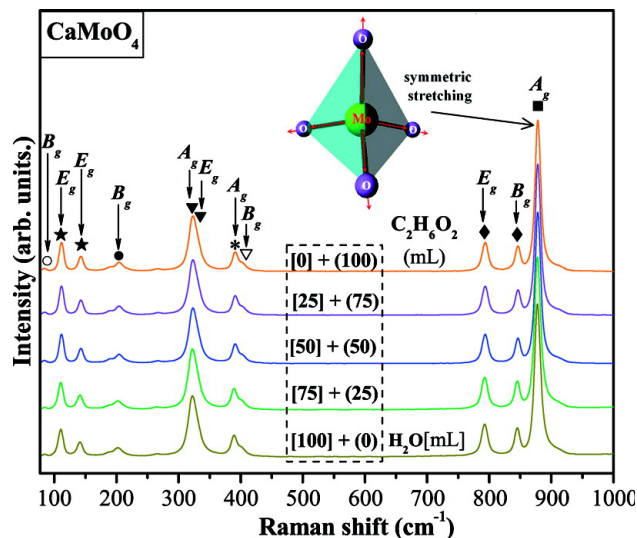


Figure 2.3: FT-Raman spectra in the range from 75 to 1000 cm^{-1} for the CaMoO_4 meso- and nanocrystals prepared with different solvent ratios ($\text{H}_2\text{O}/\text{C}_2\text{H}_6\text{O}_2$) and processed in a microwave-assisted hydrothermal/solvothermal system. The inset shows the $[\text{MoO}_4]$ clusters with symmetric stretching vibration.

As can be illustrated in Figure 2.3, only 11 Raman-active modes were detected; the other ($1B_g$ and $1E_g$) vibration modes were not detectable, probably due to their low intensities. Moreover, the Raman spectra exhibited intense and sharp bands, indicating a strong interaction between the O–Ca–O and O–Mo–O bonds in the clusters.[60, 61] In principle, this characteristic is normally observed in materials structurally ordered at short-range. The inset illustrates a typical $[MoO_4]$ cluster with symmetric stretching vibrations between the O–Mo–O bonds. The positions of each Raman-active mode are listed in Table 2.3.

Table 2.3: Comparative Results between the Experimental Raman-Active Modes of CaMoO_4 Obtained in This Work and Those Reported in the Literature by Different Synthesis Methods^a

M	T (°C)	t (h)	B_g (○)	E_g (★)	E_g (★)	B_g (●)	A_g (▼)	E_g (▼)	A_g (*)	B_g (▽)	E_g (◆)	B_g (◆)	A_g (■)	ref
CZ	1200	40		112	143	205	322	328	391	402	792	845	877	[62]
CZ	1200	24		111.5	143	204.5	321.5	327.5	391	402.5	792	845.5	877	[63]
CP	700	2	86	112	143	204	323		391	402	794	847	878	[64]
MH	140	1	83	110	141	203	322	324	391	401	793	845	878	[□]
MH	140	1	83	110	141	202	322	324	391	401	793	845	878	[□]
MHS	140	1	83	110	141	202	322	324	391	401	793	845	878	[□]
MS	140	1	83	110	141	201	322	324	390	401	793	845	878	[□]
MS	140	1	83	110	141	201	322	324	390	403	793	845	878	[□]

^aSymbols in the column head correspond to the labeled peaks in Figure 2.3; M = method; T = temperature; t = time; Raman modes = (cm^{-1}); CZ = Czochralski; CP = complex polymerization; MH = microwave-hydrothermal, MHS = microwave-hydrothermal-solvothermal, MS = microwave-solvothermal, and [□] = this work.

A closer analysis of the results displayed in this table indicated that the relative positions of all Raman-active modes of CaMoO_4 crystals reported in this work are in good agreement with those previously reported in the literature.[62-64] In fact, the shifts observed on these positions can be correlated to the structural modifications induced by the synthesis methods, mainly including the following: distortions on the $[\text{MoO}_4]$ clusters, the degree of interaction between the O–Mo–O bonds, and variations on the bond lengths, angles and/or symmetry break induced by the structural order–disorder in the lattice.

Figure 2.4 shows the FT-IR spectra of CaMoO_4 crystals synthesized by the coprecipitation method with different solvent volume ratios ($\text{H}_2\text{O}/\text{C}_2\text{H}_6\text{O}_2$) and processed in a microwave-assisted hydrothermal/solvothermal system at 140°C for 1 h.

As was previously described in the text, the molybdates belonging to the scheelite group are able to present up to eight stretching and/or bending vibration modes in infrared spectra.[65, 66] In our case, it was possible to

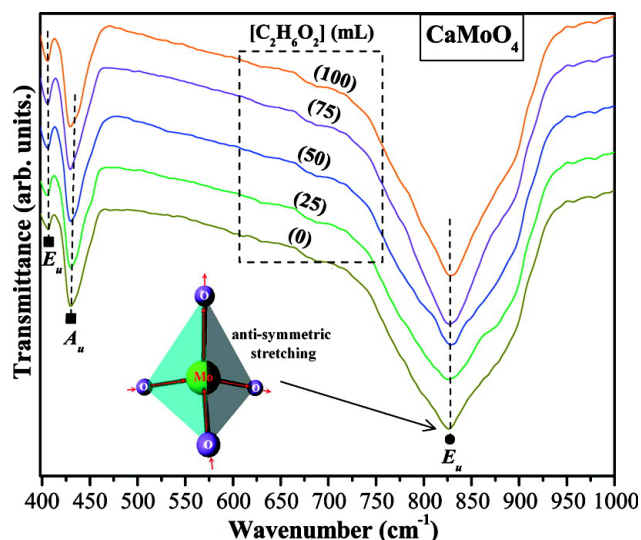


Figure 2.4: FT-IR spectra in the range from 395 to 1000 cm^{-1} for the CaMoO_4 meso- and nanocrystals prepared with different solvent ratios ($\text{H}_2\text{O}/\text{C}_2\text{H}_6\text{O}_2$) and processed in a microwave-assisted hydrothermal/solvothermal system. The inset shows the $[\text{MoO}_4]$ clusters with antisymmetric stretching vibration.

identify no more than three of these modes ($1A_u$ and $2E_u$), which are found in specific positions in the spectra. First, the strong absorption band situated at 827 cm^{-1} (E_u mode) is related to the $\nu_3(F_2)$ internal mode originated from the antisymmetric stretching vibrations in the $[\text{MoO}_4]$ clusters. The other two weak absorption bands located at 405 cm^{-1} (E_u mode) and 430 cm^{-1} (A_u mode) are generally associated with the $\nu_4(F_2)$ internal modes due to the presence of antisymmetric bending vibrations involved in the O–Mo–O bonds. The inset illustrates a characteristic $[\text{MoO}_4]$ cluster with antisymmetric stretching vibrations.

Table 2.4 shows a comparison of the relative positions between the infrared-actives modes of CaMoO_4 obtained in this work with those reported in the literature.[64, 67, 68]

Table 2.4: Comparative Results between the Experimental Infrared Active Modes of CaMoO_4 Obtained in This Work and Those Reported in the Literature by Different Synthesis Methods^a

M	T(°C)	t(h)	E_u (cm^{-1}) (■)	A_u (cm^{-1}) (■)	E_u (cm^{-1}) (●)	ref
CP	700	2		430	820	[64]
HT	120	72		428	821	[67]
SG	900	2		436	818	[68]
MH	140	1	407	430	827	[□]
MH	140	1	405	430	827	[□]
MHS	140	1	406	430	827	[□]
MS	140	1	405	430	827	[□]
MS	140	1	405	430	827	[□]

^a ■ and ● correspond to the labeled peaks in Figure 4; M = method; T = temperature; t = time; CP = complex polymerization; HT = hydrothermal, SG = sol-gel; MH = microwave-hydrothermal, MHS = microwave-hydrothermal-solvothermal, MS = microwave-solvothermal, and [□] = this work.

There is a considerable shift in the position of these vibrations, as indicated in this table, mainly in those E_u modes. Taking into account this observation, this behavior is supposed to be related to the interaction forces between the O–Mo–O bonds and/or distortions on the $[\text{MoO}_4]$ clusters in the lattice.

2.3.4 FEG-SEM Analyses of CaMoO_4 Crystals

Figure 2.5a–l shows the FEG-SEM micrographs of CaMoO_4 crystals prepared with different solvent volume ratios ($\text{H}_2\text{O}/\text{C}_2\text{H}_6\text{O}_2$) and processed in a microwave-assisted hydrothermal/solvothermal system at 140°C for 1 h, respectively.

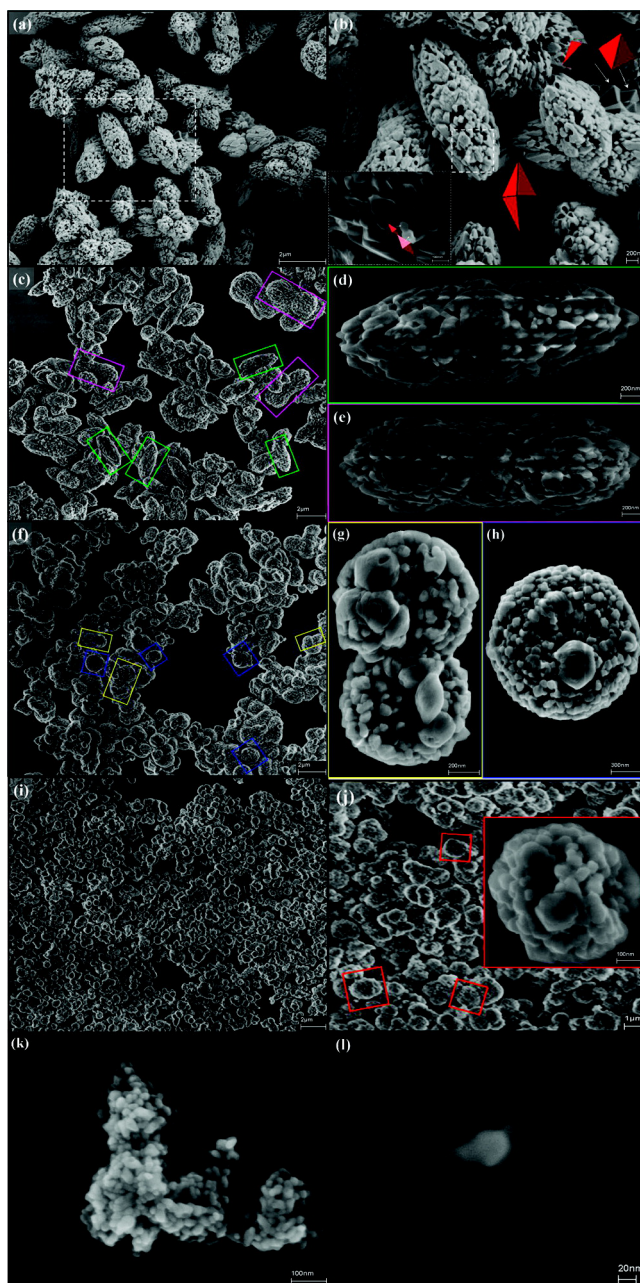


Figure 2.5: (a) Low magnification FEG-SEM micrograph of several CaMoO_4 crystals. (b) High magnification FEG-SEM micrographs of selected area in part a (dotted white square). Inset shows the zoom in part b of CaMoO_4 nanocrystals and nano-octahedrons with well-defined faces prepared with 100 mL of H_2O as solvent. (c) Low magnification FEG-SEM micrograph of several CaMoO_4 crystals prepared with 75 mL of H_2O and 25 mL of $\text{C}_2\text{H}_6\text{O}_2$ as solvents. Pink and green rectangles in part c are illustrated individually by high magnification FEG-SEM micrographs in parts d and e. (f) Low magnification FEG-SEM micrograph of several spherical-like CaMoO_4 mesocrystals prepared with 50 mL of H_2O and 50 mL of $\text{C}_2\text{H}_6\text{O}_2$ as solvents. Blue squares and yellow rectangles in part f are illustrated individually by high magnification FEG-SEM micrographs in parts g and h. (i) Low magnification FEG-SEM micrograph of several quasispherical-like CaMoO_4 nanostructures prepared with 25 mL of H_2O and 75 mL of $\text{C}_2\text{H}_6\text{O}_2$ as solvents. (j) Medium magnification FEG-SEM micrographs of quasi-spherical-like CaMoO_4 nanostructures. Inset in part j (red square) illustrates individual quasi-spherical-like CaMoO_4 nanostructures. (k) Low magnification FEG-SEM micrograph of several CaMoO_4 nanocrystals prepared with 100 mL of $\text{C}_2\text{H}_6\text{O}_2$ as solvent. (l) High magnification FEG-SEM micrographs of CaMoO_4 nanocrystals.

FEG-SEM micrographs were of fundamental importance to understanding the morphological evolution process of CaMoO_4 crystals with the variations in the solvent volume proportions. Figure 2.5a and b indicated the formation of a large quantity of corn-cob-like CaMoO_4 crystals for the synthesis performed only in aqueous solution. Clearly, it can be seen that these structures are essentially constituted of small aggregated particles with octahedral shape, which have been partially oriented and attached on the irregular faces (inset in Figure 2.5b). Under these conditions, it is possible to conclude that several nanocrystallites nucleate and grow into small seed particles. In order to minimize the overall energy of the system, a great number of these seed particles tend to aggregate together.[69-71]

In the synthesis containing 25 mL of $\text{C}_2\text{H}_6\text{O}_2$, the FEG-SEM micrographs confirmed the existence of two distinct types of microcrystals (corn cob and dumbbell shapes), as shown in Figure 2.5c–e. Gong et al.[41] and Chen et al.[72] explained that the formation of dumbbell-like morphologies is associated with the oriented aggregation mechanism, which involves the spontaneous self-organization of adjacent particles along a common crystallographic orientation. On the other hand, these authors explained that during the growth processes these structures are kinetically controlled by means of Ostwald ripening.

For the system containing the same volume of H_2O and $\text{C}_2\text{H}_6\text{O}_2$ (50 mL of each solvent), significant changes were noted with respect to the morphologic shapes. As can be seen in Figure 2.5f–h, the synthesis and MH processing conditions promoted the appearance of spherical-like CaMoO_4 mesocrystals. According to the literature,[73] the mesocrystals are classified as a new class of solid materials, which can be regarded as assemblies of crystallographically oriented nanocrystals with high crystallinity and porosity. Thus, the quantity of $\text{C}_2\text{H}_6\text{O}_2$ employed in this case was sufficient to inhibit the growth

of anisotropic superstructures. In principle, we presume that the continuous adsorption and desorption processes of this organic polymeric compound during the MH processing and the strong interaction between the inorganic faces along preferential crystallographic directions enabled the origin of these mesostructures. Recently, Xu et al.[74] observed nanostructured CaMoO_4 microspheres by means of ionic liquid-assisted synthesis. These authors concluded that the ionic liquid acted as a structure-directing template or surfactant in the formation of these microspheres. The increase in the $\text{C}_2\text{H}_6\text{O}_2$ volume up to 75 mL caused a new modification of the particle morphologies. In the present case, the high concentration of $\text{C}_2\text{H}_6\text{O}_2$ in the aqueous solution has a tendency to limit the interaction between the small particles. As the adsorption and desorption processes on the surface of CaMoO_4 particles are not well-controlled during the MH processing, a random aggregation takes place, with a subsequent growth occurring via aggregation (Figure 2.5 i and j).

The last synthesis, also known as the solvothermal synthesis, was simply performed with $\text{C}_2\text{H}_6\text{O}_2$, i.e., without the presence of H_2O . In this circumstance, the high viscosity of this polymeric substance is able to modify the mobility of the primary particles in suspension as well as its effective collision rates. Moreover, the predominance of $\text{C}_2\text{H}_6\text{O}_2$ in the solution implies a high adsorption of this compound on the inorganic surfaces, which is able to induce a steric hindrance, since this polymer surfactant (ethylene glycol) has a higher viscosity in relation to that of water (see Supporting Information Figure SI-1). Probably, this chemical event leads to a minimizing in the growth process, causing a reduction of the particle sizes. Afterward, as $\text{C}_2\text{H}_6\text{O}_2$ has good interaction with microwave radiation at frequencies of 2.45 GHz, it is acceptable that this physical phenomenon causes the presence of localized superheating in the liquid phase,[75-77] leading to a disordered aggregation or crystallographic fusion

of the nanoparticles (Figure 2.5k and l). These nanocrystals present large surface area and N_2 absorption in relation to the case of oriented aggregate crystals (see Supporting Information Figures SI-2 and 3).

2.3.5 TEM Analyses of $CaMoO_4$ Crystals

Figure 2.6 shows the TEM/HR-TEM micrographs and SAED patterns of $CaMoO_4$ crystals prepared with different solvent volume ratios ($H_2O/C_2H_6O_2$) and processed in the microwave-assisted hydrothermal/solvothermal system at $140^\circ C$ for 1 h, respectively.

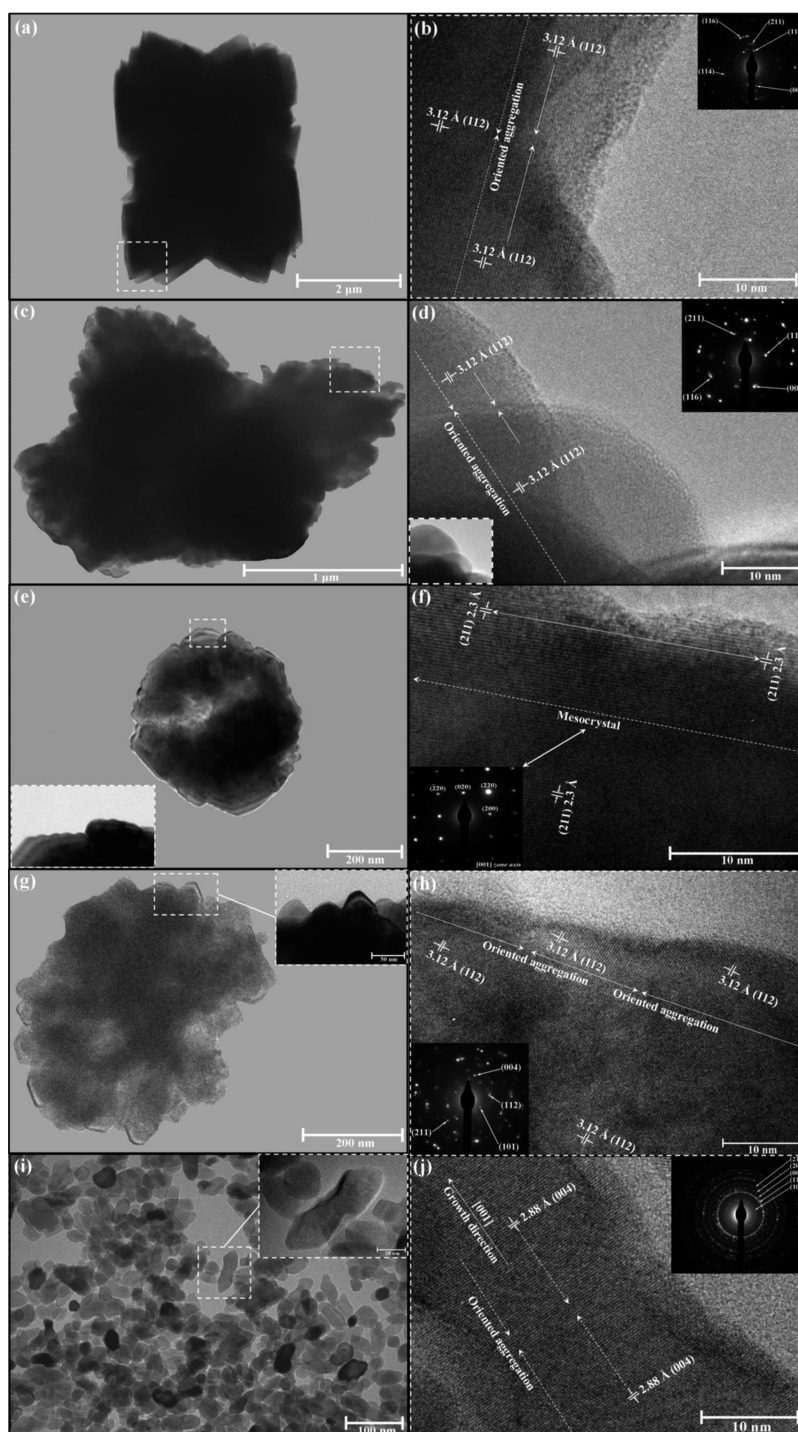


Figure 2.6: (a) Low magnification TEM micrographs of CaMoO_4 crystals synthesized in aqueous solution. (b) HR-TEM micrograph performed on the edge of a crystal (dotted white square) (inset shows the corresponding SAED pattern). (c) TEM micrographs of CaMoO_4 crystals synthesized with different solvent volume ratios: 75 mL of H_2O /25 mL of $\text{C}_2\text{H}_6\text{O}_2$. (d) HR-TEM micrograph performed on the edge of a crystal (dotted white square) (inset shows the corresponding SAED pattern). (e) TEM micrographs of CaMoO_4 mesocrystals synthesized with different solvent volume ratios: (50 mL of H_2O /50 mL of $\text{C}_2\text{H}_6\text{O}_2$). (f) HR-TEM micrograph performed on the edge of a mesocrystal (dotted white square) (inset shows the corresponding SAED pattern). (g) TEM micrographs of CaMoO_4 crystals synthesized with different solvent volume ratios: 25 mL of H_2O /75 mL of $\text{C}_2\text{H}_6\text{O}_2$. (h) HR-TEM micrograph performed on the edge of a crystal (dotted white square) (inset shows the corresponding SAED pattern). (i) TEM micrographs of CaMoO_4 crystals synthesized with 100 mL of $\text{C}_2\text{H}_6\text{O}_2$. (j) HR-TEM micrograph performed on the two nanocrystals when aggregation oriented (dotted white square) (inset shows the corresponding SAED pattern).

Figure 2.6a illustrates the low magnification TEM micrographs of corn-cob-like CaMoO_4 oriented aggregate crystals obtained only in the presence of H_2O (100 mL). In this micrograph, the dark areas are related to the high concentration of small octahedron-like particles with aggregate nature, confirming also that these microstructures are not internally hollow[78] (Figure 2.6a and Supporting Information Figure SI-4(a)). HR-TEM performed in the corner of these corn-cob-like morphologies (dashed white square in Figure 2.6a and b) revealed an oriented aggregation of two small particles exactly in the (112) plane, as estimated by the planar spacing of 3.12 Å. However, the SAED showed a characteristic polycrystalline diffraction pattern (inset Figure 2.6b), suggesting that the assemblies of particles were randomly organized in the formation stages of corn-cob-like microcrystals (Supporting Information Figure SI-4(b-d)). Additionally, other TEM micrographs demonstrated that the growth occurs preferentially along the [001] direction. In principle, a more precise analysis of the TEM/HR-TEM micrographs and SAED data illustrated in Figure 6c and d suggested that the CaMoO_4 crystals obtained in the synthesis with 75 mL of H_2O have the same behavior as that of those specifically obtained in aqueous solution (Figure 6a and b; also see Supporting Information Figure SI-4(e,f)). As was expected, the spherical-like shapes are observed in the dark area in the TEM micrographs, signifying that these morphologies are constituted by a discrete accommodation of several particles. In contrast with the other obtained morphologies, the HR-TEM microscopy carried out on an exterior part showed a region with perfect attachment and alignment between two particles (Figure 2.6e and f). We presume that the growth process conducted by the microwave heating increased the effective collision rates, producing irreversible oriented attachments if the particles achieve a congruent alignment in the interface.[79] An important observation was possible through the HR-TEM

and SAED techniques, where the chosen region (dashed white square and inset in Figure 2.6e) revealed that the attachments occurred in the (211) plane, according to the planar spacing of 2.3 Å (Figure 2.6f and Supporting Information Figures SI-4(g,h)). A significant point verified in the SAED was the evidence of a general single-crystal pattern for the octahedral-like crystal, [80, 81] supporting the existence of mesostructures for this system formed with equivalent volume ratios ($\text{H}_2\text{O}/\text{C}_2\text{H}_6\text{O}_2$). Taking into consideration the solution composed of 25 mL of H_2O and 75 mL of $\text{C}_2\text{H}_6\text{O}_2$, the TEM images provided a possible random stacking of particles as shown in Figure 2.6g and supported by the FEG-SEM measurements (Figures 2.5i and 2.5j). In this system, the HR-TEM micrographs allowed us to assume that, after collision events, some particles tend to remain attached in compatible crystallographic planes. In the case illustrated in Figure 2.6h, the oriented aggregation happened along the (112) plane. On the other hand, the diffraction pattern obtained by the SAED technique in the selected fraction in Figure 2.6h (dashed white square) (see Supporting Information Figure SI-4(i,j)) confirmed that these morphologies do not have an analogous characteristic of microcrystals. A large polydisperse distribution of irregular nanoparticles was visualized in the TEM images (Figure 2.6i). Also, choosing some of these particles (dashed white square and inset in Figure 2.6i), the presence of oriented aggregation due to the junction detected in the interface contact between the nanoparticles was found by HR-TEM measurements (corresponding to a crystallographic distance of approximately 2.88 Å) (Figure 2.6j). As was presumed, this particle system has a polycrystalline behavior because of the different crystallographic orientations identified in the SAED patterns (Supporting Information Figure SI-4(k,l)). According to Yu et al., [82] the morphological changes could be ascribed to selective interaction or adsorption of polymer molecules on certain crystal faces of scheelite, resulting in different

modes of crystal growth along different crystallographic directions.

2.3.6 Average Size Distribution of CaMoO_4 Crystals

FEG-SEM micrographs were also of great importance to evaluate the average particle size distribution of different CaMoO_4 crystals obtained in this work. Hence, the counting of 100 crystals was performed to ensure a good statistic response (Figure 2.7).

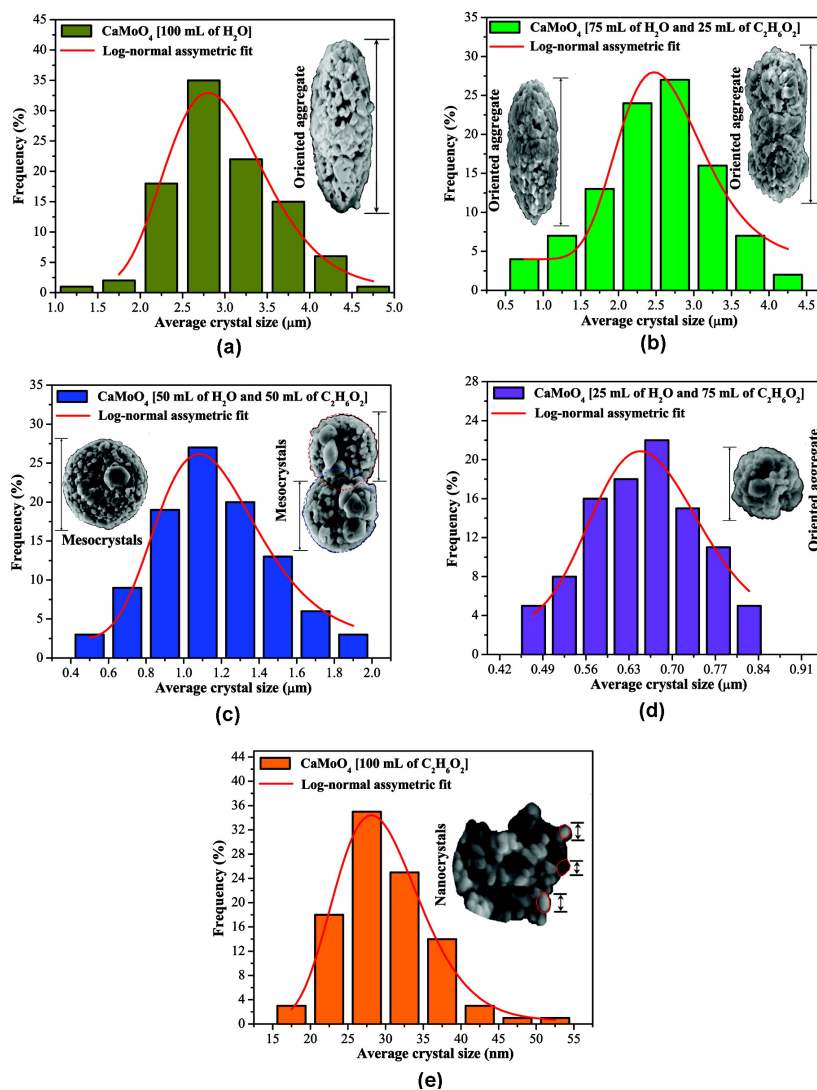


Figure 2.7: Average size distribution of CaMoO_4 meso- and nanocrystals prepared with different solvent ratios ($\text{H}_2\text{O}/\text{C}_2\text{H}_6\text{O}_2$) and processed in a microwave-assisted hydrothermal/solvothermal system: (a) 100 mL of H_2O , (b) 75 mL of H_2O and 25 mL of $\text{C}_2\text{H}_6\text{O}_2$, (c) 50 mL of H_2O and 50 mL of $\text{C}_2\text{H}_6\text{O}_2$, (d) 25 mL of H_2O and 75 mL of $\text{C}_2\text{H}_6\text{O}_2$, and (e) 100 mL of $\text{C}_2\text{H}_6\text{O}_2$.

In all cases, the counting of particle sizes was well-described by the log–normal distribution:

$$y = y_0 + \frac{A}{\sqrt{2\pi wx}} e^{-[\ln \frac{x}{x_c}]^2 / 2w^2} \quad (2.7)$$

where y_0 is the first value on the y-axis, A is the amplitude, w is the width, π is a constant, and x_c is the center value of the distribution curve on the x-axis.

The corn-cob-like CaMoO_4 crystals formed only in H_2O exhibited an average size distribution in the range from 1.25 to 4.75 μm (Figure 2.7a and inset). In this system, it was estimated that 35% of these structures have an average size of approximately 2.75 μm . The addition of 25 mL of $\text{C}_2\text{H}_6\text{O}_2$ into the aqueous solution (75 mL) resulted in two types of corn-cob-like crystals, where their sizes are situated in the range from 0.75 to 4.25 μm (Figure 2.7b and insets). As can be seen in Figure 2.7c, the CaMoO_4 mesocrystals presented an average size distribution from 0.5 to 1.9 μm ; that is, 27% of these mesocrystals have an average size of 1.1 μm . The predominance of CaMoO_4 (75 mL) in the chemical synthesis promoted a reduction in the crystal size (from 0.475 to 0.825 μm) (Figure 7d and inset). In contrast, as was previously described in the text, the high adsorption of $\text{C}_2\text{H}_6\text{O}_2$ on the CaMoO_4 surfaces caused a significant morphologic change, i.e., inducing the formation of irregular nanoparticles with 35% of nanocrystals have an average size of 27.5 nm (Figure 2.7e and inset).

2.3.7 Growth Mechanism of CaMoO_4 Crystals

Figure 2.8 shows a schematic representation of all stages involved in the synthesis and growth mechanism of CaMoO_4 crystals synthesized by the coprecipitation method at room temperature and processed in a microwave-

assisted hydrothermal/solvothermal system at 140°C for 1 h.

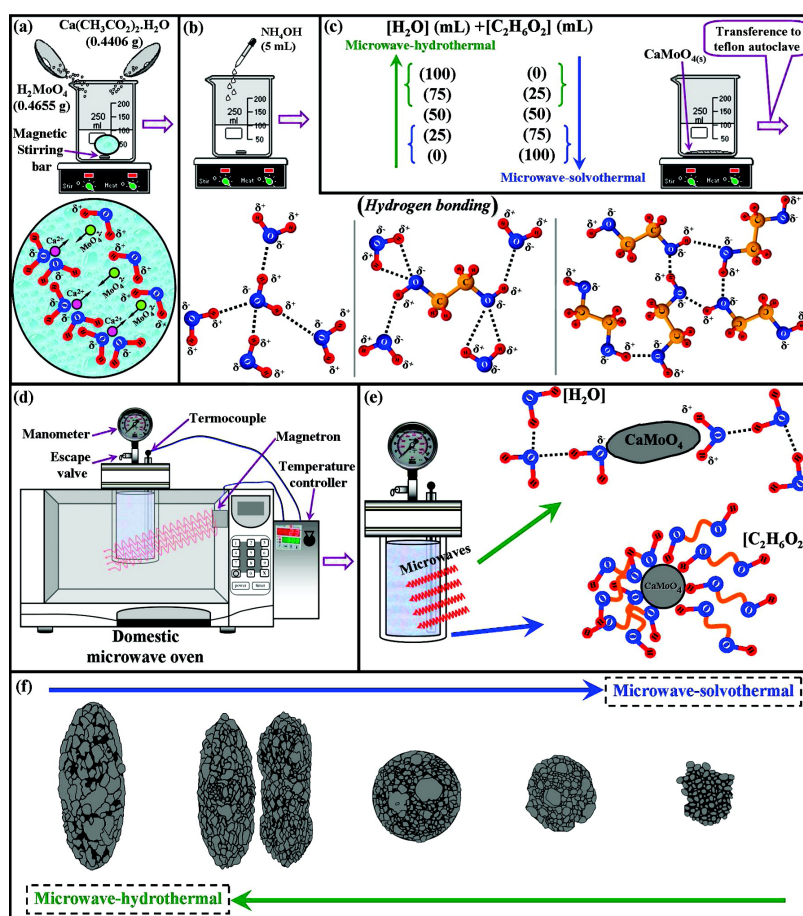


Figure 2.8: Schematic representation of the synthesis, processing, and growth mechanism of CaMoO_4 meso- and nanocrystals: (a) chemical synthesis (solvation and coprecipitation reaction), (b) increase of precipitation rate with NH_4OH and different types of hydrogen bonds between H_2O and/or $\text{C}_2\text{H}_6\text{O}_2$, (c) the different solvent ratios ($\text{H}_2\text{O}/\text{C}_2\text{H}_6\text{O}_2$) employed in preparation of CaMoO_4 meso-/nanocrystals and transference to a Teflon autoclave, (d) domestic microwave-assisted hydrothermal/solvothermal system employed in the processing of CaMoO_4 meso-/nanocrystals, (e) increase of the effective collision rates between the nano- and microcrystals with heating by action of the microwave irradiation and possible involvement of solvent molecules on the crystals, causing steric hindrance, orientation, and trapping of small nanocrystals, promoting anisotropic/isotropic growth, and (f) meso-/nanocrystal growth evolution as a function of processing in microwaves with different solvent ratios ($\text{H}_2\text{O}/\text{C}_2\text{H}_6\text{O}_2$).

Figure 2.8a illustrates the initial synthesis method, with the addition of stoichiometric amounts of respective reagents [H_2MoO_4 and $\text{Ca}(\text{CH}_3\text{CO}_2)_2 \cdot \text{H}_2\text{O}$]. In order, these reagents were dissolved in deionized water under constant stirring. In this solution, the energy of solvation of H_2O molecules promotes rapid salt dissociation and acid ionization, where the Ca^{2+} and MoO_4^{2-} ions are quickly solvated by H_2O molecules. The partial negative

charges on the H₂O molecules are electrostatically attracted by Ca²⁺ ions, while the partial positive charges on the H₂O molecules are electrostatically attracted by MoO₄²⁻ ions (inset of Figure 2.8a). However, due to the difference of the electronic density of the Ca²⁺ and MoO₄²⁻ ions, a strongest force electrostatic attraction occurs between both, resulting in the formation of the first CaMoO₄ precipitates. In the following, the precipitation rate was increased by the addition of 5 mL of NH₄OH into this solution (Figure 2.8b). Also, in this same figure, we can note that the presence of different solvent ratios (H₂O/C₂H₆O₂) can lead to several possibilities of intermolecular interactions (hydrogen bonding). In the first case, the interactions between the H₂O molecules are stronger due to hydrogen bonds and the difference of electronegativity between atoms (H and O). These create highly polar bonds with hydrogen, which leads to strong bonding between hydrogen atoms (H δ+) on one molecule and the lone pairs of oxygen atoms (O δ-) on adjacent H₂O molecules.[83-85] It is verified that each H₂O molecule can potentially form four hydrogen bonds with surrounding H₂O molecules. There are exactly a sure number of δ+ hydrogens and lone pairs so that every one of them can be involved in hydrogen bonding.[86] In the second case, the presence of hydrogen bonding for the system also is noted (ethylene glycol and water), and each ethylene glycol molecule can potentially form four hydrogen bonds with surrounding H₂O molecules.[71] In the third case, also we observed the presence of hydrogen bonding between the ethylene glycol, and its hydrophilic characteristics are due to hydrogen bonds among the OH bonds.[87] In ethylene glycol molecules, each pair of OH groups is able to form hydrogen bonding with other OH groups, due to a difference of electronegativity between the atoms (O δ- and H δ+); thus, this chemical bond presents a certain polarity.[88, 89] In Figure 2.8c, the effect of solvent ratios on the processing of CaMoO₄ oriented aggregate crystals and meso- and nanocrystals can be ob-

served. In the range using from 100 to 75 mL of H₂O as solvent, the microwave-hydrothermal method is used; with 50 mL of H₂O and 50 mL of C₂H₆O₂, the solvothermal–microwave–hydrothermal method is used; and in the range using from 100 to 75 mL of C₂H₆O₂ as solvent, the solvothermal–hydrothermal method is used. In all the methods employed, the obtained CaMoO₄ coprecipitated. After this step, these systems were stirred for 30 min and transferred to the Teflon autoclave. Figure 2.8d illustrates a schematic representation of the domestic microwave system employed in the processing of the CaMoO₄ oriented aggregate crystals and meso- and nanocrystals (see Supporting Information Figure SI-5). This apparatus was developed via several adaptations performed on a domestic microwave oven (model NN-ST357WRPH Piccolo 22 L, Panasonic). In Figure 2.8e, inside this system, the high frequency of the microwave irradiation interacts with the permanent dipoles of the liquid phases (H₂O and/or C₂H₆O₂), which initiates a rapid heating resulting from the resultant molecular rotation. Likewise, permanent or induced dipoles in the dispersed phase cause a rapid heating of the particles.[90, 91] Thus, the microwave irradiation is able to promote the effective collision between the nanoparticles, contributing to growth of the oriented aggregate crystals and meso- and nanocrystals. The adsorption of H₂O and/or C₂H₆O₂ on the CaMoO₄ nanoparticle surfaces favors the aggregation process by means of the van der Waals interaction of the hydrogen bonds of solvent with the OH groups and polarizations of nearby nanoparticles. Figure 2.8f illustrates the morphological evolution and anisotropic growth of a CaMoO₄ oriented aggregate with the employment of H₂O as solvent and the isotropic growth of CaMoO₄ meso- and nanocrystals with the employment of C₂H₆O₂ as solvent.[92]

2.3.8 UV–Visible Absorption Spectroscopy Analyses of CaMoO_4 Crystals

Parts a–e of Figure 2.9 show the UV–vis absorbance spectra of CaMoO_4 crystals prepared with different solvent volume ratios ($\text{H}_2\text{O}/\text{C}_2\text{H}_6\text{O}_2$) and processed in a microwave-assisted hydrothermal/solvothermal system at 140°C for 1 h, respectively. The found optical band values as a function of different types of solvent ratios are shown in Figure 2.9f.

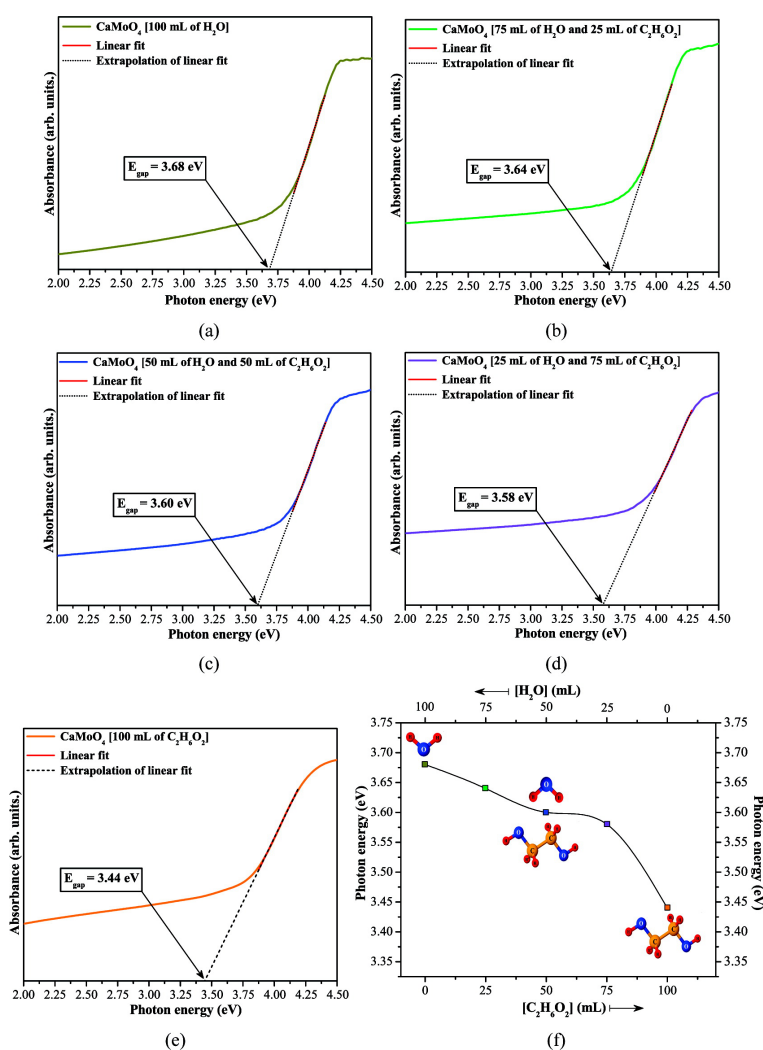


Figure 2.9: UV–vis absorbance spectra of CaMoO_4 crystals prepared with different solvent ratios ($\text{H}_2\text{O}/\text{C}_2\text{H}_6\text{O}_2$) and processed in a microwave-assisted hydrothermal/solvothermal system: (a) 100 mL of H_2O , (b) 75 mL of H_2O and 25 mL of $\text{C}_2\text{H}_6\text{O}_2$, (c) 50 mL of H_2O and 50 mL of $\text{C}_2\text{H}_6\text{O}_2$, (d) 25 mL of H_2O and 75 mL of $\text{C}_2\text{H}_6\text{O}_2$, (e) 100 mL of $\text{C}_2\text{H}_6\text{O}_2$, and (f) optical band values as a function of different solvent ratios.

The optical band gap energy (E_{gap}) was estimated by the method proposed by Wood and Tauc.[93] According to these authors, the E_{gap} is associated with absorbance and photon energy by the following equation:

$$h\nu\alpha \propto (h\nu - E_{gap})^n \quad (2.8)$$

where α is the absorbance, h is the Planck constant, ν is the frequency, E_{gap} is the optical band gap and n is a constant associated with the different types of electronic transitions ($n = 1/2, 2, 3/2,$ or 3 for direct allowed, indirect allowed, direct forbidden, and indirect forbidden transitions, respectively). The literature explains that the[94] molybdates have an optical absorption process governed by direct electronic transitions. In this phenomenon, the electronic charges located in the maximum-energy states in the valence band (VB) go to the minimum-energy states in the conduction band (CB) after an absorption process but occurring always in the same region of the Brillouin zone.[95] Based on this information, the E_{gap} values of CaMoO_4 crystals were calculated using $n = 1/2$ in equation 2.8. The obtained data are illustrated in Figure 2.9 and listed in Table 2.5. In addition, this table also shows a comparison between the E_{gap} obtained in this work and those reported in the literature.[64, 96-98]

Table 2.5: Comparative Results between the Optical Band Gap Energy (Experimental and Theoretical) of CaMoO_4 Obtained in This Work and Those Reported in the Literature by Different Synthesis Methods^a

M	shape	T(°C)	t(h)	E_{gap} (eV)	ref
CP	nanopowders	400	2	5.09	[64]
CP	nanopowders	500	2	4.87	[64]
CP	nanopowders	600	2	5.18	[64]
CP	nanopowders	700	2	5.16	[64]
CZ	crystal	1400	24	5.0	[96]
PLA	nanoparticles	900	3	4.70	[97]
PP	spherical	450	4	2.90	[98]
PP	spherical	500	4	3.70	[98]
PP	spherical	600	4	4.20	[98]
PP	spherical	700	4	4.70	[98]
MH	corn-cob-like	140	1	3.68	[□]
MH	dumbbell-like	140	1	3.64	[□]
MHS	spherical-like	140	1	3.60	[□]
MS	quasi-spherical-like	140	1	3.58	[□]
MS	nanoparticles	140	1	3.44	[□]
	theoretical displacement of Mo (0.0 Å)			4.64	[□]
	theoretical displacement of Mo (0.1 Å)			4.49	[□]
	theoretical displacement of Mo (0.15 Å)			4.36	[□]
	theoretical displacement of Mo (0.2 Å)			4.2	[□]
	theoretical displacement of Mo (0.25 Å)			4.02	[□]
	theoretical displacement of Mo (0.3 Å)			3.81	[□]
	theoretical displacement of Mo (0.35 Å)			3.57	[□]
	theoretical displacement of Mo (0.4 Å)			3.47	[□]

^aM = method; T = temperature; t = time; E_{gap} = optical band gap; CP = complex polymerization; CZ = Czochralski; PLA = pulsed laser ablation; PP = polymeric precursor; MH = microwave-hydrothermal; MHS = microwave-hydrothermal-solvothermal; MS = microwave-solvothermal; [□] = this work.

As can be seen from Table 2.5, the E_{gap} values of CaMoO_4 oriented aggregate crystals and meso- and nanocrystals are smaller than most E_{gap} values of CaMoO_4 reported in the literature.[64, 96-98] This behavior can be related to the presence of different defect densities on the CaMoO_4 prepared by different methods. These preparation methods lead to the obtention of CaMoO_4 with different (shape, average crystal size, and structural order–disorder) degrees in the lattice. Therefore, also these factors promoted the formation of intermediary energy levels within the band gap. In our case, the small E_{gap} values found for

CaMoO₄ oriented aggregate crystals and meso- and nanocrystals can be due to distortions on the lattice caused by microwave irradiation coupled with the [MoO₄] clusters.[99] Also, the modifications of the crystal morphologies by different solvent ratios can lead to the formation of new intermediary electronic states within the band gap.[100]

2.3.9 Band Structures of the Crystalline CaMoO₄ Phase without and with Displacements Theoretically Induced on the Mo Atoms

Figure 2.10 illustrates the calculated band structures of the crystalline CaMoO₄ phase without and with displacements performed on Mo atoms. In order to calculate the E_{gap} value corresponding to the distorted lattices, a displacement of 0.35 Å on the Mo atoms was necessary along the x-, y-, and z-axes (0.05 Å, -0.25 Å, and -0.24 Å) into the primitive cell.

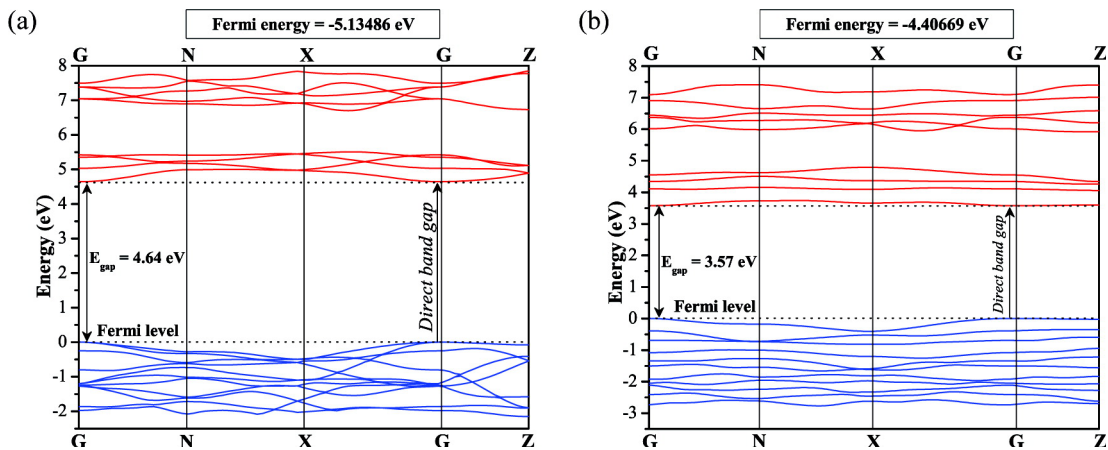


Figure 2.10: Calculated band structures of the crystalline CaMoO₄ phase without (a) and with (b) displacements on the Mo atoms.

The calculated E_{gap} exhibited considerable differences when both the structures were compared. As was expected, the theoretical calculations in-

indicated an E_{gap} of 4.64 eV for the crystalline CaMoO_4 phase without the presence of structural defects or distortions (Figure 2.10a), while in the distorted structure (Mo atom displaced of 0.35 Å) this value was approximately 3.57 eV (Figure 2.10b). Therefore, these data confirm that this reduction in the E_{gap} is associated with the appearance and redistribution of intermediary energy levels between the valence band (VB) and conduction band (CB) (see Figure 2.10). According to the theoretical calculations, the band structures modeled in both cases indicated a direct electronic transition as a consequence of this physical phenomenon occurring in the same region in the Brillouin zone (Γ Point \rightarrow Γ Point) (see Supporting Information Figure SI-6). The theoretical results reported in this work showed good agreement with those experimentally obtained (see Table 2.5 and Supporting Information Figure SI-7).

2.3.10 Density of States for the Crystalline CaMoO_4 Structure without and with Displacements Theoretically Induced on the Mo Atoms.

Figure 2.11 shows the density of states (DOS) calculated at the DFT level for crystalline CaMoO_4 without and with displacement on the Mo atoms, promoting distortions into the $[\text{MoO}_4]$ clusters, respectively.

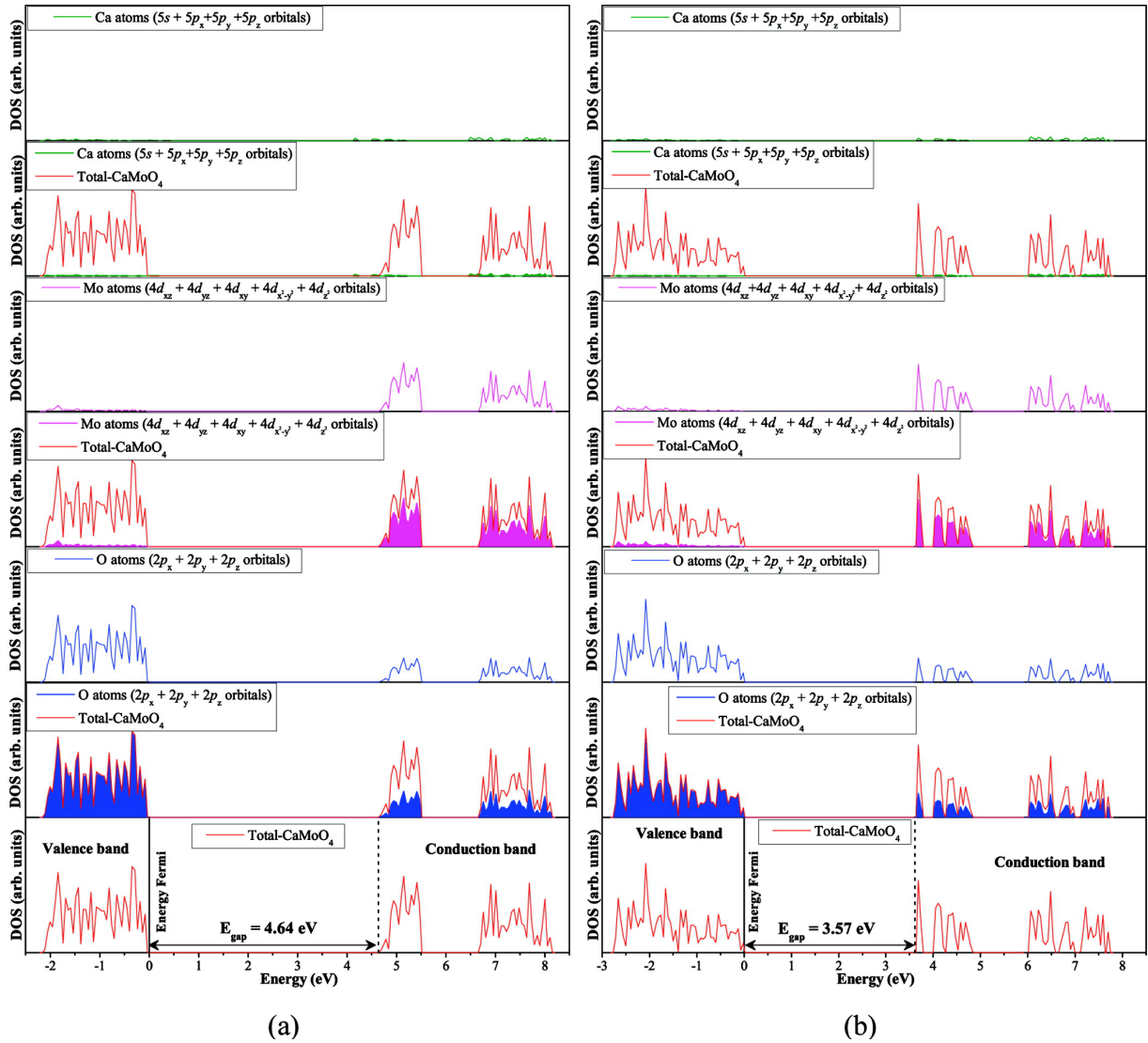


Figure 2.11: Total DOS of crystalline structure CaMoO_4 without (a) and with (b) displacements on the Mo atoms.

In Figure 2.11 it was noted that the DOS of crystalline structure CaMoO_4 without (a) and with (b) displacement on the Mo atoms has the VB predominantly composed of oxygen (O) $2p_x$, $2p_y$, and $2p_z$ atomic orbitals, while the CB is mainly formed of molybdenum (Mo) $4d_{xy}$, $4d_{xz}$, $4d_{yz}$, $4d_{x^2-y^2}$, and $4d_{z^2}$ atomic orbitals. As can be observed in Figure 2.11a, the calcium (Ca) $5s$, $5p_x$, $5p_y$, and $5p_z$ atomic orbitals have a minimal contribution (between -3 and 9 eV) due to a weak hybridization between the Ca and O orbitals. Also, the total DOS of all orbitals for the CaMoO_4 showed that those arising from the Ca atoms have few contributions between the intermediary energy states because of the

ionic character of its chemical bond (Ca-O) (see Figure 2.11b and Supporting Information Figure SI-8 and 9). The Mo 4d atomic orbitals present two different types of energy levels. The projected individual DOS of each Mo atomic orbital revealed that the CB is basically constituted of $4d_{x^2-y^2}$ and $4d_{z^2}$ orbitals (from 4.64 to 5.51 eV) as well as $4d_{xy}$, $4d_{xz}$, and $4d_{yz}$ atomic orbitals (from 6.65 to 8.15 eV) (see Supporting Information Figure SI-8). In principle, the theoretical data suggested a strong hybridization between the O 2p (above the VB) and Mo 4d orbitals (near the CB), respectively. After displacement of 0.35 Å caused on the Mo atoms, a significant change in the DOS was noted, consequently reducing the E_{gap} (3.57 eV). Figure 2.11b illustrates the reorganization of the intermediary energy levels in the valence ($2p_x$, $2p_y$, and $2p_z$) and conduction ($4d_{xy}$, $4d_{xz}$, $4d_{yz}$, $4d_{x^2-y^2}$, and $4d_{z^2}$) bands. In this distorted CaMoO_4 lattice, the O atoms are more distant from those of Mo atoms (see also Supporting Information Figure SI-9).

2.3.11 Photoluminescence Properties Analyses: Distortions on the $[\text{MoO}_4]$ Clusters in the Lattice by Microwave Irradiation and a Wide Band Model

In the last years, the experimental and theoretical results reported in the literature have tried to explain the possible mechanisms responsible for the PL properties of molybdates.[101-108] Blasse,[101] Chandrasekhar, and White[102] explained the PL emissions of CaMoO_4 by means of a model containing both metal and ligand orbitals. In this model, the charge transfer processes in these orbitals were considered the key factors for the origin of this optical property. Mikhailik et al.[103, 104] interpreted the PL properties of

CaMoO_4 as a radiative recombination of electron–hole pairs localized into the MoO_4^{2-} groups. Liu et al.[105] and Lei et al.[106] reported that the charge-transfer transitions into the $[\text{MoO}_4]^{2-}$ complex can be considered the main reason for the green PL emissions of CaMoO_4 . Recently, Thongtem et al.[107] attributed the PL emission of CaMoO_4 nanopowders with ${}^1\text{T}_2 \rightarrow {}^1\text{A}_1$ electronic transitions to the MoO_4^{2-} anions, which can be treated as excitons. However, all these explanations are directly associated with the MoO_4^{2-} groups (ions), but the CaMoO_4 is a crystalline solid composed of interconnected clusters ($\dots[\text{MoO}_4]-[\text{CaO}_8]-[\text{MoO}_4]\dots$). Therefore, in our work, we assume that the tetrahedral $[\text{MoO}_4]$ clusters can be distorted because the Mo atoms have good interactions with microwave irradiation.[108] As there is an interconnection of the $[\text{MoO}_4]$ and $[\text{CaO}_8]$ clusters in the tetragonal structure, it is possible to conclude that any distortion caused on the $[\text{MoO}_4]$ cluster also promotes a slight deformation of the Ca–O bonds. However, the ionic nature (radial character) exhibited by the $[\text{CaO}_8]$ clusters prevents a high degree of distortions on them (see Figure 2.2 and Supporting Information Figures SI-5, 8, and 9). These distortions are able to induce a symmetry break in the lattice, leading to the appearance of intermediate levels within the band gap. Also, other factors, such as inhomogeneous crystal size distribution, the crystallographic orientation of crystals, and changes in morphology (see Supporting Information Figure SI-5), can promote a charge gradient and polarization on the crystal surfaces, causing the formation of these intermediate levels that are necessary for recombination processes (electron–hole) and favoring PL emission at room temperature in CaMoO_4 oriented aggregate crystals and meso- and nanocrystals.

Figure 2.12 shows the representation for the CaMoO_4 unit cell, possible distortion sets on the $[\text{MoO}_4]$ clusters, laser excitation, a wide band model, and the PL spectrum of CaMoO_4 oriented aggregate crystals and meso-

and nanocrystals prepared with different solvent ratios ($\text{H}_2\text{O}/\text{C}_2\text{H}_6\text{O}_2$) and processed in a microwave-assisted hydrothermal/solvothermal system at 140°C for 1 h.

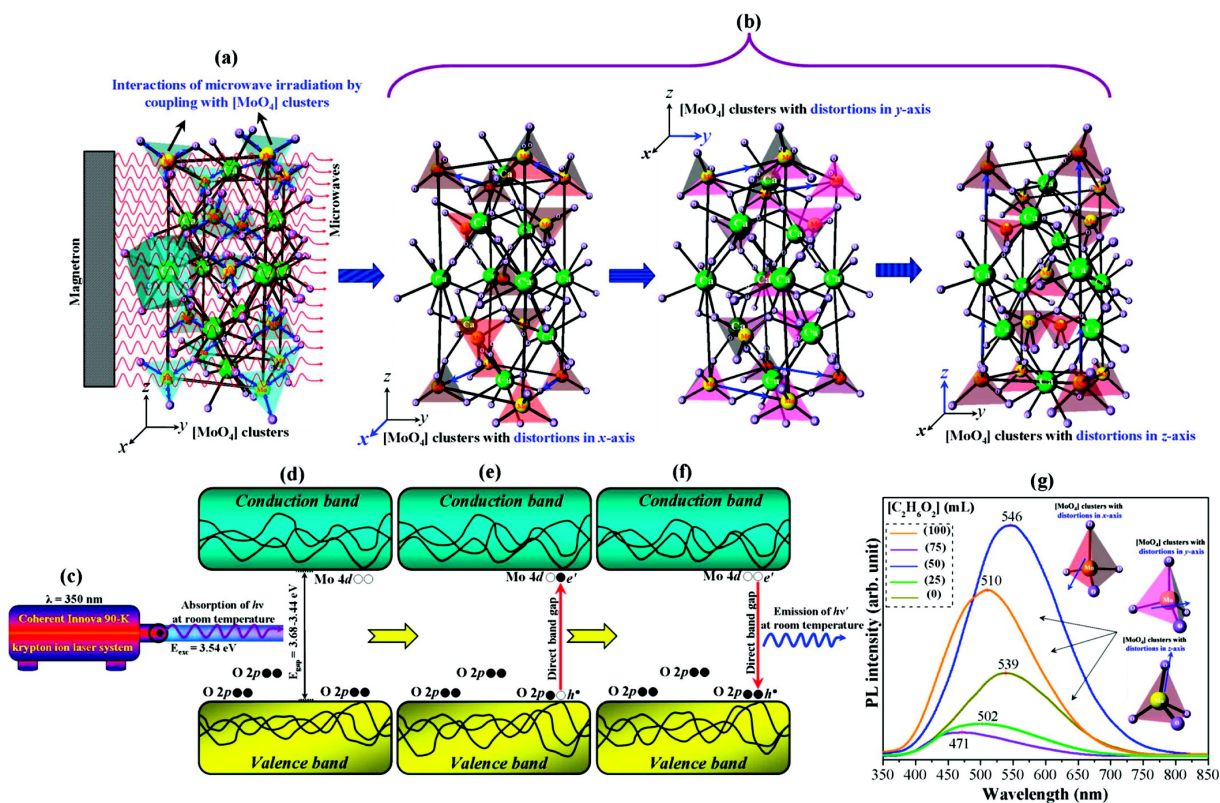


Figure 2.12: (a) Schematic representation of the unit cell under microwave irradiation, (b) possible distortion sets on the $[\text{MoO}_4]$ clusters into the lattice caused by coupling with microwave irradiation, (c) wavelength employed in the excitation process of CaMoO_4 meso- and nanocrystals, (d) proposed wide band model before excitation with the presence of intermediary energy levels, (e) electronic transition from oxygen 2p orbitals (lower energy levels) to molybdenum 4d orbitals (higher energy levels) by absorption of $(h\nu)$ at room temperature, (f) emission process of photons $(h\nu')$ because of the radiative return processes of electrons situated at molybdenum 4d orbitals to oxygen 2p orbitals, and (g) PL spectra of CaMoO_4 meso- and nanocrystals prepared with different solvent ratios ($\text{H}_2\text{O}/\text{C}_2\text{H}_6\text{O}_2$). Inset shows the distorted MoO_4 clusters in the x, y, and z axes.

Inside the autoclave cell, the high frequency of the microwave irradiation may also interact with the lattice of the CaMoO_4 crystal solid (Figure 2.12a). It is reported by Rao et al.[108] that Mo atoms are known to couple strongly to microwave irradiation at ordinary temperatures; this coupling generates high heating inside the lattice, which can lead to deformation/strain in the CaMoO_4 lattice; some of these possible distortions on the tetrahedron $[\text{MoO}_4]$

clusters were simulated through displacements on the Mo atoms along the axes (x, y, and z) illustrated in Figure 2.12b. Therefore, this structural distortion leads to formation of intermediary energy levels within the band gap. Figure 2.12c shows the laser employed in excitation of CaMoO₄ meso-/nanocrystals. The wavelength energy (350 nm \approx 3.543 eV) is able to excite several electrons localized in intermediary energy levels within the band gap (Figure 2.12d). These direct electronic transitions in band gap occur in the same region of the Brillouin zone between the maximum-energy states near to minimum-energy states (see Figure 2.10). During the excitation process at room temperature, some electrons localized at lower intermediary energy levels (oxygen 2p orbitals) near the valence band absorb the photon energies ($h\nu$) at this wavelength. As a consequence of this phenomenon, the energetic electrons are promoted to higher intermediary energy levels (molybdenum 4d orbitals) located near the conduction band (Figure 2.12e). When the electrons fall back to lower energy states, again via radiative return processes, the energies arising from this electronic transition is converted to photons ($h\nu'$) (Figure 2.12f). In this case, several photons ($h\nu'$), originating from the participation of different energy states during the electronic transitions, are responsible for the broad PL spectra (Figure 2.12g). As can be observed in Figure 2.12, the PL emission maximum also is influenced by the morphology of the crystals, depending on the shape and arrangement of clusters having different types of defects in surface and lattice. Since the distortion on the tetrahedral [MoO₄] clusters leads to specific defects at medium range, causing a nonlinear PL behavior, according to Yin et al.,[109] the PL intensity in a CaMoO₄ nanostructure may greatly depend on the particle distribution. These authors have demonstrated that the improvement in PL intensity of CaMoO₄ can be related with the control of the particle size distribution and the homogeneity of particle morphology. Our results indicated that the

spherical-like CaMoO_4 mesocrystals with isotropic growth present the largest intensities of PL emission. Thus, we believe that PL behavior can also be influenced by effective control of the orientation of these crystals. However, the true factor that acts on the PL behavior is not still completely clear, and future investigations based on both experimental data and theoretical calculations will be necessary for a better understanding of the origin of this optical property.

2.4 Conclusions

In summary, CaMoO_4 oriented aggregate crystals and meso- and nanocrystals were obtained with solvent ratios (water/ethylene glycol) and processed in a microwave-assisted hydrothermal/solvothermal system at 140 °C for 1 h. XRD patterns and FT-Raman spectra indicated that the CaMoO_4 meso- and nanocrystals are ordered at long- and short-range with the presence of a scheelite-type tetragonal structure without the presence of secondary phases. FT-IR spectra showed characteristic vibrational modes of a tetragonal crystal system. FEG-SEM micrographs indicated an anisotropic growth for CaMoO_4 oriented aggregate crystals processed under hydrothermal-microwave conditions and isotropic growth for CaMoO_4 meso- and nanocrystals processed under solvothermal-microwave conditions. Thus, the micrographs indicated that the solvent ratios are able to influence the crystal growth process, and also, the micrographs showed the agglomerate nature and polydisperse size distribution. TEM micrographs revealed that the presence of different solvent ratios (water/ethylene glycol) promotes the formation of CaMoO_4 oriented aggregate crystals and meso- and nanocrystals. HR-TEM micrographs evidenced that the CaMoO_4 oriented aggregate crystals are formed by aggregating of nanocrystals

in the same crystallographic plane, but not all those nanocrystals are oriented, while, in CaMoO_4 mesocrystals, all the nanocrystals are oriented, as seen by the SAED. HR-TEM micrographs evidenced that the CaMoO_4 nanocrystals present preferential growth along the [001] direction, but in general, these nanocrystals have different crystallographic orientations, as also seen by the SAED. A possible growth mechanism for the formation of CaMoO_4 oriented aggregate and meso- and nanocrystals prepared with different solvent ratios and a processed microwave-assisted hydrothermal/solvothermal system was explained in detail. UV–vis absorption spectra showed different optical band gap values, which were associated with the presence of intermediary energy levels within the band gap, which are basically composed of oxygen 2p orbitals (above the valence band) and molybdenum 4d orbitals (below the conduction band). The DFT investigations performed on the band structures suggested that the direct electronic transitions ($\Gamma - \Gamma$) occur in the band gap. The DOS analyses indicated that the valence band is mainly formed of oxygen $2p_x$, $2p_y$, $2p_z$ atomic orbitals, while the conduction band is composed mainly of molybdenum atoms containing $4d_{xy}$, $4d_{xz}$, $4d_{yz}$, $4d_{x^2-y^2}$, and $4d_{z^2}$ atomic orbitals. Also, the band structures and the DOS estimated by the theoretical calculations showed that the electronic states are influenced by the displacements performed on the Mo atoms (lattice formers) in the $[\text{MoO}_4]$ clusters, while little influence is noted by Ca atoms (lattice modifier) in the $[\text{CaO}_8]$ clusters due to $5s$, $5p_x$, $5p_y$, and $5p_z$ atomic orbitals presenting weak hybridization with the oxygen atomic orbitals. The PL emission maximum can be linked to crystal shape/intrinsic defects in the surface and mainly to possible distortions on the tetrahedron $[\text{MoO}_4]$ clusters in the lattice caused by the microwave irradiation. Moreover, the nonlinear PL behavior also can be related to formation of defects at medium range in the lattice caused by the magnetic field oscillator of the microwave irradiation by

coupling with solvents and/or the crystal lattice, that leads to obtention of (oriented aggregate crystals, meso and nanocrystals) with different crystallographic orientations.

Acknowledgment

The authors acknowledge the financial support of the Brazilian research financing institutions: FAPESP (No . 2009/50303-4), CNPq, and CAPES. Special thanks are extended to Prof. Dr. D. Keyson and Dr. D. P. Volanti for the development of the domestic microwave–hydrothermal system.

Supporting Information

Figures showing the viscosities of different solvent ratios ($\text{H}_2\text{O}/\text{C}_2\text{H}_6\text{O}_2$) employed in preparation of CaMoO_4 crystals; the specific surface area of CaMoO_4 aggregated oriented crystals and meso- and nanocrystals; N_2 adsorption–desorption isotherms of CaMoO_4 aggregated oriented crystals and meso- and nanocrystals; TEM/HR-TEM micrographs and SAED of CaMoO_4 oriented aggregate crystals and meso- and nanocrystals; a schematic representation of a CaMoO_4 oriented aggregate crystals and meso- and nanocrystals and possible relation of orientation of crystals with the photoluminescence properties; a diagram of the primitive body-centered-tetragonal Brillouin zone; the correlation of the experimental gap energy [$E_{\text{gap}(exp)}$] with the theoretical gap energy [$E_{\text{gap}(theo)}$] after the displacement of Mo atoms to deform the

CaMoO₄ crystal; and partial and total DOS for each one of the main atomic orbitals involved (Ca = 5s, 5p, Mo = 4d, and O = 2p) of crystalline CaMoO₄ with and without displacement of the Mo atoms. This material is available free of charge via the Internet at <http://pubs.acs.org>.

2.5 References

- [1] (a) Thongtem, T.; Phuruangrat, A.; Thongtem, S. *Mater. Lett.* **2008**, *62*, 454–457. (b) Sun, Y.; Ma, J.; Jiang, X.; Fang, J.; Song, Z.; Gao, X.; Liu, Z. *Solid State Sci.* **2010**, *12*, 1283–1286.
- [2] (a) Cui, C.; Bi, J.; Gao, D. *Appl. Surf. Sci.* **2008**, *255*, 3463–3465. (b) Gao, D.; Lai, X.; Cui, C.; Cheng, P.; Bi, J.; Lin, D. *Thin Solid Films* **2010**, *518*, 3151–3155.
- [3] Farabaugh, E. N.; Peiser, H. S.; Wachtman, J. B., Jr. *J. Res. Natl. Bur. Stand.* **1966**, *70A*, 379–384.
- [4] Zhang, Y.; Holzwarth, N. A. W.; Williams, R. T. *Phys. Rev. B* **1998**, *57*, 12738–12750.
- [5] Achary, S. N.; Patwe, S. J.; Mathews, M. D.; Tyagi, A. K. *J. Phys. Chem. Solids* **2006**, *67*, 774–781.
- [6] Cavalli, E.; Bovero, E.; Belletti, A. *J. Phys.: Condens. Matter* **2002**, *14*, 5221–5228.
- [7] Li, X.; Yang, Z.; Guan, L.; Guo, J.; Wang, Y.; Guo, Q. *J. Alloys Compd.* **2009**, *478*, 684–686.
- [8] Balakshy, V. I.; Asratyan, K. R.; Molchanov, V. Y. *J. Opt. A: Pure Appl. Opt.* **2001**, *3*, S87–S92.
- [9] Andrade, L. H. C.; Li, M.S.; Guyot, Y.; Brenier, A.; Boulon, G. *J. Phys.: Condens. Matter* **2006**, *18*, 7883–7892.
- [10] Kiss, Z. J.; Pressley, R. J. *Appl. Opt.* **1996**, *5*, 1474–1486.
- [11] Xie, A.; Yuan, X.; Hai, S.; Wang, J.; Wang, F.; Li, L. *J. Phys. D.: Appl. Phys.* **2009**, *42*, 105107–105113.
- [12] Bavykina, I.; Angloher, G.; Hauff, D.; Kiefer, M.; Petricca, F.; Pröbst, F. *Opt. Mater.* **2009**, *31*, 1382–1387.

- [13] Choi, G. K.; Kim, J. R.; Yoon, S. H.; Hong, K. S. *J. Eur. Ceram. Soc.* **2007**, 27, 3063–3067.
- [14] Choi, G. K.; Cho, S. Y.; An, J. S.; Hong, K. S. *J. Eur. Ceram. Soc.* **2006**, 26, 2011–2015.
- [15] Haque, M. M.; Lee, H. I.; Kim, D. K. *J. Alloys Compd.* **2009**, 481, 792–796.
- [16] Liang, Y.; Han, X.; Yi, Z.; Tang, W.; Zhou, L.; Sun, J.; Yang, S.; Zhou, Y. *J. Solid State Electrochem.* **2007**, 11, 1127–1131.
- [17] Belogurov, S.; Kornoukhov, V.; Annenkov, A.; Borisevich, A.; Fedorov, A.; Korzhik, M.; Ligoun, V.; Missevitch, O.; Kim, S. K.; Kim, S. C.; Kim, S. Y.; Kwak, J. W.; Lee, H. S.; Lee, J.; Myung, S. S.; Lee, M. J.; Kim, Y. D.; Lee, J. Y.; Lee, J. I.; Kim, H. J.; Kwon, Y. J.; Hwang, M. J.; Zhu, J. J. *IEEE Trans. Nucl. Sci.* **2005**, 52, 1131–1135.
- [18] Annenkov, A. N.; Buzanov, O. A.; Danevich, F. A.; Georgadze, A. Sh.; Kim, S. K.; Kim, H. J.; Kim, Y. D.; Kobychhev, V. V.; Kornoukhov, V. N.; Korzhik, M.; Lee, J. I.; Missevitch, O.; Mokina, V. M.; Nagorny, S. S.; Nikolaiko, A. S.; Poda, D. V.; Podviyanuk, R. B.; Sedlak, D. J.; Shkulkova, O. G.; So, J. H.; Solsky, I. M.; Tretyak, V. I.; Yurchenko, S. S. *Nucl. Instrum. Methods Phys. Res., Sect. A.* **2008**, 584, 334–345.
- [19] Woo, S. I.; Kim, J. S.; Jun, H. K. *J. Phys. Chem. B* **2004**, 108, 8941–8946.
- [20] Yan, S.; Zhang, J.; Zhang, X.; Lu, S.; Ren, X.; Nie, Z.; Wang, X. *J. Phys. Chem. C* **2007**, 111, 13256–13260.
- [21] Hou, Z.; Chai, R.; Zhang, M.; Zhang, C.; Chong, P.; Xu, Z.; Li, G.; Lin, J. *Langmuir* **2009**, 25, 12340–12348.
- [22] Yoon, J. W.; Ryu, J. H.; Shim, K. B. *Mater. Sci. Eng. B* **2006**, 127, 154–158.
- [23] Mikhailik, V. B.; Kraus, H.; Miller, G.; Mykhaylyk, M. S.; Wahl, D. *J.*

- Appl. Phys.* **2005**, 97, 083523–083530.
- [24] Mikhailik, V. B.; Kraus, H.; Itoh, M.; Iri, D.; Uchida, M. *J. Phys.: Condens. Matter* **2005**, 17, 7209–7218.
- [25] Ryu, J. H.; Yoon, J. W.; Lim, C. S.; Oh, W. C.; Shim, K. B. *J. Alloys Compd.* **2005**, 390, 245–249.
- [26] Marques, A. P. A.; Longo, V. M.; de Melo, D. M. A.; Pizani, P. S.; Leite, E. R.; Varela, J. A.; Longo, E. *J. Solid State Chem.* **2008**, 181, 1249–1257.
- [27] Campos, A. B.; Simões, A. Z.; Longo, E.; Varela, J. A.; Longo, V. M.; de Figueiredo, A. T.; De Vicente, F. S.; Hernandez, A. C. *Appl. Phys. Lett.* **2007**, 91, 051923–051925.
- [28] Komarneni, S.; Roy, R.; Li, Q. H. *Mater. Res. Bull.* **1992**, 27, 1393–1405.
- [29] Thongtem, T.; Phuruangrat, A.; Thongtem, S. *Curr. Appl. Phys.* **2008**, 8, 189–197.
- [30] Floriano, W. B.; Nascimento, M. A. C. *Braz. J. Phys.* **2004**, 34, 38–41.
- [31] Cavalcante, L. S.; Sczancoski, J. C.; Tranquilin, R. L.; Varela, J. A.; Longo, E.; Orlandi, M. O. *Particuology* **2009**, 7, 353–362.
- [32] Brunauer, S.; Emmett, P. H.; Teller, E. *J. Am. Chem. Soc.* **1938**, 309–319.
- [33] Becke, A. D. *J. Chem. Phys.* **1993**, 98, 5648–5652.
- [34] Lee, C.; Wang, W.; Parr, R. G. *Phys. Rev. B* **1988**, 37, 785–789.
- [35] Cora, F.; Alfredsson, M.; Mallia, G.; Middlemiss, D. S.; Mackrodt, W.; Dovesi, R.; Orlando, R. *Struct. Bonding (Berlin)*; Springer Verlag: Berlin, 2004; p 113.
- [36] <http://www.crystal.unito.it/BasisSets/Ptable.html>.
- [37] Dovesi, R.; Saunders, V. R.; Roetti, C.; Orlando, R.; Zicovich Wilson, C. M.; Pascale, F.; Civalleri, B.; Doll, K.; Harrison, N. M.; Bush, I. J.; Arco, P. D.; Llunell, M. *CRYSTAL06 User's Manual*; University of Torino: 2006.
- [38] Kokalj, A. *J. Mol. Graph.* **1999**, 17, 176–179.

- [39] Joint Committee on Powder Diffraction Standards 2001; Diffraction Data File No. 29-0351; International Centre for Diffraction Data (ICDD, formerly JCPDS): Newtown Square, PA.
- [40] Holland, T. J. B.; Redfern, S. A. T. *Mineral. Mag.* **1997**, 61, 65–77.
- [41] Gong, Q.; Qian, X.; Ma, X.; Zhu, Z. *Cryst. Growth Des.* **2006**, 6, 1821–1825.
- [42] Kim, J. G.; Choi, J. H.; Jeong, J. M.; Kim, Y. M.; Suh, I. H.; Kim, J. P.; Kim, Y. J. *Bull. Korean Chem. Soc.* **2007**, 28, 391–396.
- [43] Marques, A. P. A.; Leite, E. R.; Varela, J. A.; Longo, E. *Nanoscale Res. Lett.* **2008**, 3, 152–157.
- [44] Wang, J.; Jing, X.; Yan, C.; Lin, J.; Liao, F. *J. Electrochem. Soc.* **2005**, 152, G534–G536.
- [45] Sczancoski, J. C.; Bomio, M. D. R.; Cavalcante, L. S.; Joya, M. R.; Pizani, P. S.; Varela Longo, E.; Li, M. S.; Andrés, J. *J. Phys. Chem. C* **2009**, 113, 5812–5822.
- [46] Sczancoski, J. C.; Cavalcante, L. S.; Marana, N. L.; da Silva, R. O.; Tranquilin, R. L.; Joya, M. R.; Pizani, P. S.; Varela, J. A.; Sambrano, J. R.; Li, M. S.; Longo, E.; Andrés, J. *Curr. Appl. Phys.* **2010**, 10, 614–624.
- [47] <http://www.jcrystal.com/steffenweber/JAVA/JSV/jsv.html>.
- [48] http://dor.huji.ac.il/3d_finds.html.
- [49] Senyshyn, A.; Kraus, H.; Mikhailik, V. B.; Vasylechko, L.; Knapp, M. *Phys. Rev. B.* **2006**, 73, 014104–014113.
- [50] <http://polyhedra.org/poly/show/0/tetrahedron>.
- [51] http://polyhedra.org/poly/show/128/snub_disphenoid.
- [52] Porto, S. P. S.; Scott, J. F. *Phys. Rev.* **1967**, 157, 716–719.
- [53] Christofilos, D.; Kourouklis, G. A.; Ves, S. *J. Phys. Chem. Solids* **1995**, 56, 1122–1129.

- [54] Sarantopoulou, E.; Raptis, C.; Ves, S.; Christofilos, D.; AKourouklis, G. *J. Phys.: Condens. Matter* **2002**, 14, 8925–8938.
- [55] Scott, J. F. *J. Chem. Phys.* **1968**, 48, 874–876.
- [56] Basiev, T. T.; Sobol, A. A.; Voronko, Y. K.; Zverev, P. G. *Opt. Mater.* **2000**, 15, 205–216.
- [57] Basiev, T. T.; Sobol, A. A.; Zverev, P. G.; Ivleva, L. I.; Osiko, V. V.; Powell, R. C. *Opt. Mater.* **1999**, 11, 307–314.
- [58] Rousseau, D. L.; Bauman, R. P.; Porto, S. P. S. *J. Raman Spectrosc.* **1981**, 10, 253–290.
- [59] Barker, A. S., Jr. *Phys. Rev.* **1964**, 135, A742–A747.
- [60] Golubović, A.; Gajić, R.; Dohčević-Mitrović, Z.; Nikolić, S. *J. Alloys Compd.* **2006**, 415, 16–22.
- [61] Ling, Z. C.; Xia, H. R.; Ran, D. G.; Liu, F. Q.; Sun, S. Q.; Fan, J. D.; Zhang, H. J.; Wang, J. Y.; Yu, L. L. *Chem. Phys. Lett.* **2006**, 426, 85–90.
- [62] Zverev, P. G. *Phys. Status Solidi C* **2004**, 1, 3101–3105.
- [63] Sarantopoulou, E.; Raptis, C.; Ves, S.; Christofilos, D.; Kourouklis, G. A. *J. Phys.: Condens. Matter* **2002**, 14, 8925–8938.
- [64] Marques, A. P. A.; Motta, F. V.; Leite, E. R.; Pizani, P. S.; Varela, J. A.; Longo, E.; de Melo, D. M. A. *J. Appl. Phys.* **2008**, 104, 043505–043510.
- [65] Tarte, P.; Liegeois-Duyckaerts, M. *Spectrochim. Acta, Part A* **1972**, 28, 2029–2036.
- [66] Clark, G. M.; Doyle, W. P. *Spectrochim. Acta, Part A* **1966**, 22, 1441–1447.
- [67] Lei, F.; Yan, B. *J. Solid State Chem.* **2008**, 181, 855–862.
- [68] Li, G.; Wang, Z.; Quan, Z.; Li, C.; Lin, J. *Cryst. Growth Des.* **2007**, 7, 1797–1802.
- [69] Cavalcante, L. S.; Sczancoski, J. C.; Tranquilin, R. L.; Joaya, M. R.; Pizani, P. S.; Varela, J. A.; Longo, E. *J. Phys. Chem. Solids* **2008**, 69,

2674–2680.

[70] Penn, R. L.; Banfield, J. F. *Science* **1998**, 281, 969–971.

[71] Lu, W. G.; Fang, J. Y. *J. Phys. Chem. B* **2005**, 109, 19219–19222.

[72] Chen, D.; Tang, K.; Li, F.; Zheng, H. *Cryst. Growth Des.* **2006**, 6, 247–252.

[73] Zhou, L.; O'Brien, P. *Small* **2008**, 4, 1566–1574.

[74] Xu, C.; Zou, D.; Guo, H.; Jie, F.; Ying, T. *J. Lumin.* **2009**, 129, 474–477.

[75] Lee, J. S.; Choi, S. C. *J. Eur. Ceram. Soc.* **2005**, 25, 3307–3314.

[76] Komarneni, S.; Katsuki, H. *Pure Appl. Chem.* **2002**, 74, 1537–1543.

[77] Thongtem, T.; Phuruangrat, A.; Thongtem, S. *J. Nanopart. Res.* **2010**, 12, 2287–2294.

[78] Zhao, X.; Li, T. K.; Xi, Y. Y.; Ng, D. H. L.; Yu, J. *Cryst. Growth Des.* **2006**, 6, 2210–2213.

[79] Penn, R. L. *J. Phys. Chem. B* **2004**, 108, 12707–12712.

[80] Geng, X.; Liu, L.; Jiang, J.; Yu, S. H. *Cryst. Growth Des.* **2010**, 10, 3448–3453.

[81] Ye, F.; Peng, Y.; Chen, G. Y.; Deng, B.; Xu, A. W. *J. Phys. Chem. C* **2009**, 113, 10407–10415.

[82] Yu, J. G.; Zhao, X. F.; Liu, S. W.; Li, M.; Mann, S.; Ng, D. H. L. *Appl. Phys. A: Mater. Sci. Process.* **2007**, 87, 113–120.

[83] Emsley, J. *Chem. Soc. Rev.* **1980**, 9, 91–124.

[84] Omta, A. W.; Kropman, M. F.; Woutersen, S.; Bakker, H. J. *Science* **2003**, 301, 347–349 [85] Bushuev, Y. G. *Russian Chem. Bull.* **1997**, 46, 888–891.

[86] Rozhkova, A. G.; Butyrskaya, E. V.; Rozhkova, M. V.; Shaposhnik, V. A. *J. Struct. Chem.* **2007**, 48, 166–169.

[87] Zhang, J. B.; Zhang, P. Y.; Ma, K.; Han, F.; Chen, G. H.; Wei, X. H. *Sci. China, Ser. B: Chem.* **2008**, 51, 420–426.

-
- [88] Kao, M. J.; Tien, D. C.; Jwo, C. S.; Tsung, T. T. *J. Phys. Conf. Ser.* **2005**, 13, 442–445.
- [89] Zwirbla, W.; Sikorska, A.; Linde, B. B. J. *J. Mol. Struct.* **2005**, 743, 49–52.
- [90] Murugan, A. V.; Samuel, V.; Ravi, V. *Mater. Lett.* **2006**, 60, 479–480.
- [91] Phuruangrat, A.; Thongtem, T.; Thongtem, S. *J. Cryst. Growth* **2009**, 311, 4076–4081.
- [92] Wang, W.; Hu, Y.; Goebel, J.; Lu, Z.; Zhen, L.; Yin, Y. *J. Phys. Chem. C* **2009**, 113, 16414–16423.
- [93] Wood, D. L.; Tauc, J. *Phys. Rev. B* **1972**, 5, 3144–3151.
- [94] Lacomba-Perales, R.; Ruiz-Fuertes, J.; Errandonea, D.; Martínez-García, D.; Segura, A. *Eur. Phys. Lett.* **2008**, 83, 37002–37006.
- [95] Longo, V. M.; Orhan, E.; Cavalcante, L. S.; Porto, S. L.; Espinosa, J. W. M.; Varela, J. A.; Longo, E. *Chem. Phys.* **2007**, 334, 180–188.
- [96] Zakharko, Y.; Luchechko, A.; Syvorotka, I.; Stryganyuk, G.; Solskii, I. *Radiat. Meas.* **2010**, 45, 429–431.
- [97] Ryu, J. H.; Choi, B. G.; Yoon, J. W.; Shima, K. B.; Machi, K.; Hamada, K. *J. Lumin.* **2007**, 124, 67–70.
- [98] Longo, V. M.; de Figueiredo, A. T.; Campos, A. B.; Espinosa, J. W. M.; Hernandez, A. C.; Taft, C. A.; Sambrano, J. R.; Varela, J. A.; Longo, E. *J. Phys. Chem. A* **2008**, 112, 8920–8928.
- [99] Jackson, S. K.; Layland, R. C.; Loye, H. C. Z. *J. Alloys Compd.* **1999**, 291, 94–101.
- [100] Fujita, M.; Itoh, M.; Takagi, S.; Shimizu, T.; Fujita, N. *Phys. Status Solidi B* **2006**, 243, 1898–1907.
- [101] Blasse, G. *J. Solid State Chem.* **1975**, 13, 339–344.
- [102] Chandrasekhar, B. K.; White, W. B. *Mater. Res. Bull.* **1990**, 25,

1513–1518.

[103] Mikhailik, V. B.; Kraus, H.; Wahl, D.; Mykhaylyk, M. S. *Phys. Status Solidi B* **2005**, 242, R17–R19.

[104] Mikhailik, V. B.; Kraus, H.; Itoh, M.; Iri, D.; Uchida, M. *J. Phys.: Condens. Matter* **2005**, 17, 7209–7218.

[105] Liu, J.; Huang, X.; Li, Y.; Li, Z. *J. Mater. Chem.* **2007**, 17, 2754–2758.

[106] Lei, H.; Zhang, S.; Zhu, X.; Sun, Y.; Fu, Y. *Mater. Lett.* **2010**, 64, 344–346.

[107] Phuruangrat, A.; Thongtem, T.; Thongtem, S. *J. Alloys Compd.* **2009**, 481, 568–572.

[108] Rao, K. J.; Vaidhyanathan, B.; Ganguli, M.; Ramakrishnan, P. A. *Chem. Mater.* **1999**, 11, 882–895.

[109] Yin, Y.; Gao, Y.; Sun, Y.; Zhou, B.; Ma, L.; Wu, X.; Zhang, X. *Mater. Lett.* **2009**, 64, 602–604.

Chapter 3

Paper 2 - Very Intense Distinct Blue and Red Photoluminescence Emission in MgTiO₃ Thin Films Prepared by the Polymeric Precursor Method: An Experimental and Theoretical Approach

Elídia Aparecida Vetter Ferri [†], Tatiana Martelli Mazzo ^{*‡}, Valeria Moraes Longo[§], Eduardo Moraes [‡], Paulo Sérgio Pizani ^{||}, Máximo Siu Li [⊥], José Waldo Martínez Espinosa[#], José Arana Varela[§], and Elson Longo[§]

J. Phys. Chem. C, 2012, 116 (29), pp 15557–15567

[†] Departamento de Química, Universidade Tecnológica Federal do Paraná, 85503-390, Pato Branco, PR, Brazil

[‡] INCTMN, LIEC, Departamento de Química, Universidade Federal de São Carlos, P.O. Box 676, 13565-905, São Carlos, SP, Brazil

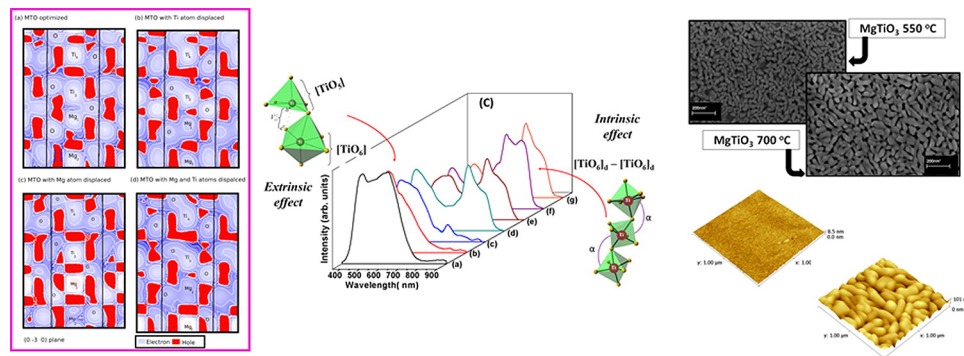
[§] INCTMN, LIEC, Instituto de Química, Universidade Estadual Paulista, P.O. Box 355, 14800-900, Araraquara, SP, Brazil

^{||} Departamento de Física, Universidade Federal de São Carlos, Laboratório de Semicondutores, P.O. Box 676, 13565-905, São Carlos, SP, Brazil

[⊥] Instituto de Física de São Carlos, USP, C. P. 369, 13569-970 São Carlos, São Paulo, Brazil

[#] Departamento de Engenharia de Produção, Universidade Federal de Goiás, 75704-020 Catalão, Goiás,

Brazil



Abstract

MgTiO₃ (MTO) thin films were prepared by the polymeric precursor method with posterior spin-coating deposition. The films were deposited on Pt(111)/Ti/SiO₂/Si(100) substrates and heat treated at 350 °C for 2 h and then heat treated at 400, 450, 500, 550, 600, 650 and 700 °C for 2 h. The degree of structural order–disorder, optical properties, and morphology of the MTO thin films were investigated by X-ray diffraction (XRD), micro-Raman spectroscopy (MR), ultraviolet–visible (UV–vis) absorption spectroscopy, photoluminescence (PL) measurements, and field-emission gun scanning electron microscopy (FEG-SEM) to investigate the morphology. XRD revealed that an increase in the annealing temperature resulted in a structural organization of MTO thin films. First-principles quantum mechanical calculations based on density functional theory (B3LYP level) were employed to study the electronic structure of ordered and disordered asymmetric models. The electronic properties were analyzed, and the relevance of the present theoretical and experimental results was discussed in the light of PL behavior. The presence of localized electronic levels and a charge gradient in the band gap due to a break in the symmetry are responsible for the PL in disordered MTO lattice.

3.1 Introduction

The increasing demand for light-emitting devices for displays, communication systems operating at microwave frequencies, electroluminescence, and the continuing miniaturization of circuitry systems has spurred the development of highly dielectric materials with active optical properties.

In particular, MgTiO_3 (MTO) is a ceramic oxide characterized by an ilmenite structure with space group $R\bar{3}$ and a rhombohedral crystal system.[1, 2] These materials have found a wide range of applications in electronic systems such as capacitors and mobile communication as well as radar and satellite broadcasting.[3, 4] Several methods have been used to obtain pure MTO, but the high sintering temperature of bulk materials is actually a major drawback that prohibits their use as dielectric resonators for miniaturized microwave circuits.[5] Thus, there is a continuous technological interest in using MTO crystals in the form of thin films with tailored properties and lower crystallization temperatures for easier integration into microelectronic devices.

The broad luminescent band usually observed at low temperatures in perovskite-type crystals is associated with the presence of imperfections or defects.[6] Leonelli and Brebner proposed a model to describe the luminescence process where electrons form small polarons that interact with holes to produce self-trapped excitons (STEs). The recombination of STEs results in a visible emission either immediately subsequent to or sometime after being trapped by impurities and defects.[7, 8] More recently, several phenomena of photoluminescence (PL) at low temperatures have been reported in the perovskite-type structure, and the effects observed have been ascribed to the recombination of electrons and hole polarons that form a charge transfer vibronic exciton.[9, 10]

Our group demonstrated that structurally disordered titanates (ATiO_3 where $A = \text{Mg, Ca, Sr, or Ba}$) synthesized by a soft chemical process (polymeric precursor method) showed intense PL at room temperature when excited by a 350.7 nm laser excitation line.[11, 12] We have reported several interesting properties of these ordered–disordered materials, including the fact that X-ray absorption near edge spectroscopy (XANES) results of the SrTiO_3 disordered powders[13] revealed the coexistence of two types of environments for titanium: a five-fold $[\text{TiO}_5]$ square-based pyramid and a six-fold coordination $[\text{TiO}_6]$ octahedron. The order was related to $[\text{TiO}_6]$ clusters whereas the disorder was related to $[\text{TiO}_5]$ clusters. Ab initio calculations showed that localized levels above the valence band (VB) and below the conduction band (CB) appear in theoretical disordered models and a charge transfer occurs from the $[\text{TiO}_5]$ cluster to the $[\text{TiO}_6]$ cluster. These additional levels explain the wide PL emission observed in disordered materials.[14, 15] Furthermore, this theory was expanded to understand the role of a modifier lattice,[16] and the interplay between the modifier and former lattice was refined with the concept of a complex cluster.[11, 12, 17] These distorted clusters produce a charge imbalance that encourages the trapping of holes in the aforementioned localized states. From a structural and electronic standpoint, the optical transition involved in PL measurements is due to a reorganization of electronic charges in distorted $[\text{TiO}_6]$ and $[\text{AO}_{12}]$ clusters in ATiO_3 -based materials. Distorted clusters yield a lattice distortion that is propagated throughout the material that shifts the surrounding clusters away from their ideal positions. Thus, distorted clusters must move for these properties to occur, which changes the electronic distribution throughout the network of these polar clusters. These movements can be induced within the crystal lattice by irradiation during the measurements, and this anisotropic cooperative movement leads to the PL property. Therefore, up to this point, the

wide band model[18] suggested by our group explains the favorable structural conditions that give rise to PL emission before the excitation process. Very recently, by first principle calculations, we have characterized normal vibrational modes associated with the breathing of TiO_6 octahedra of SrTiO_3 typical perovskite in the formation of a stable t^* (triplet) excited state as well as tetragonal distortions involved in the achievement of a stable s^* (singlet) excited state during the excitation process.[19, 20]

In earlier studies on MTO powders, we reported PL properties of this material. The PL emission was attributed to the structural order–disorder and/or distortions on the $[\text{TiO}_6]$ – $[\text{TiO}_6]$ complex clusters.[21] Most of the studies on MTO have been limited to the bulk crystal form; very few studies on MTO thin films have been reported.[22-25]

In this research, we investigated a synergistic study between experimental and theoretical results to synthesize and characterize MTO thin films prepared by the polymeric precursor method. For the experimental part, various complementary characterization techniques were used such as X-ray diffraction (XRD), micro-Raman (MR) spectroscopy, ultraviolet–visible (UV–vis) absorption spectroscopy, PL measurements, and field-emission gun scanning electron microscopy (FEG-SEM) to obtain a clearer picture of the physics underlying the luminescent behavior of ordered and disordered MTO thin films. For a theoretical approach to experimental PL results, three types of disorder were simulated in the crystalline (ordered) rhombohedra unit cell based on experimental XANES spectroscopy:[26] in the network former (Ti), in the network modifier (Mg), and in the network former–modifier (Ti/Mg). The purpose of these theoretical simulations was to demonstrate how different structural defects contribute to the disordered system and give rise to specific states in the forbidden gap that leads to different electronic transitions and

hence to different colored light emission.

3.2 Experimental Procedures

3.2.1 Synthesis of MTO Thin Films

The synthesis of MTO thin films was based on the polymeric precursor method.[27] Magnesium acetate $(\text{CH}_3\text{CO}_2)_2\text{Mg}$ (98%, Aldrich), titanium butoxide $\text{Ti}[\text{O}(\text{CH}_2)_3\text{CH}_3]_4$ (99%, Aldrich), ethylene glycol, $\text{C}_2\text{H}_6\text{O}_2$ (99.5%, Synth), and citric acid $\text{C}_6\text{H}_8\text{O}_7$ (99.5%, Synth) were used as raw materials. Titanium citrate was formed by dissolution of titanium butoxide in an aqueous solution of citric acid under constant stirring. The citrate solution was stirred at 90 °C to obtain a clear homogeneous solution. $(\text{CH}_3\text{CO}_2)_2\text{Mg}$ was added in a stoichiometric quantity to the Ti citrate solution. After the homogenization of Mg^{2+} cations, $\text{C}_2\text{H}_6\text{O}_2$ was added to promote a polyesterification reaction. The citric acid/ethylene glycol ratio was fixed at 60/40 in mass.

The polymeric resin obtained was placed in a viscosimeter Rheometer model Brookfield DV-III for the viscosity adjustment. After the adjustment of the viscosity to 12.9 mPa, the resin was deposited in the substrate of Pt(111)/Ti/SiO₂/Si(100) through the spin-coating system. The speed of rotation was fixed at 7000 rpm for 30 s. After deposition, each layer was dried at 150 °C for 10 min to remove residual solvents.

These films were heat treated initially at 350 °C for 2 h using a constant heating rate of 1 °C/min and then at 400, 450, 500, 550, 600, 650, and 700 °C in a furnace with a gradient control for 2 h.

3.2.2 Characterization Techniques

The MTO thin film crystalline phase was analyzed by XRD patterns recorded on a Rigaku-DMax2500PC with a Cu K α radiation in the 2θ range from 20° to 60°. MR measurements were performed using a T64000 spectrometer (Jobin–Yvon, France) triple monochromator coupled to a CCD detector. Spectra were obtained using a 514.5 nm wavelength of an argon ion laser; its maximum output power was maintained at 8 mW. UV–vis spectroscopy for spectra of the optical absorbance for MTO powders was taken using total diffuse reflectance mode Cary 5G equipment. A PL spectrum in the range from 350 to 1000 nm was taken with a Thermal Jarrel-Ash Monospec 27 monochromator and a Hamamatsu R446 photomultiplier. The 350.7 nm line of a krypton ion laser (Coherent Innova 90 K) was used as the excitation source, and the maximum output power was maintained at 200 mW. FEG-SEM micrographs (Supra 35-VP, Carl Zeiss, Germany) were employed to estimate the thickness of MTO films and the morphology. All measurements were taken at room temperature. The evaluation of surface morphology and roughness for MTO thin films was carried out by atomic force microscopy (AFM) using a Nanoscope III-A-Digital Instruments microscope.

3.3 Computational Details, Models, and Mechanisms

3.3.1 Packages, Functions, and Basis Sets

The calculations were performed with the CRYSTAL06[28] package within the framework of the density functional theory (DFT). The Becke's three-parameter hybrid nonlocal exchange functional[29] combined with the Lee–Yang–Parr gradient-corrected correlation functional, B3LYP,[30] was used. Hybrid density-functional methods have been extensively used for molecules that provides an accurate description of crystalline structures, bond lengths, binding energies, and band gap values.[31] The diagonalization of the Fock matrix was performed at adequate k-point grids (Pack–Monkhorst 1976) in the reciprocal space. The point group symmetry of the system was fully exploited to reduce the number of points to be considered. On each numerical step, the residual symmetry was preserved during the self-consistent field method (SCF) and the gradient calculation.

Atomic centers have been described by all-electron basis sets 8-511d1G for Mg,[32] 86-411(d31)G for Ti,[33] and 6-31d1 for O.[34] To simulate the displacement of the Mg and Ti atoms, we used the ATOMDISP option of CRYSTAL06. The XCRYSDEN program was used to design the band structure diagrams.[35]

3.3.2 MTO Structure and Periodic Model Details

The MTO structure crystallizes in a trigonal type structure with

rhombohedral axes with a space group $R\bar{3}$ with C_{3i}^2 symmetry at room temperature.[24, 25, 36] The magnesium atoms share the corners of the unit cell, and six oxygens surround the titanium atoms in a distorted octahedra. A unit cell was used as a periodic model to represent the crystalline ordered MTO (MTO-o), which contains 10 atoms in the unit cell. This MTO-o can be designated $[\text{TiO}_6]_o-[\text{TiO}_6]_o$ because each titanium atom is surrounded by six O and $[\text{MgO}_6]_o-[\text{MgO}_6]_o$ as six O surround the Mg atom (see Figure 3.1).

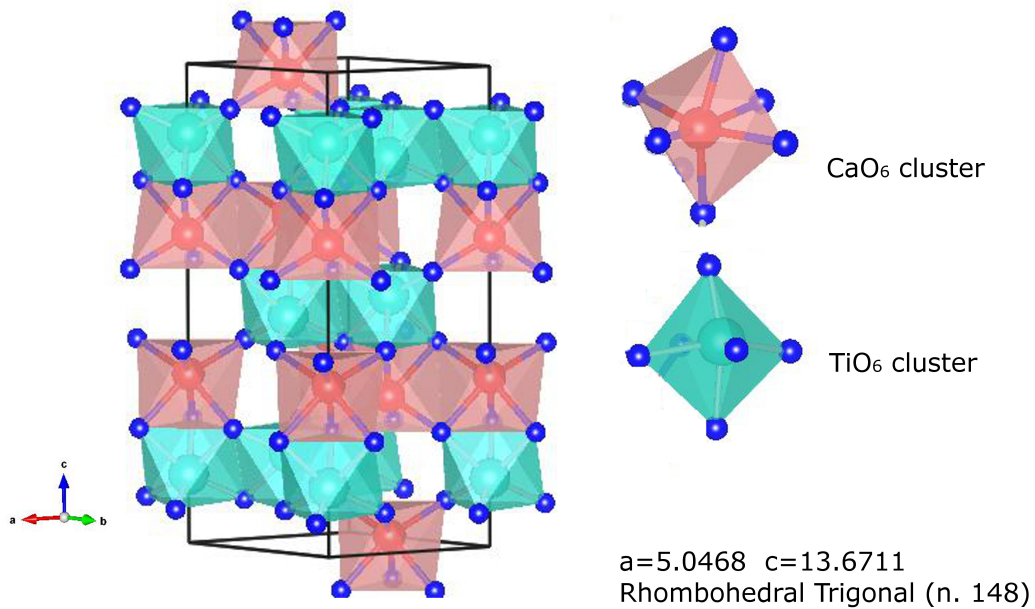


Figure 3.1: MTO-o model can be designated $[\text{TiO}_6]_o-[\text{TiO}_6]_o$ clusters because each titanium atom is surrounded by 6 O and $[\text{MgO}_6]_o-[\text{MgO}_6]_o$ cluster as 12 O surround the Mg atom.

Calculated values of the a and c parameters were 5.0468 and 13.8711 Å, respectively. The optimized value of the a and c parameters was used to calculate the disordered structures.

Three models (see Figure 3.1) were built to simulate the disordered type based on experimental XANES spectroscopy:[26](i) displacement of the network former, Ti (MTO-f); (ii) displacement of the network modifier, Mg (MTO-m); and (iii) simultaneous displacement of the network former–modifier, Ti/Mg (MTO-fm), by 0.5 Å.

In the MTO-f case, this displacement causes asymmetries in the octahedral, in which Ti is now surrounded by five oxygens in a square-based pyramid configuration, while the other Ti are surrounded by six oxygens, as in the case of MTO-o. This structure can be designated as $[\text{TiO}_6]-[\text{TiO}_5.V_O^Z]$, where $V_O^Z = V_O^X, V_O^\bullet, V_O^{\bullet\bullet}$, which gives rise to increasing disordered complex clusters (octahedral), depending on the displacement of the titanium.

The displacement of the network modifier disorder (MTO-m) causes asymmetries in the unit cell, where Mg is now surrounded by five oxygens $[\text{MgO}_5.V_O^X]$ while the others Mg are surrounded by six oxygens $[\text{MgO}_6]$, as in the case of MTO-o. Therefore, this asymmetric MTO-m model, represents the disorder in the network modifier material. This structure can be designated as $[\text{MgO}_6]-[\text{MgO}_5.V_O^Z]$, depending on the displacement of the magnesium.

Finally, the network former and modifier disorder (MTO-fm) was modeled at the same time by shifting both titanium and magnesium in the same way as described above. Therefore, in this asymmetric MTO model, MTO-fm represents the disorder in network former and modifier material. This structure can be designated as $[\text{TiO}_6]-[\text{TiO}_5.V_O^Z]$ and $[\text{MgO}_6]-[\text{MgO}_5.V_O^Z]$. With these models, the effects of different structural disorders can be separately evaluated in terms of the electronic structure.

It is important to notice that the cited displacement of atoms generates complex clusters that are representation of more distorted octahedral of former and modifier lattice. The purpose of this modeling was not to represent the exact reality of disordered structures, but to outline a simple scheme for a better understanding of the effects of structural deformation effects on the electronic structure without completely suppressing the geometry of the cell which is useful in periodic calculations.

3.4 Results and Discussion

3.4.1 X-ray Diffraction Patterns

Figure 3.2 presents XRD patterns of MTO thin films deposited on a Pt(111)/Ti/SiO₂/Si(100) substrate and heat treated at 400, 450, 500, 550, 600, 650, and 700 °C for 2 h.

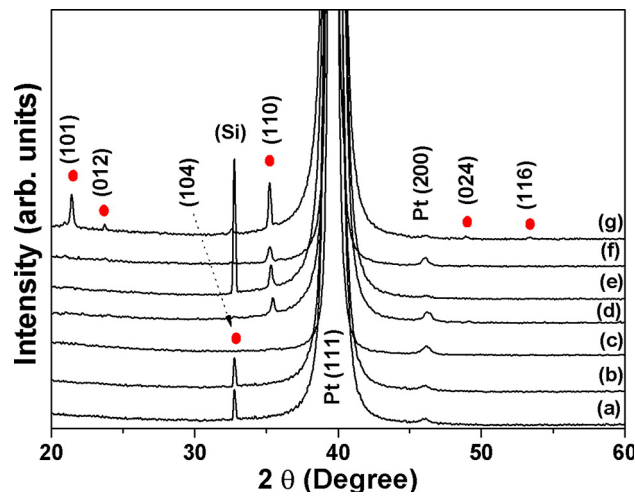


Figure 3.2: XRD patterns of MTO thin films on a Pt(111)/Ti/SiO₂/Si(100) substrate heat treated at (a) 400 °C; (b) 450 °C; (c) 500 °C; (d) 550 °C; (e) 600 °C; (f) 650 °C; and (g) 700 °C.

Figure 3.2 shows the increase in the heat treatment temperature that resulted in a structural organization of MTO thin films. Thin films heat treated at 550, 600, 650, and 700 °C exhibited a preferential orientation along the (110) direction on the substrate, which is in agreement with the results obtained by Choi et al.[25] The highest degree of crystallization was observed for the MTO thin film heat treated at 700 °C for 2 h. This film has a polycrystalline structure with respective crystallographic planes (101), (012), (104), (110), (024), and (116). In these crystalline films, all diffraction peaks can be indexed to the rhombohedral structure, which is in agreement with the respective Joint Committee on Powder Diffraction Standards (JCPDS) card no. 06-0494 and with

the diffraction peaks previously reported in the literature.[21, 22]

3.4.2 Micro-Raman Analysis

Figure 3.3 shows MR spectra of MTO thin films heat treated from 400 to 700 °C for 2 h under an air atmosphere. This figure illustrates that crystalline MTO thin films (600–700 °C) have all 10 Raman-active modes ($5A_g + 5E_g$) as predicted in the literature,[36-38] which characterizes an ordered structure at short range.

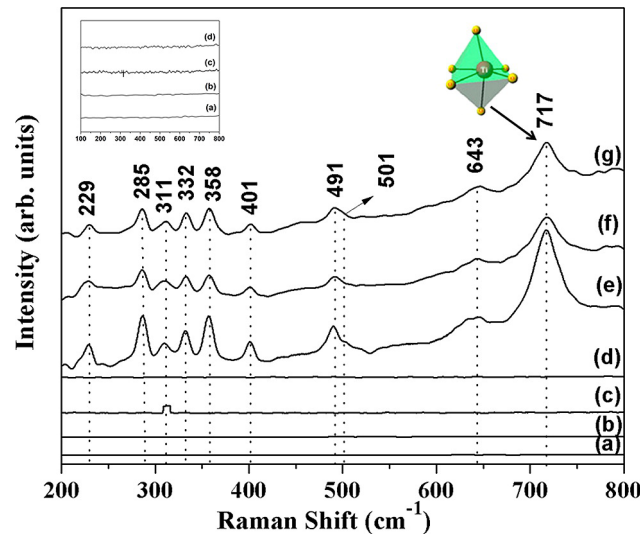


Figure 3.3: MR spectra of MTO thin films on a Pt(111)/Ti/SiO₂/Si(100) substrate heat treated at (a) 400 °C; (b) 450 °C; (c) 500 °C; (d) 550 °C; (e) 600 °C; (f) 650 °C; and (g) 700 °C. Insert: MR spectra of MTO thin films heat treated at (a) 400 °C; (b) 450 °C; (c) 500 °C; and (d) 550 °C.

Raman-active phonon modes for MTO thin films heat treated from 400 to 550 °C were not observed, which indicates structural order–disorder at short range (see the insert of Figure 3.3). A_g modes situated at 229 and 311 cm^{-1} emerge from vibrations of Mg and Ti atoms along the z axis. Other A_g modes observed at 401, 501, and 717 cm^{-1} are assigned to vibrations of O atoms. Particularly for modes at 501 and 717 cm^{-1} , the six O atoms exhibit breathing-like

vibrations, but each mode has a different vibration direction into the octahedral configuration. The intense E_g mode verified at 285 cm^{-1} is related to the antisymmetric breathing vibration of the O octahedron. E_g modes located at 332 and 358 cm^{-1} can be described as the twisting of the O octahedron with the vibrations of the Mg and Ti atoms parallel to the xy plane. E_g modes at 491 cm^{-1} are due to the antisymmetric breathing and twisting vibrations of the O octahedra with the cationic vibrations parallel to the xy plane. For the E_g mode at 491 cm^{-1} , both Mg and Ti atoms are involved in the vibration while the E_g mode at 643 cm^{-1} is associated with the Ti–O stretch.[36] In Table 3.1 are shown a comparative between the Raman modes obtained in this work with those reported in the literature.

Table 3.1: Data Obtained by MR Spectra Analyses of MTO Thin Films Heat Treated at Different Temperatures in Comparison with Other Studies Reported in the Literature

	MTO _{power,(22)} cm ⁻¹	MTO _{power,(38)} cm ⁻¹	this work, cm ⁻¹
A _g	229	225	229
E _g	285.8	281	285
A _g	310	306	311
E _g	330.9	328	332
E _g	356.5	353	358
A _g	400.2	398	401
E _g	488.9	486	491
A _g	501.2	500	501
E _g	643.9	641	643
A _g	716.4	715	717

3.4.3 Field-Emission Gun Scanning Electron Microscopy Analyses

Figure 3.4 shows FEG-SEM micrographs of the surface microstructure and cross section of MTO thin films annealed at different temperatures. The average thickness of MTO thin films ranges from 198 to 321 nm.

At 550 °C, nanoparticles of the cubic MTO initial crystal appear in accordance with the XRD pattern. An increase in the annealing temperature produces grain growth, reduces the total grain boundary area, and favors the junction between them. This behavior is typical of a coalescence process that results in the formation of necks (see inset in Figure 3.4c). For synthesizing a particle after the nucleation process, the subsequent growth of an individual structure occurs by two primary mechanisms: aggregation growth[39] and coarsening growth.[40] Crystal growth by aggregation can occur by a range of mechanisms, including interactions of randomly oriented particles (i.e., coalescence) or highly oriented particles (i.e., oriented attachment). Coalescence is defined as the aggregation between two nanoparticles of roughly equal sizes with no molecular exchange between them.[41]

The heat treatment in MTO thin films intensifies grain growth and contributes to the formation of pores (see inset in Figure 3.4d–g). Large grains are associated with the high crystallization rate of MTO thin films.

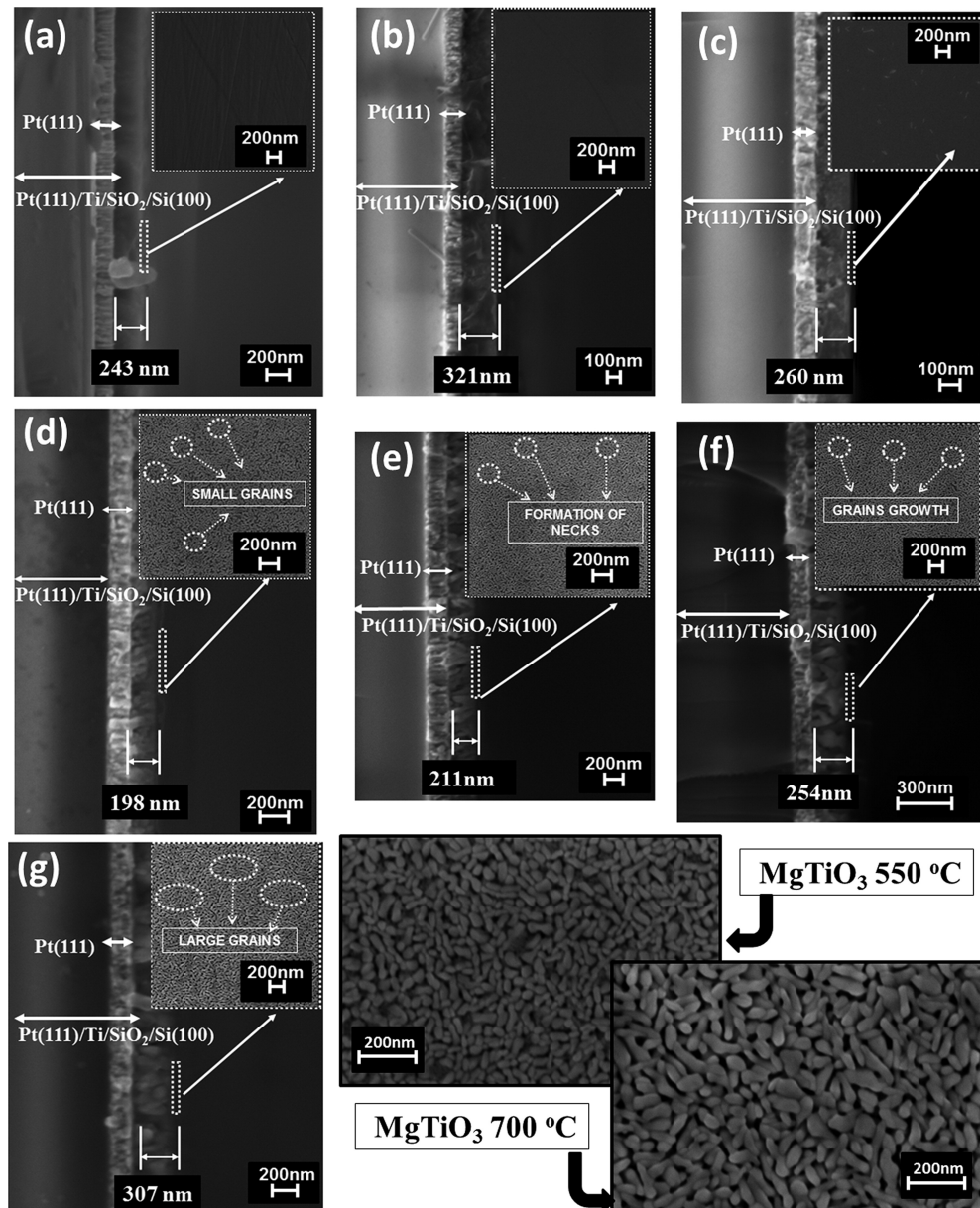


Figure 3.4: FEG-SEM micrographs of the surface microstructure and cross section of MTO thin films on a Pt(111)/Ti/SiO₂/Si(100) substrate heat treated at (a) 400 °C; (b) 450 °C; (c) 500 °C; (d) 550 °C; (e) 600 °C; (f) 650 °C; and (g) 700 °C.

3.4.4 Atomic Force Microscopy Analysis

The heat treatment temperature influence on morphologies of MTO thin films was also examined by atomic force microscopy (AFM) using tapping mode amplitude modulation. Figure 3.5 shows the surface morphologies of the deposited films deposited heat treat at 400, 550, and 700 °C.

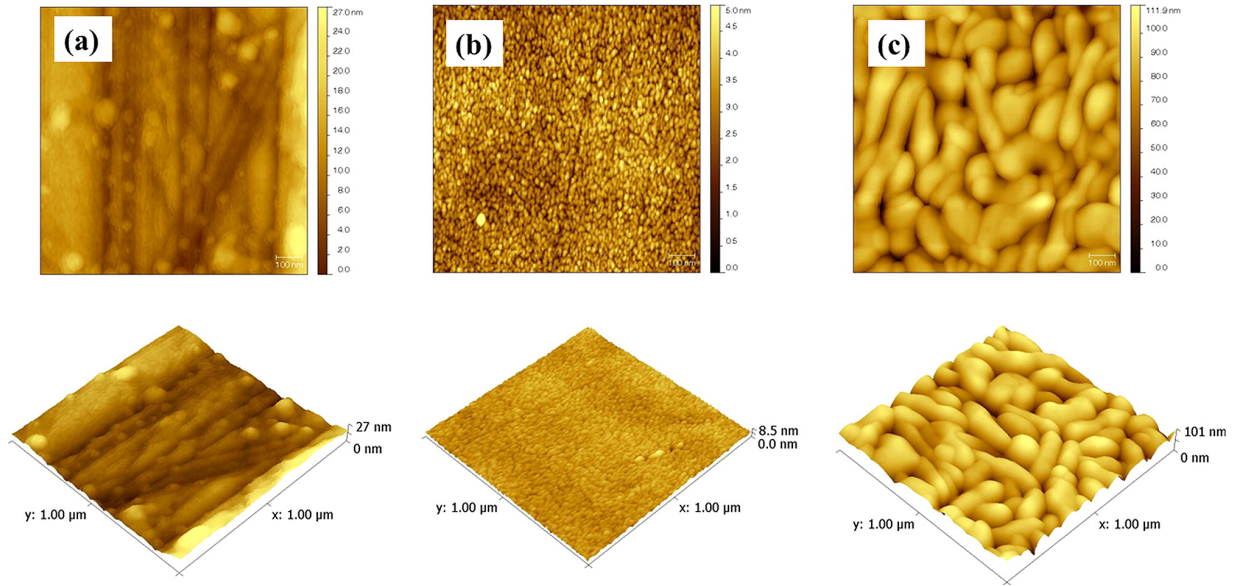


Figure 3.5: AFM micrographs of MTO thin films on a Pt(111)/Ti/SiO₂/Si(100) substrate heat treated at (a) 400 °C; (b) 550 °C; and (c) 700 °C.

The root-mean-square (rms) roughness varied from 4.23 to 13 nm as the heat treatment temperature increased from 400 to 700 °C. The MTO thin film heat treated at 400 °C is structurally disordered in the long and short range as revealed by the analysis of XRD and MR. AFM micrographs indicate that particles have an inhomogeneous growth with no granular structure (see Figure 3.5a). The MTO film surface morphology heat treated at 700 °C shows characteristic grains of an ordered (crystalline) material (see Figure 3.5c). An increase in the treatment temperature produces the appearance of small grains distributed homogeneously in the MTO thin film that are free of cracks. The structural order increase with annealing time temperature is confirmed by AFM analysis.

3.4.5 Ultraviolet–Visible Absorption Spectroscopy Analysis

The experimental optical band gap energy (E_{gap}) was estimated by the method proposed by Wood and Tauc.[42] The optical band gap value of

MTO thin films is associated with both absorbance and photon energy by equation 3.1 where a is the absorbance, h is Planck's constant, ν is the frequency, E_{gap} is the optical band gap, and n is a constant allied to the possible different types of electronic transitions, which can be described when $n = 2$ for direct allowed transitions. Figure 3.6a–g shows UV–vis absorbance spectra of MTO thin films heat treated at different temperatures for 2 h under an air atmosphere.

$$h\nu\alpha\infty(h\nu - E_{gap})^n \quad (3.1)$$

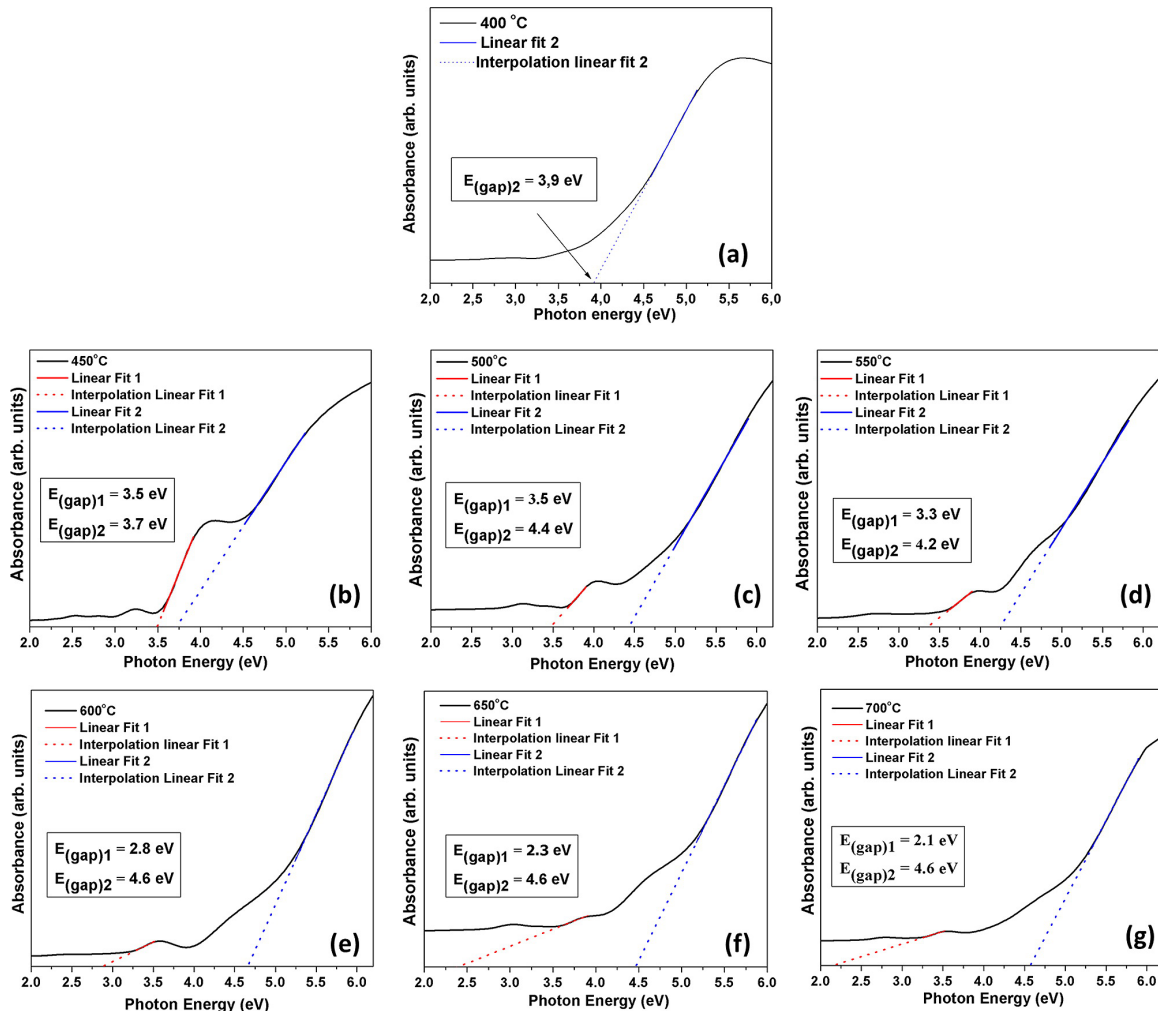


Figure 3.6: UV–vis optical absorption edge for (a) 400 °C; (b) 450 °C; (c) 500 °C; (d) 550 °C; (e) 600 °C; (f) 650 °C; and (g) 700 °C.

The results obtained for MTO thin films indicate two absorptions.

The E_{gap1} can be related to deep defects inserted in the band gap, and the E_{gap2}

can be related to shallow defects in the band gap. In the disorder-to-order evolution, with an increase in the annealing temperature, the E_{gap1} absorbance becomes smaller, and the E_{gap2} absorbance increases. The increase in E_{gap} values can be associated with a reduction of intermediary energy levels within the optical band gap. Reductions of these energy levels are attributed to the increase in the structural organization lattice with an increase in the heat treatment temperature. Therefore, a clear correlation between structural order–disorder and temperature can be assessed; with an increase in temperature, a more ordered and crystalline structure appears. These results agree with results obtained by XRD and MR where order at long and short range in thin films is obtained at temperatures higher than 550 °C.

The experimental band gap value obtained for the MTO powders reported by the literature was around 3.7 eV.[21, 43] The experimental optical band gap value of the MTO crystalline film thin measured in this study was 4.6 eV (E_{gap2}). The reminiscent weak absorption of 2.1 eV (E_{gap1}) can be attributed to distorted octahedra present in the MTO structure as intrinsic defects probably due to distorted tilted octahedra and will be better explained hereafter.

3.4.6 Energy Band Structure

To analyze the differences in the electronic structure, reference to quantities such as band structures are convenient because they can be compared to each other independent of the crystal space group. The calculated band structure also indicates contributions of electronic states in valence and conduction bands. Figure 3.7 shows the band structure of MTO-o, MTO-f, MTO-m, and MTO-fm models (see Figure 3.1) with 0.5 Å of dislocation and the respective

band gaps derived from these models.

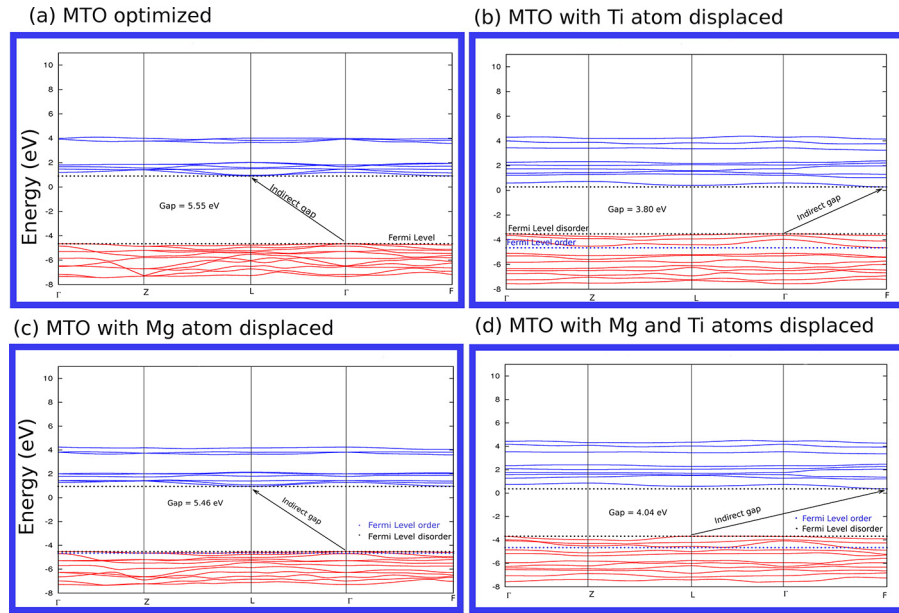


Figure 3.7: Calculated energy band structures for (a) MTO-o; (b) MTO-f; (c) MTO-m; and (d) MTO-fm.

The calculations indicate the modifications that the structural changes cause in the gap state. It should be emphasized that the displacements that generated the theoretical models represented in this work were based on previous XANES spectroscopic results[21] and do not reflect the exact reality of disordered thin films. However, they provide an interesting scheme by shedding light on the effects of structural deformation on the electronic structure.

Displacement in the network former causes increased disorder in the lattice when compared with the network modifier and simultaneous dislocation of the both network former and modifier. This disorder is characterized by band gap energy reduction in disordered models that leads to delocalized levels and a degeneracy lift of the valence band (VB) orbital and conduction band (CB) orbital (presented in the DOS analysis).

Figure 3.7a depicts the calculated band structure of bulk MTO-o. The top of the VB is at the Γ point. The bottom of the CB is at the L point. The minimal indirect gap between Γ and L is 5.55 eV, which is greater than the

experimental value of the crystalline thin film thin heat treated at 700 °C as deduced from the optical absorption edge that was found to be 4.6 eV. This result is an indication that the experimental structure has extrinsic distorted complex clusters, as observed in local measurements of MR or $[\text{TiO}_6]_o-[\text{TiO}_6]_o$ with a distorted angle between them (as observed in BaZrO_3 previous results).[44]

The calculated band structure of bulk MTO-f is depicted in Figure 3.7b. The top of the VB is at the Γ point, and the bottom of the CB is at the F point, which is different from the MTO-o model. The indirect minimal gap between Γ and F is 3.80 eV. This model represents only the electronic states derived from disorder in the former lattice and cannot be compared with an experimental film because disorder solely in the network former is impossible.

The calculated band structure of MTO-m is reported in Figure 3.7c. The top of the VB is at the Γ point, and the bottom of the CB is at the F point as in the MTO-o model. The indirect minimal theoretical gap is 5.46 eV, which is very close to the MTO-o model. This result means that the structural disorder of the modifier lattice has very little influence in the electronic structure of MTO that is consequently governed by the former lattice disorder. Finally, for the MTO-fm model, the calculated band gap was 4.04 eV from L in the VB to F in the CB. This result does not represent the major disorder of the lattice; that is, when the former and modifier lattices are dislocated simultaneously, the resulting electronic structure is more organized than the unique disorder in the former lattice. A possible explanation for this paradox is that there is an accommodation of the lattice when both the modifier and the former lattices are dislocated, which does not occur when the unique former lattice is dislocated.

The experimental optical absorption edge indicates two absorption regions that become more distinct with the evolution from disorder to order when the annealing temperature is increased. Compared with theoretical mod-

els, the deeper defects are related with a former network disorder linked to the $[\text{TiO}_5\text{V}_O^X]$ complex that is neutral in the lattice and represents a distorted octahedral and that remains even when the ordered MTO thin film is heat treated at 700 °C.

Indirect gaps along the K-points in the Brillouin zone are sensitive to structural changes in the MTO lattice, so a local disorder of former and/or modifier lattice in one region is a surface or interface, and order in another region as the bulk leads to different gaps in different regions of the Brillouin zone. These permanent differences are possible in MTO order–disorder structures and permit an electronic cross link between electrons and holes in the lattice in an intermediate range (distance between adjacent clusters). This fact can explain that there is more than an absorption region observed in the experimental optical absorption edge.

3.4.7 Density of States

The calculated total and atom-resolved density of states (DOS) projected for the models MTO-o, MTO-f, MTO-m, and MTO-fm are shown in Figure 3.8. They range from -8 eV below the top of the VB to 10 eV above and are the principal orbital that influences the gap state.

For the MTO-o (see Figure 3.8a), valence bands derive from $2p_x$, $2p_y$, and $2p_z$ orbitals of O atoms. They are separated by an indirect gap from the first CB that derives from transition metal titanium ($3d_{xy}$, $3d_{xz}$, $3d_{yz}$) atomic orbitals that are designated as “ t_{2g} ” in comparison with the $[\text{TiO}_6]_o$ regular cluster. Above these six bands are four Ti ($3d_{z^2-y^2}$ and $3d_{z^2}$) character bands designated as “ e_g ”. For the displaced models (MTO-f, MTO-m, and MTO-fm), although

the VB is globally constituted of O ($2p_x$, $2p_y$, $2p_z$) character states, the top is dislocated in relation to the MTO-o model that creates additional levels in the forbidden band gap. The CB is composed of 3d states of titanium in an apparently random splitting of bands (Figure 3.8b–d).

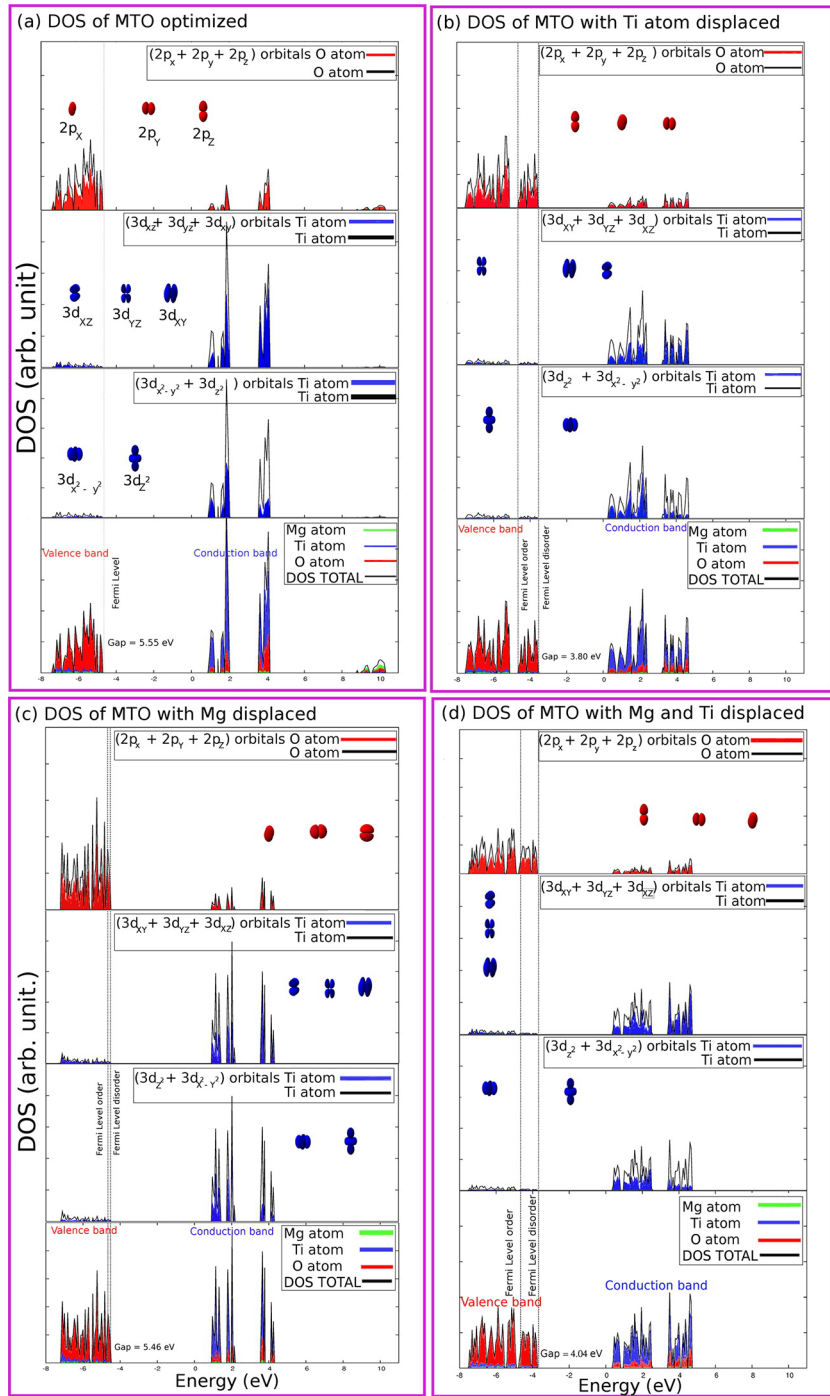


Figure 3.8: Total and atom-projected DOS for (a) MTO-o; (b) MTO-f; (c) MTO-m; and (d) MTO-fm models.

Mg ($3s$) states (not shown) are to be found in energies above -10

eV and are more dispersed in disordered models. These levels are weakly hybridized with oxygen levels in the MTO-f, MTO-m, and MTO-fm models.

3.4.8 Electron Density Map

As discussed previously, the theoretical models presented here are representations of broken bond. These defects produce an imbalanced density of charges in the network.

Figure 3.9 exhibits electron density maps for MTO-o, MTO-f, MTO-m, and MTO-fm models. The chosen plane was the (030), which contains the Mg, Ti, and O atoms. An analysis of Figure 3.9a clearly shows that the bonding between O–Ti–O has a covalent bonding nature that is visible due to hybridization between O (2p) states and the Ti (3d) states.

In the MTO-f model (see Figure 3.9b), the covalent bonding nature of O–Ti (dislocated) decreases as a consequence of a breaking Ti–O bond. The displacement of a metallic center when switching from MTO-o to MTO-f results in the deformation of a symmetric $[\text{TiO}_6\text{--TiO}_6]$ structure into two fragments: $[\text{TiO}_6]$ and $[\text{TiO}_5.V_O^Z]$ complex states where $z = V_O^X, V_O^\bullet, V_O^{\bullet\bullet}$, and the Kröger–Vink notation is used to designate complex clusters. The charge density is modulated by the metal dislocation value; that is, the distance between the dislocated metal and the oxygen, which loses their connection. Then, the $[\text{TiO}_5.V_O^X]$ species will be linked to the neutral or ordered complex and the $[\text{TiO}_5.V_O^\bullet]$ and $[\text{TiO}_5.V_O^{\bullet\bullet}]$ complexes are linked to an increased dislocation of metal and a more disordered structure, respectively.

Thus, the ionic bond nature of O–Mg–O is increased as observed in Figure 3.9c. With the deformation of a symmetric $[\text{MgO}_6\text{--MgO}_6]$ structure

by the dislocation of the Mg atom, the complexes $[\text{MgO}_5.V_O^X]$, $[\text{MgO}_5.V_O^\bullet]$ and $[\text{MgO}_5.V_O^{\bullet\bullet}]$ are formed.

The profile contours of Figure 3.9d for the MTO-fm model are a junction of MTO-f and MTO-m contours with polarization of specific regions in the lattice as a consequence of the simultaneous dislocation of Ti and Mg atoms. This structure generates greater imbalanced charges and the formation of static electrons and holes in the lattice.

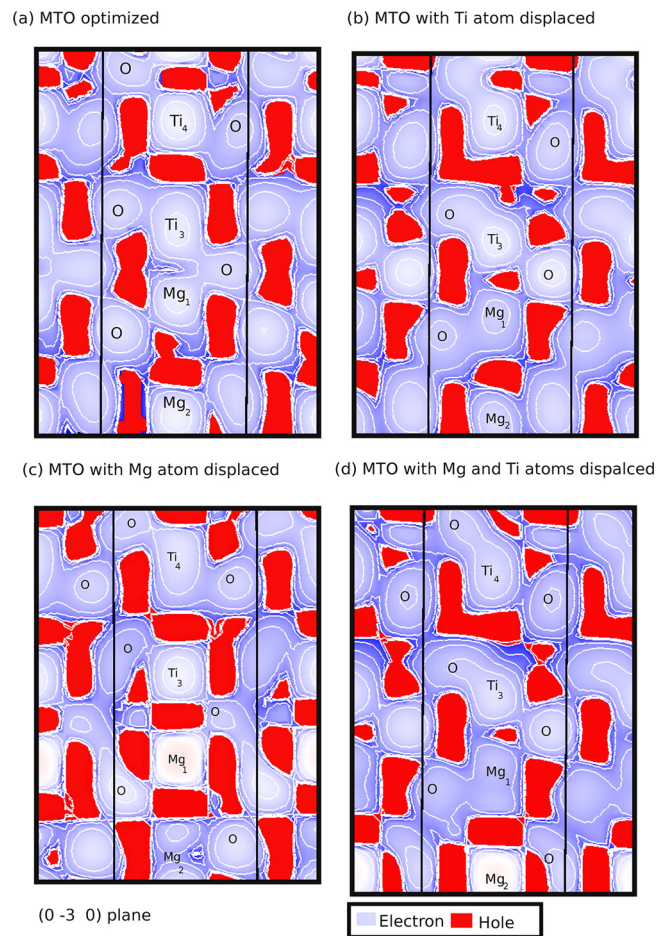


Figure 3.9: Electron density maps of (a) MTO-o; (b) MTO-f; (c) MTO-m; and (d) MTO-fm.

3.4.9 PL Emission at Room Temperature in MTO Thin Films

Figure 3.10 shows PL spectra of MTO thin films heat treated at different temperatures and excited with a 350.7 nm line of a krypton ion laser.

The profile of the PL emission is typical of a multiphoton process where the emission occurs by different methods and involves numerous states within the band gap.

It can be argued that two effects derived from extrinsic and intrinsic defects can govern the PL emission of the MTO thin films heat treated at different temperatures.

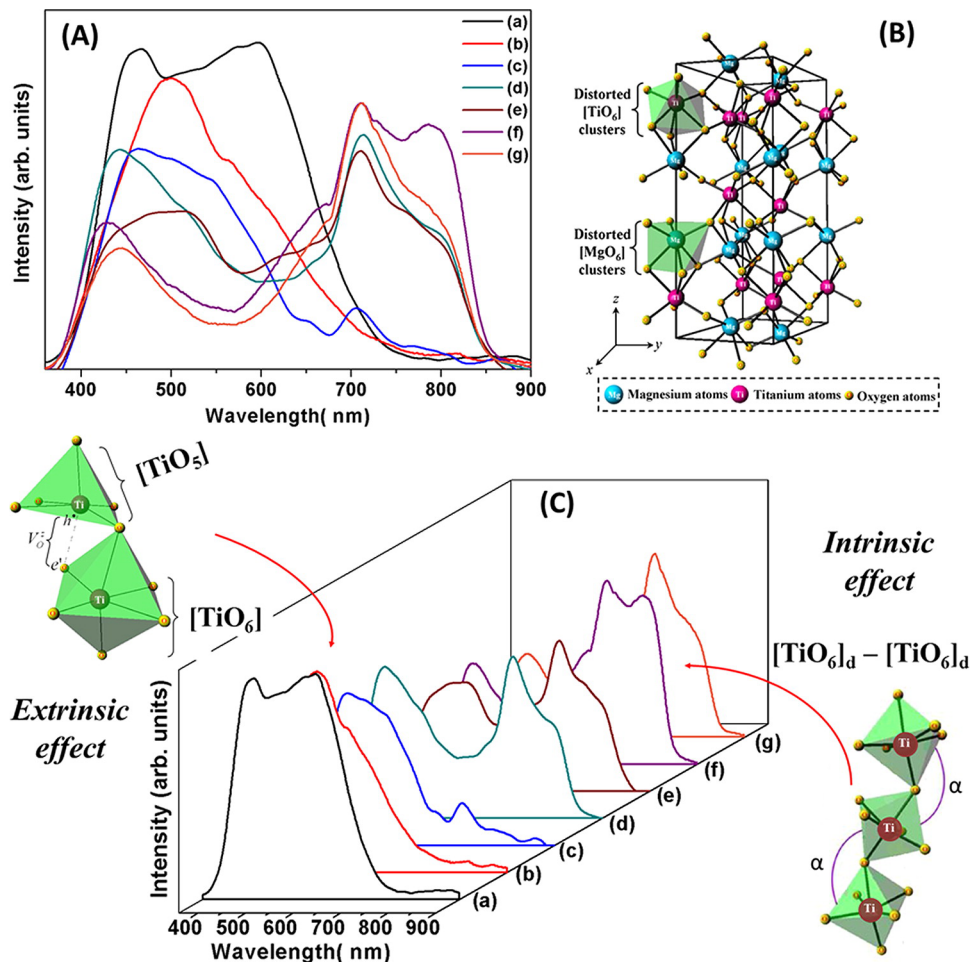
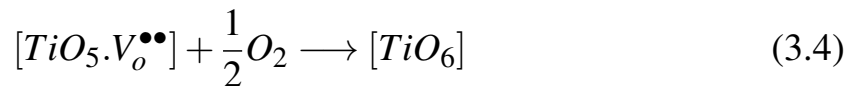
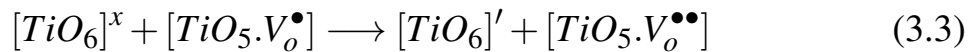
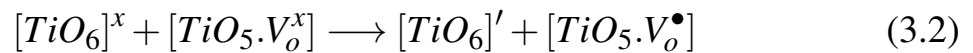


Figure 3.10: PL spectra of MTO thin films on a Pt(111)/Ti/SiO₂/Si(100) substrate heat treated at (a) 400 °C; (b) 450 °C; (c) 500 °C; (d) 550 °C; (e) 600 °C; (f) 650 °C; and (g) 700 °C; excited with a 350.7 nm line of a krypton ion laser. (A) Two-dimensional graphic of PL spectra; (B) schematic representation of a MgTiO₃ 1 × 1 × 1 unit cell rhombohedral structure; and (C) Three-dimensional graphic of PL spectra.

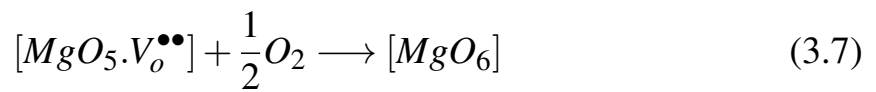
An intense broad greenish luminescence appears in thin films annealed from 400 to 500 °C with a maximum centered at 480 nm along with a weak infrared emission centered at 754 nm. The green emission is a more en-

energetic light and can be related to absorption in the gap_2 region, and the lesser energetic red emission can be related to the gap_1 absorption region (see Figure 3.6). We believe that two kinds of extrinsic defects are present in the disordered films, at long and short range, related to the former and modifier lattice disorder (complex clusters). As discussed previously, in the theoretical analysis, the disordered model shows an additional level above the VB and below the CB along with a permanent unbalanced charge density. During the excitation process, these electronic conditions give rise to trapping of electrons and holes. Several indirect band gaps permitted in the MTO structure during the excitation lead to a dynamic electron and hole crossing over different points of the Brillouin zone that results in two distinct emission PL regions.

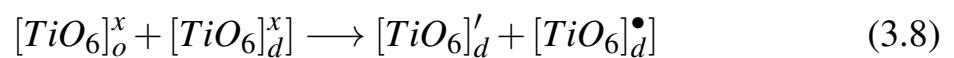
The extrinsic effect occurs by the dislocation of Mg or Ti in the MTO structure and results in complex cluster formations. For the former network (Ti)



Also, this model can be extended for the following network modifiers:



With the evolution of a crystallization process above 550 °C, there is a visible change in the PL emission with an intense emission at infrared spectra of light and a weaker emission in the visible green region. In this instance, shallow defects are eliminated, and reminiscent deeper defects remain. As discussed previously, experimental evidence exists that is dictated by MR results, and theoretical calculation evidence exists that this kind of defect comes from the former lattice. However, as demonstrated previously by XANES results,[21] at this point, the MTO structure has only very distorted or tilted $[TiO_6]_d$ clusters at the local range. These tilted clusters influence the intermediate range order as a distorted angle between $[TiO_6]_d$ - $[TiO_6]_d$ clusters and is the structural motif of MTO thin film intrinsic disorder (equation 3.8). This intermediate disorder (between two clusters) is replicated along the lattice and appears at long-range order as indicated by XRD results.



Therefore, it has become increasingly clear that structural complexity is essential for the appearance of the PL phenomenon. The key factor that

modulates the PL emission of these materials is the structural order–disorder within the lattice network; that is, the symmetry-breaking process that leads to nonideal (distorted) $[\text{TiO}_6]_d$ and $[\text{MgO}_6]_d$ clusters and the relationship between these clusters followed by networks of complex clusters and a specific charge distribution.

3.5 Conclusions

MgTiO_3 (MTO) thin films were successfully prepared by the polymeric precursor method with posterior spin-coating deposition. XRD patterns and MR spectra confirmed that films heat treated at $700\text{ }^\circ\text{C}$ crystallize in a rhombohedral structure. Also, XRD patterns and MR spectra show that films heat treated from 450 to $550\text{ }^\circ\text{C}$ have a structural order–disorder at long and short range. UV–vis absorption spectra revealed two absorptions: $E_{(gap)1}$ related to deep defects inserted in the band gap and $E_{(gap)2}$ related to shallow defects in the band gap. With an increase in the annealing temperature, the $E_{(gap)1}$ absorbance becomes smaller, and the $E_{(gap)2}$ absorbance increases. Band structure results indicate an indirect band gap for ordered and disordered models in different regions of the Brillouin zone and that a disorder in the former lattice is more remarkable than in the modifier lattice. Differences in the Brillouin zone in the MTO order–disorder structure permits an electronic cross link between electrons and holes in the lattice in an intermediate range (distance between adjacent clusters). This fact can explain more than an absorption region observed in the experimental optical absorption edge. Charge density maps show that, in disordered models, imbalanced charges and the formation of static electrons and holes in the lattice appear. These charges are linked with a complex

cluster of $[\text{TiO}_5.V_O^Z]$ and $[\text{MgO}_5.V_O^Z]$. PL phenomena of MTO thin film can be associated with extrinsic ($[\text{TiO}_5.V_O^Z]-[\text{TiO}_6]$ and $[\text{MgO}_5.V_O^Z]-[\text{MgO}_6]$) and intrinsic defects ($[\text{TiO}_6]_d-[\text{TiO}_6]_d$). With the evolution of the crystallization process above 550 °C, there is a visible change in the PL emission with an intense emission at infrared spectra of light and a weaker emission in the visible green region. Shallow defects are eliminated, and reminiscent deeper defects related to the former lattice remain. These two clear and distinct emissions can be controlled by the annealing temperature, and thus, MTO thin films are an extremely versatile materials that can be used in optical electronic devices.

The authors declare no competing financial interest.

Acknowledgment

The authors appreciate the support of the Brazilian research financing institutions CAPES, FAPESP/CEPID 98/14324-0, CNPq, and FAPESP. They also wish to thank Rorivaldo Camargo and Madalena Tursi for technical contributions.

3.6 References

This article references 44 other publications.

- [1] Okada, T.; Narita, T.; Nagai, T.; Yamanaka, T. *Am. Mineral.* **2008**, 93, 39–47.
- [2] Linton, J. A.; Fei, Y. W.; Navrotsky, A. *Am. Mineral.* **1999**, 84, 1595–1603.
- [3] Ferreira, V. M.; Baptista, J. L.; Petzelt, J.; Komandin, G. A.; Voitsekhovskii, V. V. *J. Mater. Res.* **1995**, 10, 2301–2305.
- [4] Belnou, F.; Bernard, J.; Houivet, D.; Haussonne, J. M. *J. Eur. Ceram. Soc.* **2005**, 25, 2785–2789.
- [5] Miao, Y. M.; Zhang, Q. L.; Yang, H.; Wane, H. P. *Mater. Sci. Eng., B* **2006**, 128, 103–106.
- [6] Zhang, W. F.; Yin, Z.; Zhang, M. S.; Du, Z. L.; Chen, W. C. *J. Phys.: Condens. Matter* **1999**, 11, 5655–5660.
- [7] Leonelli, R.; Brebner, J. L. *Solid State Commun.* **1985**, 54, 505–507.
- [8] Leonelli, R.; Brebner, J. L. *Phys. Rev. B* **1986**, 33, 8649–8656.
- [9] Eglitis, R. I.; Kotomin, E. A.; Borstel, G. *Eur. Phys. J. B* **2002**, 27, 483–486.
- [10] Eglitis, R. I.; Kotomin, E. A.; Borstel, G. *J. Phys.: Condens. Matter* **2002**, 14, 3735–3741.
- [11] Longo, V. M.; Cavalcante, L. S.; Costa, M. G. S.; Moreira, M. L.; de Figueiredo, A. T.; Andres, J.; Varela, J. A.; Longo, E. *Theor. Chem. Acc.* **2009**, 124, 385–394.
- [12] Moreira, M. L.; Andres, J.; Longo, V. M.; Li, M. S.; Varela, J. A.; Longo, E. *Chem. Phys. Lett.* **2009**, 473, 293–298.
- [13] Pontes, F. M.; Longo, E.; Leite, E. R.; Lee, E. J. H.; Varela, J. A.; Pizani, P. S.; Campos, C. E. M.; Lanciotti, F.; Mastelaro, V.; Pinheiro, C. D. *Mater. Chem. Phys.* **2003**, 77, 598–602.

-
- [14] Orhan, E.; Varela, J. A.; Zenatti, A.; Gurgel, M. F. C.; Pontes, F. M.; Leite, E. R.; Longo, E.; Pizani, P. S.; Beltran, A.; Andres, J. *Phys. Rev. B* **2005**, 71, 085113.
- [15] Longo, E.; Orhan, E.; Pontes, F. M.; Pinheiro, C. D.; Leite, E. R.; Varela, J. A.; Pizani, P. S.; Boschi, T. M.; Lanciotti, F.; Beltran, A.; Andres, J. *Phys. Rev. B* **2004**, 69, 125115.
- [16] de Lazaro, S.; Milanez, J.; de Figueiredo, A. T.; Longo, V. M.; Mastelaro, V. R.; De Vicente, F. S.; Hernandez, A. C.; Varela, J. A.; Longo, E. *Appl. Phys. Lett.* **2007**, 90, 111904.
- [17] Longo, V. M.; Costa, M. D. S.; Simoes, A. Z.; Rosa, I. L. V.; Santos, C. O. P.; Andres, J.; Longo, E.; Varela, J. A. *Phys. Chem. Chem. Phys.* **2010**, 12, 7566–7579.
- [18] Longo, V. M.; Cavalcante, L. S.; Erlo, R.; Mastelaro, V. R.; de Figueiredo, A. T.; Sambrano, J. R.; de Lazaro, S.; Freitas, A. Z.; Gomes, L.; Vieira, N. D.; Varela, J. A.; Longo, E. *Acta Mater.* **2008**, 56, 2191–2202.
- [19] Gracia, L.; Andres, J.; Longo, V. M.; Varela, J. A.; Longo, E. *Chem. Phys. Lett.* **2010**, 493, 141–146.
- [20] Gracia, L.; Longo, V. M.; Cavalcante, L. S.; Beltran, A.; Avansi, W.; Li, M. S.; Mastelaro, V. R.; Varela, J. A.; Longo, E.; Andres, J. *J. Appl. Phys.* **2011**, 110, 043501.
- [21] Ferri, E. A. V.; Sczancoski, J. C.; Cavalcante, L. S.; Paris, E. C.; Espinosa, J. W. M.; de Figueiredo, A. T.; Pizani, P. S.; Mastelaro, V. R.; Varela, J. A.; Longo, E. *Mater. Chem. Phys.* **2009**, 117, 192–198.
- [22] Carta, G.; Gerbasi, R.; Rossetto, G.; Zanella, P.; Natali, M.; Bolzan, M.; Saoncella, O. *Surf. Coat. Technol.* **2007**, 201, 9117–9119.
- [23] Chen, Y. B.; Huang, C. L. *Surf. Coat. Technol.* **2006**, 201, 654–659.
- [24] Chen, Y. B.; Huang, C. L. *J. Cryst. Growth* **2005**, 282, 482–489.

- [25] Choi, Y. H.; Lee, J. *Thin Solid Films* **2001**, 385, 43–47.
- [26] Longo, V. M.; de Figueiredo, A. T.; de Lazaro, S.; Gurgel, M. F.; Costa, M. G. S.; Paiva-Santos, C. O.; Varela, J. A.; Longo, E.; Mastelaro, V. R.; De Vicente, F. S.; Hernandez, A. C.; Franco, R. W. A. *J. Appl. Phys.* **2008**, 104, 023515.
- [27] Pechini, M. P. U.S. Patent 3330697, July 11, **1967**.
- [28] Dovesi, R.; Saunders, V. R.; Roetti, C.; Orlando, R.; Zicovich-Wilson, C. M.; Pascale, F.; Civalleri, B.; Doll, K.; Harrison, N. M.; Bush, I. J.; D'Arco, P.; Llunell, M. *CRYSTAL06*; University of Torino: Torino, Italy, **2006**.
- [29] Becke, A. D. *J. Chem. Phys.* **1993**, 98, 5648–5652.
- [30] Lee, C. T.; Yang, W. T.; Parr, R. G. *Phys. Rev. B* **1988**, 37, 785–789.
- [31] Hu, C.-H.; Chong, D. P. *Encyclopedia of Computational Chemistry*; von Ragué Schleyer, P., Ed.; Wiley: Chichester, U.K., **1998**.
- [32] Valenzano, L.; Noel, Y.; Orlando, R.; Zicovich-Wilson, C. M.; Ferrero, M.; Dovesi, R. *Theor. Chem. Acc.* **2007**, 117, 991–1000.
- [33] Cora, F. *Mol. Phys.* **2005**, 103, 2483–2496.
- [34] Corno, M.; Busco, C.; Civalleri, B.; Ugliengo, P. *Phys. Chem. Chem. Phys.* **2006**, 8, 2464–2472.
- [35] Kokalj, A. *J. Mol. Graph.* **1999**, 17, 176.
- [36] Wang, C.-H.; Jing, X. P.; Feng, W.; Lu, J. *J. Appl. Phys.* **2008**, 104, 034112.
- [37] Reynard, B.; Guyot, F. *Phys. Chem. Miner.* **1994**, 21, 441–450.
- [38] Hirata, T.; Ishioka, K.; Kitajima, M. *J. Solid State Chem.* **1996**, 124, 353–359.
- [39] Privman, V.; Goia, D. V.; Park, J.; Matijevic, E. *J. Colloid Interface Sci.* **1999**, 213, 36–45.
- [40] Norris, S. A.; Watson, S. J. *Acta Mater.* **2007**, 55, 6444–6452.

- [41] Jose-Yacaman, M.; Gutierrez-Wing, C.; Miki, M.; Yang, D. Q.; Piyakis, K. N.; Sacher, E. *J. Phys. Chem. B* **2005**, 109, 9703–9711.
- [42] Wood, D. L.; Tauc, J. *Phys. Rev. B* **1972**, 5, 3144.
- [43] Haart, L. G. J.; Vries, A. J.; Blasse, G. *Mater. Res. Bull.* **1984**, 19, 817.
- [44] Moreira, M. L.; Buzolin, P. G. C.; Longo, V. M.; Nicoleti, N. H.; Sambrano, J. R.; Li, M. S.; Varela, J. A.; Longo, E. *J. Phys. Chem. A* **2011**, 115, 4482–4490.

Chapter 4

Paper 3 - A combined theoretical and experimental study of electronic structure and optical properties of β -ZnMoO₄ microcrystals

L.S. Cavalcante^{a,b}, E. Moraes^c, M.A.P. Almeida^c, C.J. Dalmaschio^c, N.C.

Batista^b, J.A. Varela^a, E. Longo^a, M. Siu Li^d, J. Andrés^e, A. Beltrán^e

Polyhedron, Volume 54, 30 April 2013, Pages 13–25

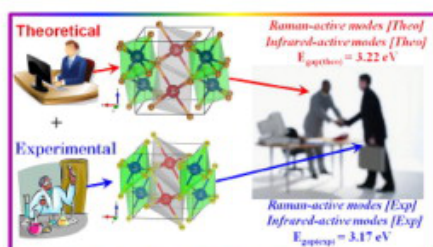
^a Universidade Estadual Paulista, P.O. Box 355, CEP 14801-907 Araraquara, SP, Brazil

^b UESPI-CCN, Departamento de Química, Rua João Cabral, P.O. Box 2231, 64002-150, Teresina-PI, Brazil

^c DQ-LIEC-Universidade Federal de São Carlos, P.O. Box 676, CEP 13565-905, São Carlos, SP, Brazil

^d IFSC-Universidade de São Paulo, P.O. Box 369, 13560-970, São Carlos, SP, Brazil

^e Department of Química-Física-Analítica, Universitat Juame I, 12071 Castello, Spain



Abstract

In this paper, a combined theoretical and experimental study on the electronic structure and photoluminescence (PL) properties of beta zinc molybdate (β -ZnMoO₄) microcrystals synthesized by the hydrothermal method has been employed. These crystals were structurally characterized by X-ray diffraction (XRD), Rietveld refinement, Fourier transform Raman (FT-Raman) and Fourier transform infrared (FT-IR) spectroscopies. Their optical properties were investigated by ultraviolet-visible (UV-vis) absorption spectroscopy and PL measurements. First-principles quantum mechanical calculations based on the density functional theory at the B3LYP calculation level have been carried out. XRD patterns, Rietveld refinement, FT-Raman and FT-IR spectra showed that these crystals have a wolframite-type monoclinic structure. The Raman and IR frequencies experimental results are in reasonable agreement with theoretically calculated results. UV-vis absorption measurements show an optical band gap value of 3.17 eV, while the calculated band structure has a value of 3.22 eV. The density of states indicate that the main orbitals involved in the electronic structure of β -ZnMoO₄ crystals are (O 2*p*-valence band and Mo 4*d*-conduction band). Finally, PL properties of β -ZnMoO₄ crystals are explained by distortions effects in octahedral [ZnO₆] and [MoO₆] clusters and inhomogeneous electronic distribution into the lattice with the electron density map.

4.1 Introduction

Zinc molybdate (ZnMoO₄) crystals are semiconductor inorganic solids that exhibit two types of structures α -alpha and β -beta which can be obtained depending on synthesis conditions and processing time/temperature [1-

3]. α -ZnMoO₄ crystals present a triclinic structure, space group $P\bar{1}$ and point group symmetry C_1 [4]. In the triclinic structure, zinc atoms are coordinated to six oxygens which form the distorted octahedral [ZnO₆] clusters while the molybdenum atoms are linked to four oxygens with its configuration of tetrahedral [MoO₄] clusters [5]. However, β -ZnMoO₄ crystals have a wolframite-type monoclinic structure, space group $P2/c$ and point group symmetry C_{2h}^4 [6]. In the monoclinic structure, the zinc and molybdenum atoms are surrounded by six oxygens which form the distorted octahedral [ZnO₆]/[MoO₆] clusters [6]. Both α - and β -ZnMoO₄ crystals in undoped and doped forms have been investigated because of their interesting electronic properties and high potential for possible industrial applications in various scientific fields such as: luminescence [7-9], red/green phosphors for light-emitting diodes [10-16], cryogenic/bolometric scintillating detectors [16-19], microwave dielectric [20], anticorrosive paints [21], cathode electrode in lithium batteries [22], photocatalyst for degradation of Victoria blue R and methyl orange dyes [23,24], and as a humidity sensor [25].

In the past years, ZnMoO₄ crystals with two types of α -triclinic and β -monoclinic structures were initially prepared by traditional methods such as: an oxide mixture or solid state reaction [26-30]. However, these preparation methods require high temperatures, long processing times and sophisticated equipment with high maintenance costs as well as the formation of deleterious phases. A possible alternative for the reduction of these problems and the production of these crystals at a low temperature can be the use of wet chemical methods such as coprecipitation controlled/calcination [31-32] and citrate complex precursors [33]. Recently, the hydrothermal (HT) method has attracted the attention of the scientific community in the preparation of different molybdates with several sizes, shapes and nanostructures [34-36]. In particular, this

synthesis method enables the attainment of pure molybdate at low temperatures (120°C – 160°C) in micro and nanoscale with excellent photoluminescence (PL) properties [37-41]. From a theoretical perspective, only one recent research [42] has been reported in the literature which shows band structure calculations and partial densities of states for the triclinic structure of α -ZnMoO₄ crystals using the full-potential linear-augmented-plane-wave method.

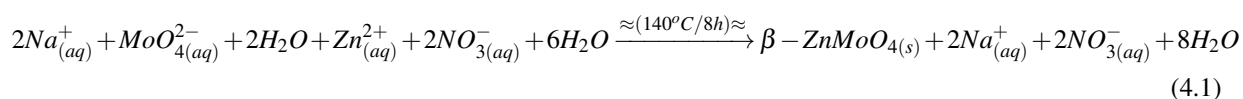
Therefore, in this work, we report the synthesis of β -ZnMoO₄ microcrystals by means of the HT method. These microcrystals were analyzed by X-ray diffraction (XRD), Fourier transform (FT-Raman), FT-Infrared (IR), ultraviolet-visible (UV-Vis) absorption spectroscopy and PL measurements. PL spectroscopy is an indispensable tool to elucidate electronic structure changes and physical phenomena involved in optical properties. In addition, we present first-principles quantum mechanical calculations based on the density functional theory (DFT) was employed to find a correlation between experimental results of Raman/IR spectroscopies and the Raman/IR-active frequencies theoretical, band gap and PL properties of β -ZnMoO₄ microcrystals with a monoclinic structure.

4.2 Experimental details

4.2.1 Synthesis of β -ZnMoO₄ microcrystals

β -ZnMoO₄ microcrystals were prepared by the HT method at 140°C for 8 h. The typical synthesis procedure for these microcrystals is described as follows: 2.5 mmol or 0.6079 g of molybdate (VI) sodium dihydrate [Na₂MoO₄·2H₂O] (99.5% purity, Sigma-Aldrich) and 2.5 mmol or

0.7512 g of zinc (II) nitrate hexahydrate [$\text{Zn}(\text{NO}_3)_2 \cdot 6\text{H}_2\text{O}$] (99% purity, Sigma-Aldrich) were dissolved separately in two plastic vessels (Falcon) with a capacity of 50 mL of deionized water. After dissolution of these salts at room temperature. Then the first solution (50 mL) with (Na^+ and MoO_4^{2-} ions) and the second solution (50 mL) with the (Zn^{2+} and NO_3^- ions) were mixed and transferred into a stainless-steel autoclave. This system was kept under constant agitation during the total time on the synthesis HT. The HT processing promotes favorable conditions for chemical reactions between the Zn^{2+} and MoO_4^{2-} ions which results in the formation of crystalline $\beta\text{-ZnMoO}_4$ microcrystals as shown in equation 4.1 below:



Then the stainless-steel autoclave was cooled to room temperature. The resulting suspensions were washed several times with deionized water to remove residual Na^+ ions. Finally, crystalline $\beta\text{-ZnMoO}_4$ precipitated powders of a light-gray color were collected and dried on a hot plate at 70°C for 8 h.

4.2.2 Characterizations $\beta\text{-ZnMoO}_4$ microcrystals

These $\beta\text{-ZnMoO}_4$ microcrystals were structurally characterized by X-ray diffraction (XRD) patterns using a D/Max-2500PC diffractometer Rigaku (Japan) with Cu-K α radiation ($\lambda = 1.5406 \text{ \AA}$) in the 2θ range from 10° to 73° in normal routine with a scanning velocity of $2^\circ/\text{min}$ and from 10° to 75° with a scanning velocity of $1^\circ/\text{min}$ in the Rietveld routine. FT-Raman spectroscopy was recorded with a Bruker-RFS 100 (Germany). The Raman spectrum from 50 to $1,000 \text{ cm}^{-1}$ was obtained using a 1,064 nm line with a Nd:YAG laser kept at its maximum output power at 100 mW and counts of 500 scans. FT-IR

spectroscopy was performed in a Bomem-Michelson spectrophotometer in the transmittance mode (model MB-102). The FT-IR spectrum in the range from 200 to 1,050 cm^{-1} was obtained using KBr pellets as a reference. The shapes of these $\beta\text{-ZnMoO}_4$ microcrystals were observed with a field emission scanning electron microscopy model Inspect F50 (FEI Company, Hillsboro, USA) operated at 15 kV. UV-vis spectra were taken using a Varian spectrophotometer (Model Cary 5G, USA) in a diffuse reflectance mode. PL measurements were performed through a Monospec 27 monochromator (Thermal Jarrel Ash, USA) coupled to a R446 photomultiplier (Hamamatsu Photonics, Japan). A krypton ion laser (Coherent Innova 90K, USA) ($\lambda = 350$ nm) was used as the excitation source; its maximum output power was maintained at 500 mW. The laser beam was passed through an optical chopper, and its maximum power on the sample was maintained at 40 mW. PL measurements were performed at room temperature.

4.2.3 Computational Method and Periodic Model of $\beta\text{-ZnMoO}_4$ microcrystals

All the calculations were carried out with the CRYSTAL09 computer program [43] within the framework of the density functional theory with the hybrid functional B3LYP [44-45]. The calculations were performed using a periodically repeating geometry; the method is described in the CRYSTAL09 manual [43]. Zn, Mo, and O atoms centers are described in basis sets: 86-411d31G, PS-311(d31)G and 8-411G, respectively, taken from the Crystal web site [46] where PS stands for Hay & Wadt's nonrelativistic small core pseudopotential [47]. The diagonalization of the Fock matrix was performed at ad-

equate k -point grids in the reciprocal space which is the Pack-Monkhorst/Gilat shrinking factor $IS = ISP = 4$. The thresholds controlling the accuracy of the calculation of Coulomb and exchange integrals were set to 10^{-8} (ITOL1 to ITOL4) and 10^{-14} (ITOL5) which assures a convergence in total energy better than 10^{-7} a.u. whereas the percentage of Fock/Kohn-Sham matrix mixing was set to 40 (IPMIX = 40) [47]. Full optimization of the (a , b , c) lattice parameters as well as the (x , y , z) internal coordinates has been carried out. The XCrySDen program version 1.5.23 [48] has been used to draw the band structure diagram, density of states (DOS) and the maps of the electronic density. The Raman/IR vibrational modes and their corresponding frequencies were calculated using numerical second derivatives of the total energies as implemented in the CRYSTAL09 package [43].

4.3 Results and discussion

4.3.1 X-ray diffraction and Rietveld refinement analyses of β -ZnMoO₄ crystals

Figures 1(a–c) show the experimental XRD patterns and Rietveld refinement plot of β -ZnMoO₄ microcrystals synthesized at 140°C for 8 h by the HT method and theoretical XRD profile with their specific lines position of optimized monoclinic structure, respectively.

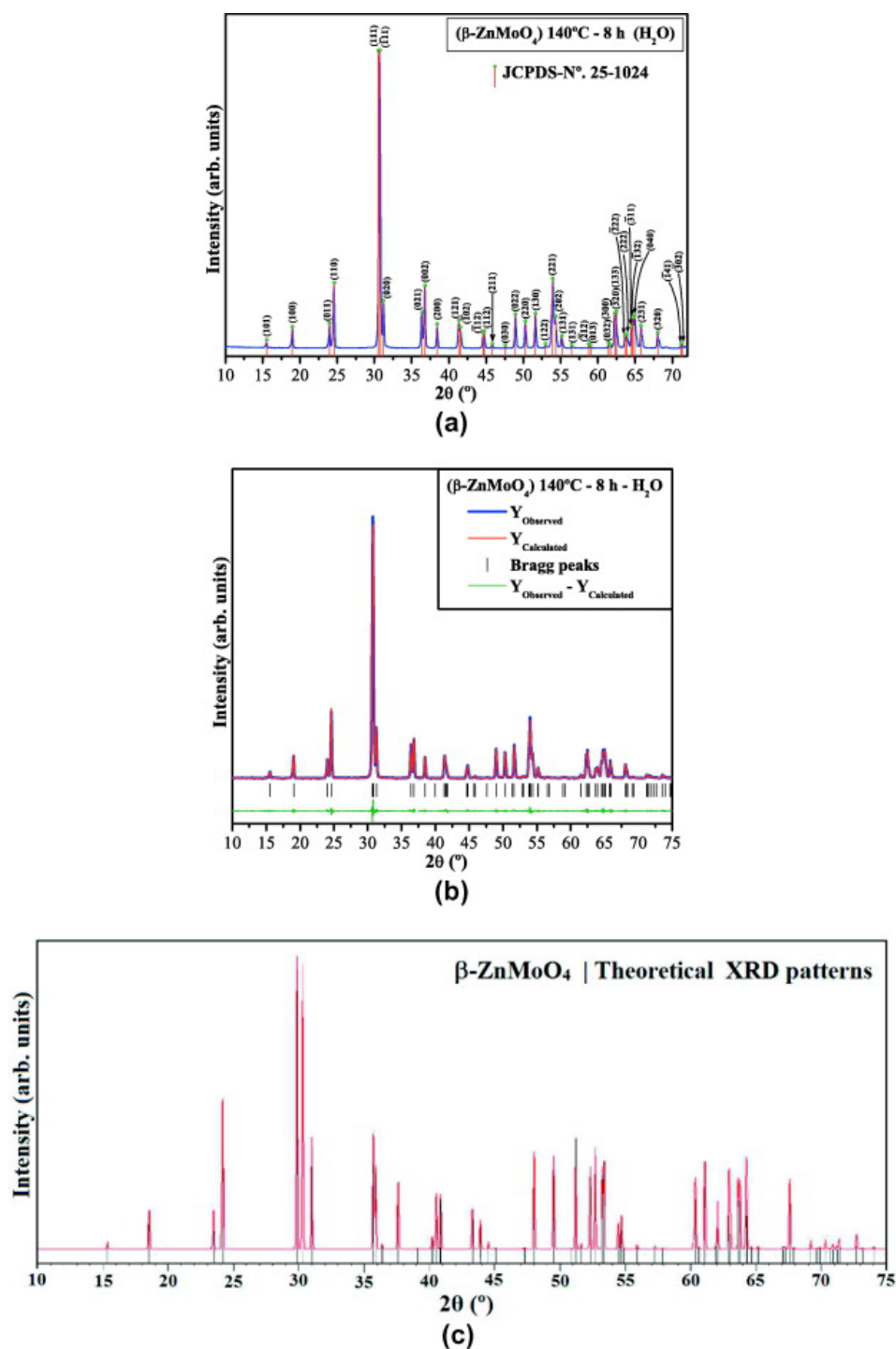


Figure 4.1: (a) XRD patterns, (b) Rietveld refinement plot of β -ZnMoO₄ microcrystals synthesized at 140°C for 8 h in HT system and (c) XRD patterns theoretically calculated, respectively.

According to the XRD patterns analysis illustrated in Figure 4.1(a), all XRD peaks can be indexed perfectly to a wolframite-type monoclinic structure with the space group $P2/c$ and point group symmetry C_{2h}^4 . Moreover, XRD patterns are in agreement with the respective Joint Committee on Powder

Diffraction Standards (JCPDS) card N^o. 25-1024 [49] and theoretical results. The profile of the all XRD peaks are narrower, that indicate the presence of large crystals with a considerable degree of structural order at long-range. The experimental lattice parameters, unit cell volume and atomic positions of β -ZnMoO₄ microcrystals were calculated using the Rietveld refinement method [50] with the Maud program (version 2.33) [51-52] (Figure 4.1(b)). The experimental results obtained from Rietveld refinement were optimized by theoretical calculations. The theoretical lattice parameters and atomic positions were used to model theoretical XRD profile with their specific lines position (Figure 4.1(c)). The experimentally obtained data from Rietveld refinement and theoretical calculations, respectively, are shown in Table 4.1.

Table 4.1: Lattice parameters, unit cell volume, atomic coordinate obtained experimentally from the structural refinement by the Rietveld method and theoretically calculated from DFT method.

(a) Atoms ^a	Wyckoff	Site	S.O.F.	x	y	z
Zn	2 <i>f</i>	2	1	0.5	0.68588	0.25
Mo	2 <i>e</i>	2	1	0	0.19564	0.25
O1	4 <i>g</i>	1	1	0.23115	0.35436	0.31255
O2	4 <i>g</i>	1	1	0.21435	0.93315	0.32451
(b) Atoms ^b						
Zn	2 <i>f</i>	2	1	0.5	0.67568	0.25
Mo	2 <i>e</i>	2	1	0	0.18603	0.25
O1	4 <i>g</i>	1	1	0.26110	0.38081	0.39073
O2	4 <i>g</i>	1	1	0.21320	0.89251	0.42669

^a β -ZnMoO₄ microcrystals synthesized at 140 °C for 8 h by HT method. a = 4.6987(3) Å; b = 5.7487(2) Å; c = 4.9044(2) Å; V = 132.47 Å³; β = 90.3312°; R_w = 6.54%; R_wnb = 5.67%; R_b = 4.23%; R_{exp} = 3.23% and s = 2.02.

^b Theoretical results. a = 4.7391 Å; b = 5.8100 Å; c = 5.0895 Å; V = 140.12 Å³.

S.O.F., site occupancy factor.

In this table, it was verified that the lattice parameters and unit cell volumes of a monoclinic structure are very close to the values recently published in the literature [3]. Small variations between these values can be related

to the peculiarity of each synthesis method where the experimental variables (temperature, time processing, heating rate, solvents, etc.) are able to influence the organization of the octahedral $[\text{ZnO}_6]$ and $[\text{MoO}_6]$ clusters within the monoclinic structure. Also, these variables cause the formation or reduction of structural defects (oxygen vacancies, distortion on the bonds, stresses and strains on the crystalline lattice). Moreover, in this table, the fit parameters (R_{wnb} , R_b , R_{exp} , R_w , and σ) suggest that the refinement results are quite reliable. It is interesting to note that there are considerable variations in the atomic positions related to the oxygen atoms while zinc and molybdenum atoms practically keep their positions fixed within the structure. These results indicate the existence of distortions on the octahedral $[\text{ZnO}_6]$ and $[\text{MoO}_6]$ clusters presents in electronic structure of β - ZnMoO_4 microcrystals.

4.3.2 Unit cell representations of β - ZnMoO_4 crystals

Figures 4.2(a,c,e) illustrate the representations of experimental β - ZnMoO_4 unit cells and Figures 4.2(b,d,f) shows the representations of theoretical β - ZnMoO_4 unit cells in same perspective, respectively.

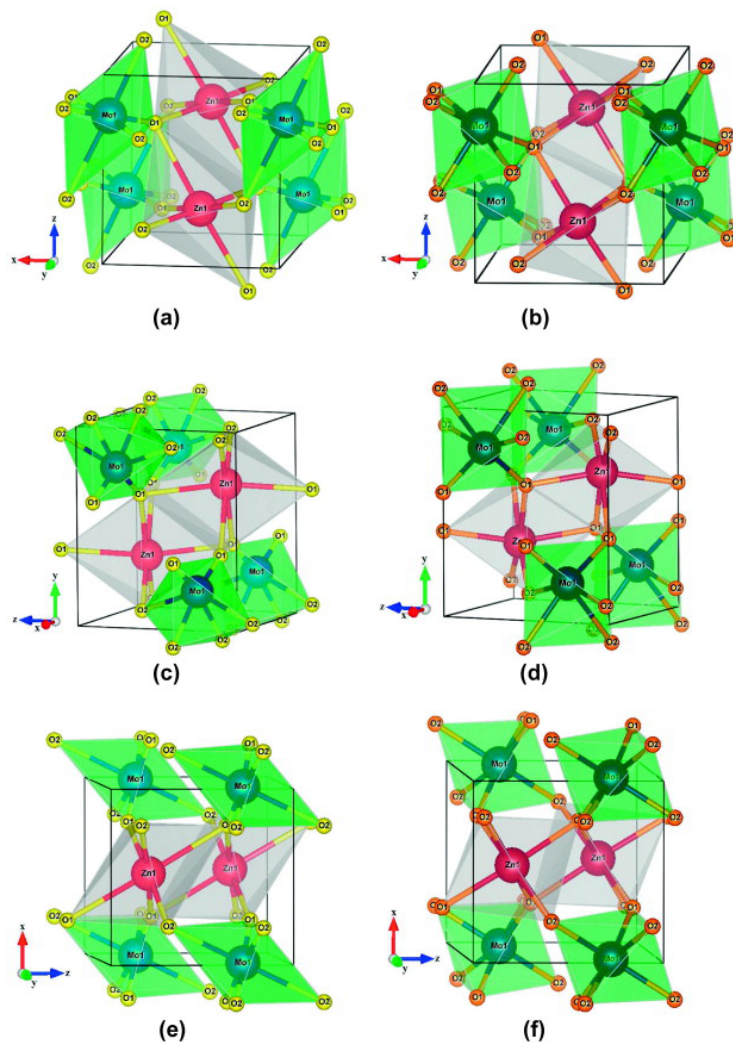


Figure 4.2: Schematic representation of the monoclinic unit cells corresponding to β -ZnMoO₄ crystals projected at same axis: (a, c and e) experimental and (b, d and f) theoretical, respectively.

The lattice parameters and atomic positions obtained from the Rietveld refinement and theoretical calculations presented in Table 4.1 were used to model these unit cells using the Visualization for Electronic and Structural Analysis (VESTA) program, version 3.1.2, for Windows [53]. The monoclinic structure of the β -ZnMoO₄ crystals is characterized by exhibiting a space group $P2/c$, point-group symmetry C_{2h}^4 and two clusters per unit cell ($Z = 2$). In both unit cells, the Zn and Mo atoms are coordinated to six oxygen atoms which form the distorted octahedral [ZnO₆] and [MoO₆] clusters (6-vertices, 6-faces, and 12-edges) [54]. As it can be observed, that the Figures 4.2(a and b); (c and

d); and (e and f) exhibits small differences in (O-Zn-O) and (O-Mo-O) bond angles. However, the experimental β -ZnMoO₄ crystals present minor unit cell volume and major distortions on the octahedral [ZnO₆]/[MoO₆] clusters in relation to unit cell of theoretical β -ZnMoO₄ crystal lattice. In principle, this phenomenon occurs due to experimental conditions required for crystallization and formation of β -ZnMoO₄ crystals and other phenomena involved such as dissolution and re-crystallization mechanisms under HT conditions [55]. These small differences between the experimental and theoretical β -ZnMoO₄ unit cells can be noted in Figures 4.2(a-f).

4.3.3 Fourier-transform Raman/infrared Spectroscopies: Theoretical and experimental analyses of β -ZnMoO₄ crystals

According to the group theory calculations and symmetry [56-58], molybdate and tungstate crystals with a wolframite-type monoclinic structure present $3N = 36$ degrees of freedom. Therefore, there are $N = 12$ atoms within the unit monoclinic cell as illustrated previously (see Figures 4.3(a,b)). In our case, β -ZnMoO₄ microcrystals have 36 distinct vibrational modes (Raman and infrared) as indicated in equation 4.2 [57-58]:

$$\Gamma_{(Raman+Infrared)} = 8A_g + 10B_g + 8A_u + 10B_u \quad (4.2)$$

where the A_g and B_g are Raman-active modes, and A_u and B_u are active vibrational modes in the infrared spectrum; the A and B modes are nondegenerate. The terms “ $_g$ and $_u$ ” subscripts indicate the parity under inversion in centrosymmetric β -ZnMoO₄ crystals. Therefore, only 18 active vibrational modes are

expected in Raman spectra of β -ZnMoO₄ crystals as represented by equation 4.3 below [59]:

$$\Gamma_{(Raman)} = 8A_g + 10B_g \quad (4.3)$$

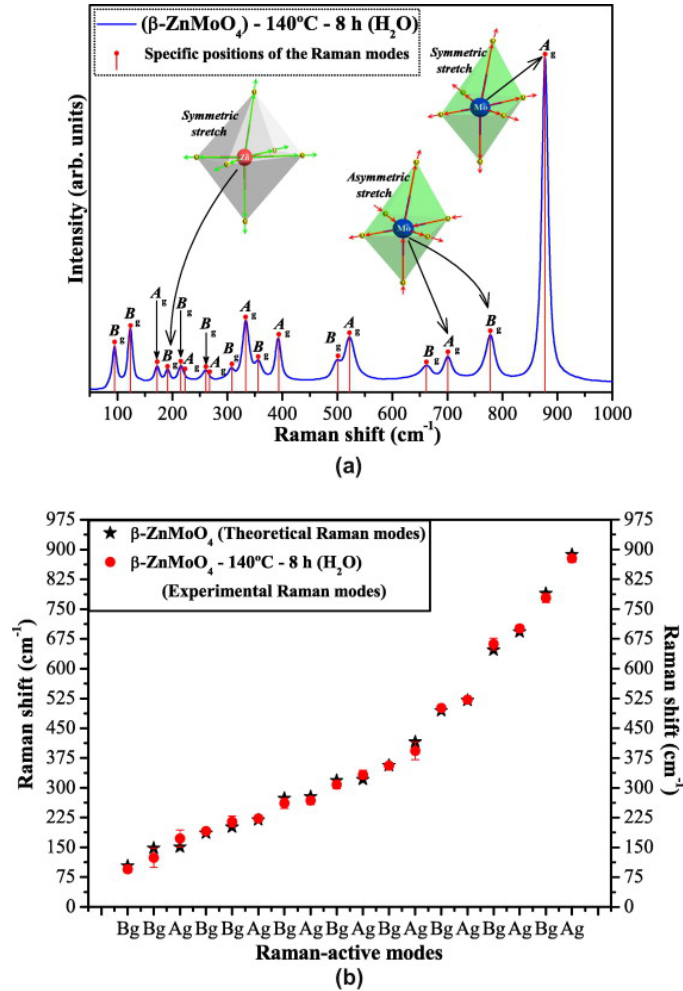


Figure 4.3: (a) FT-Raman spectrum of β -ZnMoO₄ microcrystals synthesized at 140 °C for 8 h in HT system and (b) comparative between the relative positions of theoretical and experimental Raman-active modes.

According to the literature [60-61] and the data obtained from the structural refinement of the β -ZnMoO₄ crystals with a wolframite-type monoclinic structure, these crystals have only distorted octahedral [ZnO₆] and [MoO₆] clusters with a symmetry group O_h , space group $P2/c$ and symmetry site C_2 . Raman spectra of β -ZnMoO₄ crystals can be classified into two types of groups (external and internal modes). External vibrational modes are related

to the lattice phonons which corresponds to the motion of distorted octahedral $[\text{ZnO}_6]$ clusters in the unit cell. The internal vibrational modes are ascribed to vibrations of distorted octahedral $[\text{MoO}_6]$ clusters by assuming a center of mass of the steady state. The distorted octahedral $[\text{MoO}_6]$ clusters have their vibrations composed by six internal modes (four A_g and two B_g). The other vibrational modes with low values in Raman spectra are external modes.

Figures 4.3(a) and (b) illustrate the FT-Raman spectrum and specific theoretical/experimental Raman modes of β - ZnMoO_4 microcrystals, respectively.

In Figure 4.3(a), we can identify eighteen Raman active vibrational modes between 50 and $1,000\text{ cm}^{-1}$ for β - ZnMoO_4 microcrystals synthesized at 140°C for 8 h by the HT method. The main Raman (A_g) mode referent to intense peak located at around 878 cm^{-1} is assigned to the symmetric stretch of bonds ($\leftarrow\text{O}\leftarrow\text{Mo}\rightarrow\text{O}\rightarrow$) (see inset Figure 4.3(a)). Moreover, two Raman (A_g and B_g) modes at approximately (778 cm^{-1} and 701 cm^{-1}) are assigned to the asymmetric stretch of bonds ($\rightarrow\text{O}\rightarrow\text{Mo}\rightarrow\text{O}\rightarrow$) [62] (see inset Figure 4.3(a)) while a Raman (B_g) mode of low intensity at around 191 cm^{-1} is ascribed to the symmetric stretch of bonds ($\leftarrow\text{O}\leftarrow\text{Zn}\rightarrow\text{O}\rightarrow$) (see inset Figure 4.3(a)) [63]. Therefore, all Raman peaks correspond to a wolframite-type monoclinic structure. The experimental positions of 18 Raman vibrational modes were identified (\bullet) and compared with those Raman-active modes calculated theoretically through atomic positions and lattice parameters for the optimized β - ZnMoO_4 crystal (see Figure 4.3(b)) and their respective experimental and theoretical positions are listed in the Supplementary data (Table-S1).

In Figure 4.3(b), there is good agreement between the Raman-active modes of β - ZnMoO_4 microcrystals synthesized experimentally and theoretically obtained from *ab-initio* calculations. Some small variations in the

typical positions of the vibrational modes can be caused by preparation methods, average crystal size, distortions on the (O-Zn-O)/(O-Mo-O) bonds, internal forces interactions between the $[\text{ZnO}_6]$ - $[\text{MoO}_6]$ - $[\text{ZnO}_6]$ clusters and/or different degrees of structural order-disorder within the lattice. Moreover, our theoretical calculation does not consider the non-harmonic contribution to the lattice vibrations.

As described earlier, Raman and infrared spectra display 34 different vibrational modes that were presented in equation 4.2. Only some of these modes are active in the infrared spectrum. Therefore, only 18 vibrational modes are expected in the infrared spectrum of β - ZnMoO_4 crystals, as represented by equation 4.4 below:

$$\Gamma_{(Raman)} = 8A_u + 10B_u \quad (4.4)$$

However, three modes ($1A_u$ and $2B_u$) are only acoustic vibrations and can not be detected in the infrared spectrum. Therefore, equation 4.4 should be reduced and can be better represented by the following equation 4.5 [64-66]:

$$\Gamma_{(Raman)} = 7A_u + 8B_u \quad (4.5)$$

In general, infrared (IR) spectroscopy elucidates the different types of vibrational modes between the atoms and their inter-atomic bonds in molybdates [67].

Figures 4.4(a) and (b) illustrate the FT-IR spectrum and specific theoretical/experimental infrared modes of β - ZnMoO_4 microcrystals, respectively.

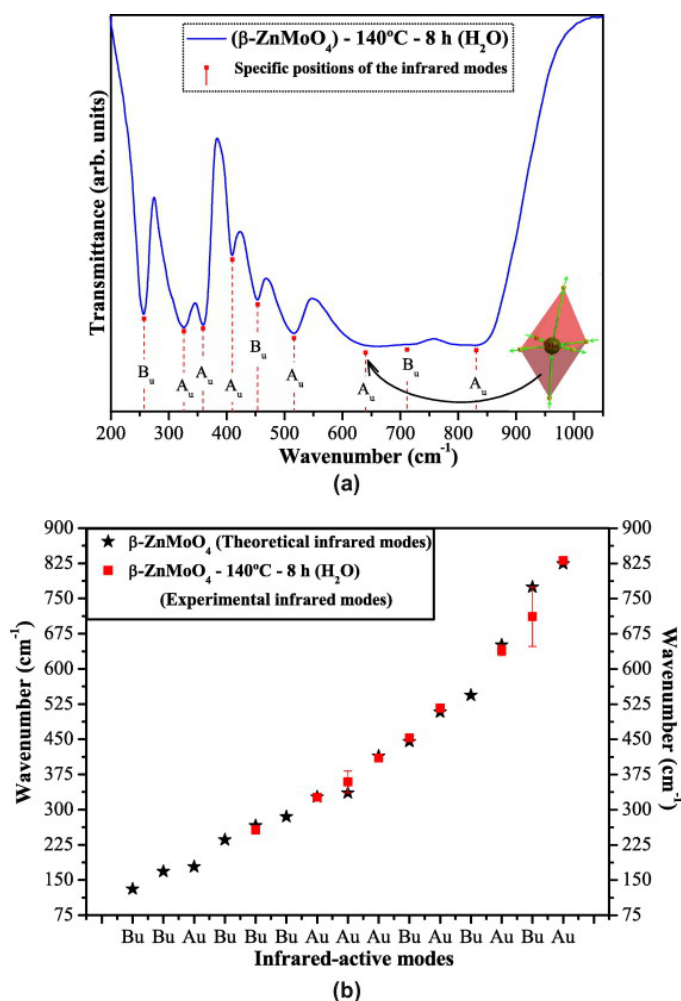


Figure 4.4: (a) FT-IR spectrum of β -ZnMoO₄ microcrystals synthesized at 140 °C for 8 h in HT system and (b) comparative between the relative positions of theoretical and experimental IR-active modes.

In Figure 4.4(a) shows eight infrared-active vibrational modes between 50 and 1,050 cm^{-1} for β -ZnMoO₄ microcrystals synthesized at 140°C for 8 h by the HT method. A very narrow band at around 257 cm^{-1} is due to the (B_u) mode with the anti-symmetric stretch of bonds and interaction forces between the $[\text{ZnO}_6] \leftrightarrow [\text{ZnO}_6]$ clusters. Thus, two (A_u) modes at approximately 326 and 359 cm^{-1} are related to the symmetric stretch ($\text{O} \leftarrow \text{Zn} \leftarrow \text{O} \rightarrow \text{Zn} \rightarrow \text{O}$) of the distorted octahedral $[\text{ZnO}_6]$ - $[\text{ZnO}_6]$ clusters in a chain. The A_u mode at around (410 cm^{-1}) is ascribed to an anti-symmetric stretch ($\rightarrow \text{O} \rightarrow \text{Zn} \rightarrow \text{O} \rightarrow$) of distorted octahedral $[\text{ZnO}_6]$ clusters. Two bands at approximately 453 and 516 cm^{-1} are assigned to B_u e A_u modes which are related to the anti-symmetric

stretch ($\text{O} \leftarrow \text{Mo} \leftarrow \text{O} \leftarrow \text{Mo} \leftarrow \text{O}$) of distorted octahedral $[\text{MoO}_6]$ - $[\text{MoO}_6]$ clusters in a chain. A broad band at around 665 cm^{-1} corresponds to an A_u mode which is the main band in the infrared spectrum of β - ZnMoO_4 crystals (see inset Figure 4.4(a)) with distorted octahedral $[\text{MoO}_6]$ clusters which are assigned to an anti-symmetric stretching. Also, a shoulder at 712 cm^{-1} is related to the B_u mode. Finally, the band at around 829 cm^{-1} is related to A_u mode which is assigned to symmetric stretch ($\leftarrow \text{O} \leftarrow \text{Mo} \rightarrow \text{O} \rightarrow$) of the distorted octahedral $[\text{MoO}_6]$ clusters. Typical theoretical and experimental positions (■) of IR-actives modes are shown in Figure 4.4(b). Moreover, their respective experimental and theoretical values are listed in the Supplementary data-Table-S2.

Figure 4.4(b) indicates a good conformity between the wavenumbers of the infrared-active modes which are experimentally determined and theoretically calculated. Moreover, theoretical results evidence the presence of some (B_g and A_g) modes at 131.17 cm^{-1} , 168.42 cm^{-1} , 178.3 cm^{-1} , 236.03 cm^{-1} , 285.26 cm^{-1} and 544.19 cm^{-1} which were not experimentally detected due to the low detection limit imposed by the FT-IR spectrophotometer. In terms of spectral positions, small deviations in the IR-active modes of β - ZnMoO_4 microcrystals can be attributed to different degrees of interaction and modification on the O-Zn-O and O-Mo-O bond lengths and/or angles within the distorted octahedral $[\text{ZnO}_6]$ and $[\text{MoO}_6]$ clusters. We have noted that some of these infrared vibrational modes of β - ZnMoO_4 microcrystals are similar to isostructural ZnWO_4 crystals [68-69].

4.3.4 Ultraviolet-visible absorption spectroscopy and band structures of β -ZnMoO₄ crystals

The optical band gap energy (E_{gap}) was calculated by the method proposed by Kubelka and Munk [70]. This methodology is based on the transformation of diffuse reflectance measurements to estimate E_{gap} values with good accuracy within the limits of assumptions when modeled in three dimensions [71]. Particularly, it is useful in limited cases of an infinitely thick sample layer. The Kubelka-Munk equation for any wavelength is described by equation 4.6:

$$F(R_{\infty}) = \frac{(1 - R_{\infty})^2}{2R_{\infty}} = \frac{k}{s} \quad (4.6)$$

where $F(R_{\infty})$ is the Kubelka-Munk function or absolute reflectance of the sample. In our case, magnesium oxide (MgO) was the standard sample in reflectance measurements. $R_{\infty} = R_{sample}/R_{MgO}$ (R_{∞} is the reflectance when the sample is infinitely thick), k is the molar absorption coefficient and s is the scattering coefficient. In a parabolic band structure, the optical band gap and absorption coefficient of semiconductor oxides [72] can be calculated by the following equation 4.7:

$$\alpha h\nu = C_1(h\nu - E_{gap})^n, \quad (4.7)$$

where α is the linear absorption coefficient of the material, $h\nu$ is the photon energy, C_1 is a proportionality constant, E_{gap} is the optical band gap and n is a constant associated with different kinds of electronic transitions ($n = 0.5$ for a direct allowed, $n = 2$ for an indirect allowed, $n = 1.5$ for a direct forbidden

and $n = 3$ for an indirect forbidden). According to the literature, the isostructural ZnWO_4 crystals exhibit an optical absorption spectrum governed by direct electronic transitions [73-75]. In this phenomenon, after the electronic absorption process, the electrons located in the maximum-energy states in the valence band revert to minimum-energy states in the conduction band under the same point in the Brillouin zone [75-76]. Based on this information, E_{gap} values of $\beta\text{-ZnMoO}_4$ crystals were calculated using $n = 0.5$ in equation 4.7. Finally, using the remission function described in equation 4.6 and with the term $k = 2\alpha$, we obtain the modified Kubelka-Munk equation as indicated in equation 4.8

$$[F(R_\infty)h\nu]^2 = C_2(h\nu - E_{gap}), \quad (4.8)$$

Therefore, finding the $F(R_\infty)$ value from 4.8 and plotting a graph of $[F(R_\infty)h\nu]^2$ against $h\nu$, the E_{gap} of $\beta\text{-ZnMoO}_4$ microcrystals was determined.

Figures 4.5(a) and (b) illustrate the UV-vis spectrum of $\beta\text{-ZnMoO}_4$ microcrystals synthesized at 140°C for 8 h by HT method and their band structure, respectively.

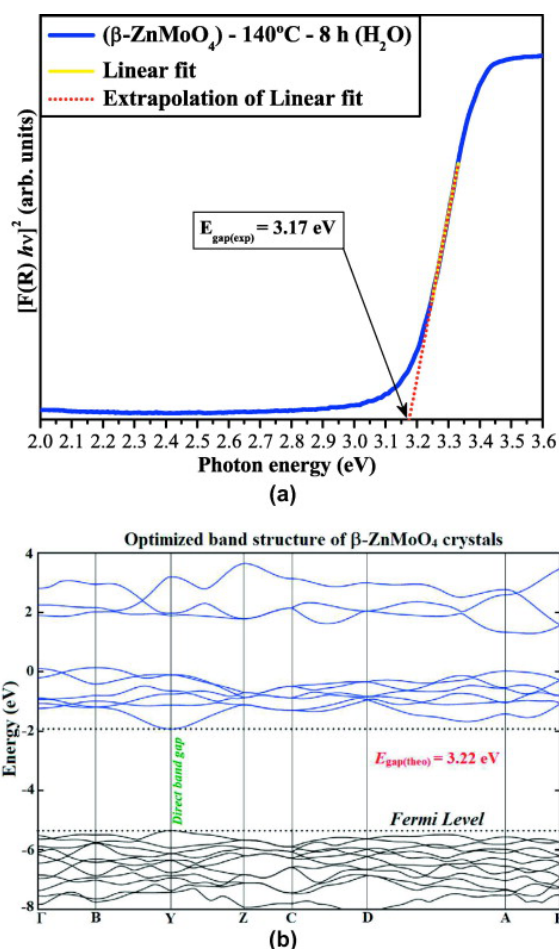


Figure 4.5: (a) UV-Vis spectra of $\beta\text{-ZnMoO}_4$ microcrystals synthesized at 140°C for 8 h in HT system and (b) optimized band structure of $\beta\text{-ZnMoO}_4$ crystals.

The profile of the UV-vis spectrum for $\beta\text{-ZnMoO}_4$ microcrystals indicates a typical optical behavior of structurally ordered crystalline materials. This microcrystal exhibits a direct E_{gap} value of 3.17 eV (see Figure 4.5(a)). Figure 4.5(b) reveals that band structures of $\beta\text{-ZnMoO}_4$ crystals are characterized by well defined direct electronic transitions; i.e., the top of the valence band (VB) as well as the bottom of the conduction band (CB) are at the same $Y \leftrightarrow Y (0, 0.5, 0)$ point. Therefore, it was verified that theoretical band gap values ($E_{\text{gap}} = 3.22 \text{ eV}$) are close to values experimentally estimated by UV-vis spectra (Figure 4.5(a)).

4.3.5 Density of states of β -ZnMoO₄ crystals

Figures 4.6(a) and (b) illustrate the DOS projected over the most important orbitals of the O and Mo atoms and the total DOS projected over all atoms involved in the electronic structure of β -ZnMoO₄ crystals, respectively.

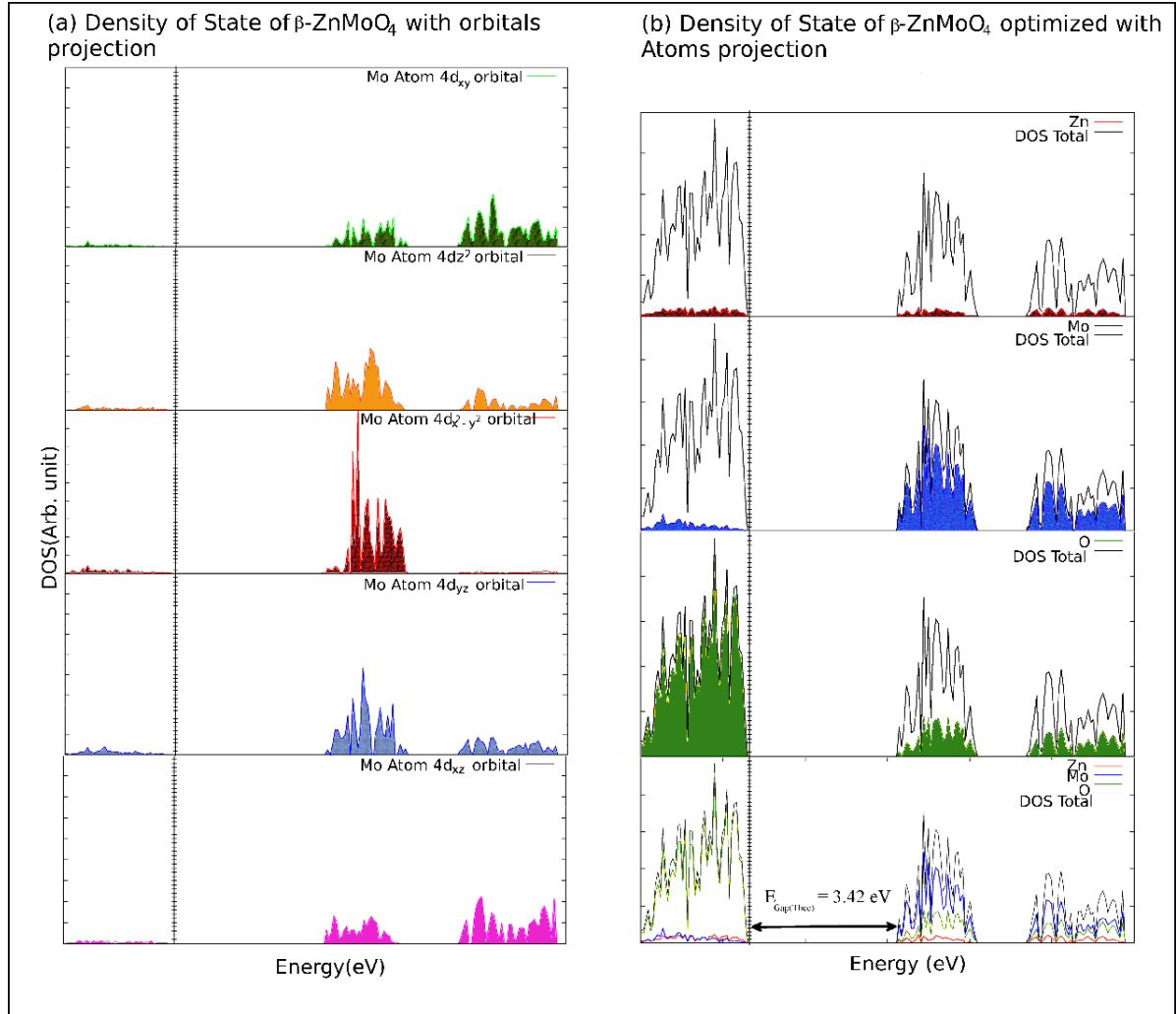


Figure 4.6: (a) Projected partial DOS on the Mo orbitals and (b) projected total DOS on the Zn, Mo and O orbitals for the β -ZnMoO₄ crystals.

Figure 4.6(a) shows that the top of the VB are composed mainly of O ($2p_x$, $2p_y$, and $2p_z$ atomic orbitals) that connect with both Zn and Mo atoms. The lower part of the CB is formed mainly by Mo ($4d_{xy}$, $4d_{xz}$ and $4d_{yz}$, $4d_{x^2-y^2}$ and $4d_{z^2}$ atomic orbitals). In addition, was verified a slight contribution

of the O $2p$ orbitals. In an octahedral field, the $4d$ orbitals of the Mo atoms are not degenerate; they first split in the t_{2g} ($4d_{xy}$, $4d_{xz}$, and $4d_{yz}$) and e_g ($4d_{x^2-y^2}$ and $4d_{z^2}$) orbitals. The e_g orbitals have lobes that point at the oxygen ligands and thus will ascend in energy; the t_{2g} orbitals have lobes that lie between ligands and thus will descend in energy (in the VB), but due to the distortion in octahedral $[\text{MoO}_6]$ clusters, they present five different energies. The order of energies are opposite in the virtual bands so the most important contributions in the lower part of the CB are due to e_g orbitals followed by $4d_{yz}$ (t_{2g}) and to a lesser extent, to the ($4d_{xy}$ and $4d_{xz}$) orbitals (see Figures 4.6(a,b) lists the total DOS of all orbitals for β - ZnMoO_4 crystals. This total DOS shows that Zn atomic orbitals have a minimal contribution (between - 8 eV and 4 eV) due to a weak hybridization between the Zn and O orbitals. On the other hand, the total DOS indicates a strong hybridization between O $2p$ (above the VB) and Mo $4d$ orbitals (near the CB), respectively. Therefore, this analysis performed on the total orbital-resolved DOS denotes a significant dependence of Mo ($4d$) orbitals in the CB. In general, this behavior can be correlated with distortions on the octahedral $[\text{MoO}_6]$ clusters within the monoclinic structure which are responsible for the origin of intermediary energy levels located above the CB.

4.3.6 Electron density maps and PL emission of β - ZnMoO_4 crystals

Figures 4.7(a-d) show electron density maps performed on the Zn, Mo, O atoms and Zn-Mo atoms in different planes. Figure 4.7(e) shows the possible mechanism of charge transference between the $[\text{ZnO}_6]$ - $[\text{MoO}_6]$ / $[\text{ZnO}_6]$ - $[\text{ZnO}_6]$ clusters involved in a monoclinic structure and Figure 4.7(f) shows the

PL behavior of β -ZnMoO₄ microcrystals synthesized at 140°C for 8 h by the HT method, respectively.

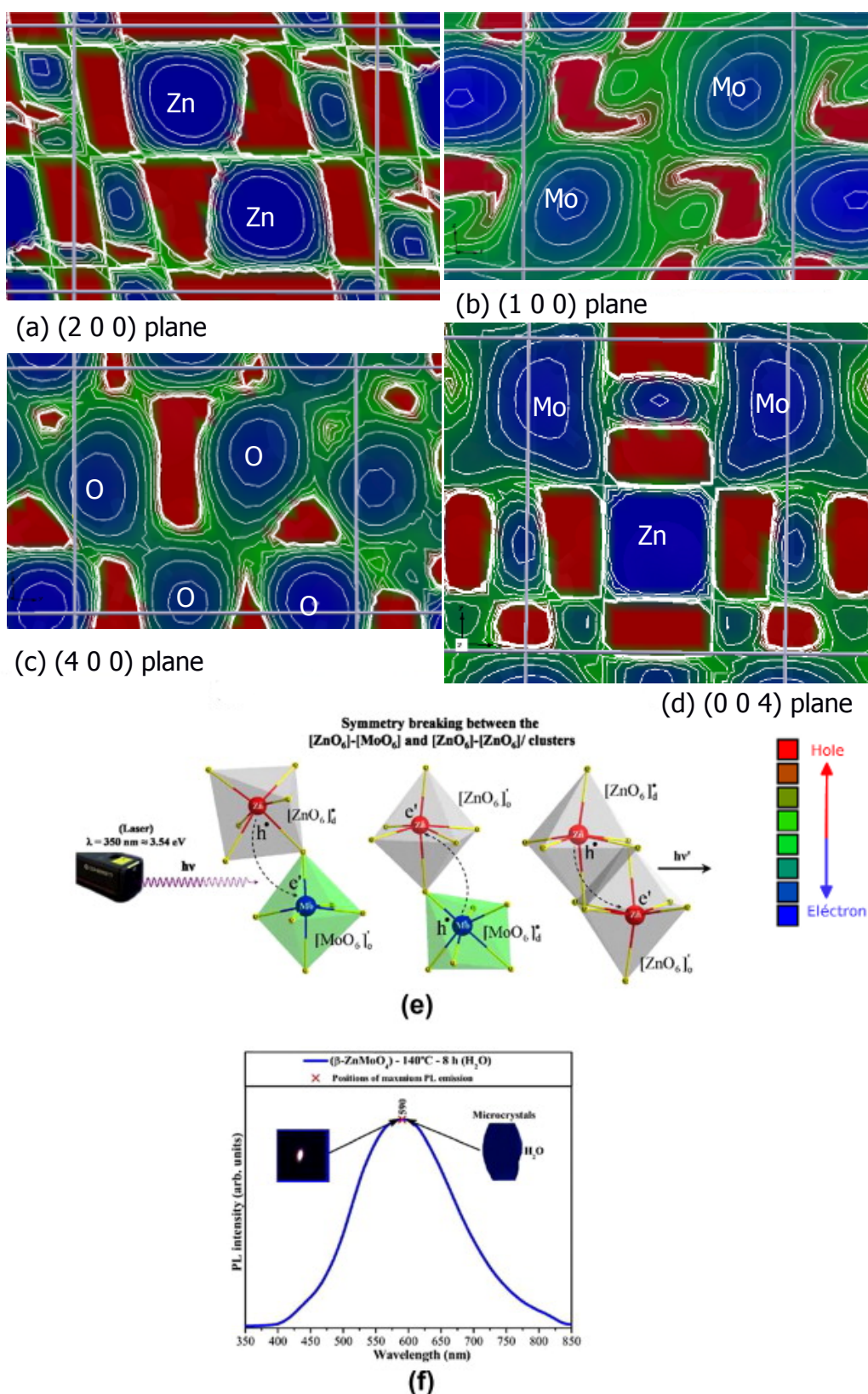
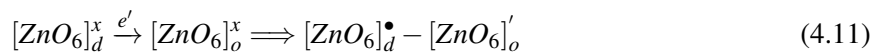
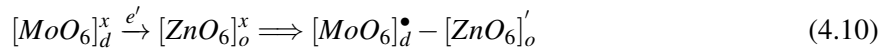
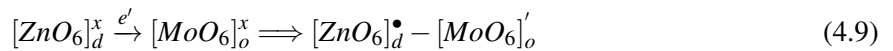


Figure 4.7: Electronic density map on the: (a) (2 0 0) plane, (b) (1 0 0) plane, (c) (4 0 0) plane, and (d) (0 0 4) plane of the $\beta\text{-ZnMoO}_4$ crystals (e) Possible mechanism of charge transference between the clusters and (f) PL spectra of $\beta\text{-ZnMoO}_4$ microcrystals synthesized at 140 °C for 8 h in HT system. Insets show the digital photographs of its corresponding PL emissions and FE-SEM image of individual microcrystal, respectively.

Figure 4.7(a) shows the electronic density map on the Zn atoms in (200) plane of β -ZnMoO₄ crystals. The regions in dark blue can be ascribed to a high electronic density or the number of electrons (e') located in Zn atoms and between the [ZnO₆]-[ZnO₆] clusters while the region in red indicates the possible absence of the e' between the [ZnO₆]-[MoO₆]-[ZnO₆] clusters. Moreover, we can verify that these regions have a value near zero which is donated in internal scale (see inset Figure 4.7(a)). Regions with medium electronic density (in light blue) are possibly related to O atoms which are bonded to Zn atoms. Figure 4.7(b) depicts the electronic density map on Mo atoms in the (100) plane of β -ZnMoO₄ crystals. Regions in dark blue and light blue indicate a high electronic density for Mo atoms while the region in red indicates the absence of an electronic density between the [MoO₆]-[ZnO₆]-[MoO₆] clusters. In addition, was verified that these regions have a value near zero which is donated in internal scale (see inset Figure 4.7(b)). In addition, circular green regions can possibly be related to O atoms bonded with Mo atoms. Figure 4.7(c) illustrates the electronic density map on the O atoms in the (400) plane of β -ZnMoO₄ crystals. In this plane, a high electronic density corresponding to O atoms in circular blue and green regions can be verified. However, the O atoms are not equidistant due to distortions of the bonds present in octahedral on [MoO₆] and [ZnO₆] clusters which is in good agreement with models shown in Figures 4.2(a-f). Based on this information, it is possible to confirm that $2p$ orbitals of O atoms are hybridized with $4d_{x^2-y^2}$ and $4d_{z^2}$ orbitals of Mo atoms are located on the axes in base of octahedron and apex of octahedron non-formed angles of 90°. Figure 4.7(d) illustrates the electronic density map on the Zn and Mo atoms in the (004) plane of β -ZnMoO₄ crystals. In this figure can be confirmed that two Mo atoms are interconnected to one O atom with a high electronic density. Thus, the Zn atom is equidistant to two Mo atoms, and the region in

different colors indicates that there is an inhomogeneous electron distribution and charges between distorted octahedral $[\text{MoO}_6]$ and $[\text{ZnO}_6]$ clusters.

Figure 4.7(e) shows the laser employed in the excitation of $\beta\text{-ZnMoO}_4$ microcrystals. The wavelength energy (350 nm \approx 3.543 eV) is able to excite several electrons localized in intermediary energy levels within the band gap (see Figure 4.5(a)). These direct electronic transitions in the band gap occur in the same region of the Brillouin zone between the maximum-energy states near to minimum-energy states (see Figure 4.5(b)). During the excitation process at room temperature, some electrons localized at lower intermediary energy levels (O $2p$ orbitals) near the VB absorb photon energies ($h\nu$). As a consequence of this phenomenon, the energetic electrons are promoted to higher intermediary energy levels (Mo $4d$ orbitals) located near the CB (see Figure 4.6(b)). When the electrons revert to lower energy states, (again via radiative return processes), energies arising from this electronic transition are converted to photons ($h\nu'$) (see Figure 4.7(e)). Moreover, the Figure 4.7(e) shows our proposed model of electron transfer between clusters to origin PL emission of $\beta\text{-ZnMoO}_4$ crystals. In this model, we can attribute the possible process of charge transfer between the $[\text{ZnO}_6]_d^x$ - $[\text{MoO}_6]_o^x$, $[\text{MoO}_6]_d^x$ - $[\text{ZnO}_6]_o^x$ or $[\text{ZnO}_6]_d^x$ - $[\text{ZnO}_6]_o^x$ clusters in the monoclinic lattice of $\beta\text{-ZnMoO}_4$ crystals due to order-disorder effects between clusters caused by a constant process of charge transfer according to Equations (4.9), (4.10) and (4.11):



In these equations, the cluster-to-cluster charge-transfer (CCCT) in a crystal containing more than one kind of cluster is characterized by excitations involving electronic transitions from one cluster to another cluster [77]. Gracia *et al.* [78] have demonstrated that the CCCT mechanism in CaWO_4 crystals at excited states (excited singlet and excited triplet) can be considered a new class of electronic transitions which are involved in PL emissions. In this work, we consider that within the $\beta\text{-ZnMoO}_4$ lattice, the octahedral $[\text{ZnO}_6]_d^x$ - $[\text{MoO}_6]_o^x$, $[\text{MoO}_6]_d^x$ - $[\text{ZnO}_6]_o^x$ or $[\text{ZnO}_6]_d^x$ - $[\text{ZnO}_6]_o^x$ clusters (o = ordered and d = disordered/distorted) arise from structural distortions in a monoclinic structure where the occurrence of electronic transference between them is possible. Therefore, several photons ($h\nu'$) originating from the participation of different energy states during electronic transitions between the VB and CB of $\beta\text{-ZnMoO}_4$ crystals are responsible for their broad PL properties (see Figure 4.7(f)).

4.4 Conclusions

In summary, $\beta\text{-ZnMoO}_4$ microcrystals were synthesized successfully by the conventional HT method at 140°C for 8 h. XRD patterns and Rietveld refinement data demonstrate that $\beta\text{-ZnMoO}_4$ microcrystals are monophasic with a wolframite-type tetragonal structure and space group $P2/c$. FT-Raman and FT-IR spectroscopies have been employed to verify the vibrational modes while UV-vis absorption spectroscopy and PL measurements were used to investigate their optical properties. The experimental Raman and infrared modes are in good agreement with theoretical results. UV-vis absorption spectra showed an optical band gap which are associated with the presence of in-

intermediary energy levels between the VB and CB. The band structure reveals a direct band gap from Y to Y point for β -ZnMoO₄ microcrystals. According to the DOS analyses, the energy states in the VB are constituted mainly from O ($2p_x$, $2p_y$, and $2p_z$) orbitals, while in the CB there is the main contribution from Mo ($4d_{xy}$, $4d_{xz}$ and $4d_{yz}$, $4d_{x^2-y^2}$ and $4d_{z^2}$, respectively). An electron density map shows an inhomogeneous electronic distribution of charges between distorted octahedral [MoO₆] and [ZnO₆] clusters. The PL behavior of β -ZnMoO₄ microcrystals is associated with distortion effects on the octahedral [ZnO₆] and [MoO₆] into the monoclinic structure.

Acknowledgements

The authors thank the financial support of the Brazilian research financing institutions: CNPq-DCR (350711/2012-7), FAPESP (N^o. 2009/50303-4), FAPEPI-GERATEC (N^o. 01.08.0506.00), and CAPES.

4.5 References

- [01] S.C. Abrahams, J. Chem. Phys. 46 (1967) 2052-2063.
- [02] Y. Li, G. Weisheng, B. Bo, G. Kaijie, IEEE Internat. Confer Energy Environm. Techn. 3 (2009) 672-675.
- [03] G. Zhang, S. Yu, Y. Yang, W. Jiang, S. Zhang, B. Huang, J. Crys. Growth. 312 (2010) 1866-1874.
- [04] W. Reichelt, T. Weber, T. Söhnel, S. Däbritz, Z. Anorg. Allg. Chem. 626 (2000) 2020-2027.
- [05] T. Söhnel, W. Reichelt, H. Oppermann, H. J. Mattauch, A. Simon, Z. Anorg. Allg. Chem. 622 (1996) 1274-1280.

-
- [06] K. Pavani, A Ramanan, *Eur. J. Inorg. Chem.* 2005 (2005) 3080-3087.
- [07] D. Spassky, A. Vasilev, I. Kamenskikh, V. Kolobanov, V. Mikhailin, A. Savon, L. Ivleva, I. Voronina, L. Berezovskaya, *Phys. Status Solidi. A.* 206 (2009) 1579-1583.
- [08] T.N. Nikolaenko, Y.A. Hizhnyi, S.G. Nedilko, *J. Lumin.* 128 (2008) 807-810.
- [09] L.I. Ivleva, I.S. Voronina, L.Y. Berezovskaya, P.A. Lykov, V.V. Osiko, L.D. Iskhakova, *Crystallogr. Rep.* 53 (2008) 1087-1090.
- [10] X. Ju, X. Li, W. Li, W. Yang, C. Tao, *Mater. Lett.* 65 (2011) 2642-2644.
- [11] L. Yu, M. Nagami, *Mater. Lett.* 64 (2010) 1644-1646.
- [12] A. Xei, X. Yuan, F. Wang, Y. Shi, Z. Mu, *J. Phys. D. Appl. Phys.* 43 (2010) 055101-055105.
- [13] Z. Chunlei, H. Yunsheng, Z. Weidong, H. Xiaowei, *J. Rare Earths.* 27 (2009) 758-760.
- [14] L.Y. Zhou, J.S. Wei, F.Z. Gong, J.L. Huang, L.H. Yi, *J. Solid. State. Chem.* 181 (2008) 1337-1341.
- [15] A. Kumar, J. Kumar, *J. Mater. Chem.* 21 (2011) 3788-3795.
- [16] V.B. Mikhailik, H. Kraus, D. Wahl, H. Ehrenberg, M.S. Mykhaylyk, *Nucl. Instrum. Methods Phys. Res. Sect. A.* 562 (2006) 513-516.
- [17] C. Arnaboldi, C. Brofferio, O. Cremonesi, L. Gironi, M. Pavan, G. Pessina, S. Pirro, E. Previtali, *Astropart. Phys.* 34 (2011) 797-804.
- [18] L. Gironi, C. Arnaboldi, J.W. Beeman, O. Cremonesi, F.A. Danevich, V.Y. Degoda, L.I. Ivleva, L.L. Nagornaya, M. Pavan, G. Pessina, S. Pirro, V.I. Tretyak, V.I. Tupitsyna. *J. Instrum.* 5 (2010) P11007-P11017.
- [19] L.L. Nagornaya, F.A. Danevich, A.M. Dubovik, B.V. Grinyov, S. Henry, V. Kapustyanyk, H. Kraus, D.V. Poda, V.M. Kudovbenko, V.B. Mikhailik, M. Panasyuk, O.G. Polischuk, V. Rudyk, V. Tsybul'skyi, I.A. Tupitsyna, Y.Y.

- Vostretsov, IEEE. Trans. Nucl. Sci. 56 (2009) 2513-2518.
- [20] J. Guo, D. Zhou, H. Wang, X. Yao, J. Alloys Compd. 509 (2011) 5863-5865.
- [21] B.D. Amo, R. Ramagnoli, V.F. Vetetre. J. Appl. Electrochem. 29 (1999) 1401-1407.
- [22] N.N. Leyzerovich, K.G. Bramnik, T. Buhrmester, H. Ehrenberg, H. Fuess, J. Power. Sourc. 127 (2004) 76-84.
- [23] C.C. Chen, Y.R. Jiang, K.H. Chang, Adv. Mater. Res. 557 (2012) 761-766.
- [24] L. Lv, W. Tong, Y. Zhang, Y. Su, X. Wang, J. Nanosci. Nanotechnol. 11 (2011) 9506-9512.
- [25] A.M.E.S. Raj, C. Mallika, K. Swaminathan, O.M. Sreedharan, K.S. Nagaraja, Sens. Actuators B. Chem. 81 (2002) 229-236.
- [26] N. Sotani, T. Suzuki, K. Nakamura, K. Eda, S. Hasegawa, J. Mater. Sci. 36 (2001) 703-713.
- [27] A.L. Kruglyashov, E.M. Skou, Solid State Ionics. 28 (1988) 233-236.
- [28] A. Manthiram, J. Gopalakrishnan, Mater. Res. Bull. 15 (1980) 207-211.
- [29] AM. Dubovik, Y.Y. Vostretsov, B.V. Grinyov, F.A. Danevich, H. Kraus, L.L. Nagornaya, V.B. Mikhailik, I.A. Tupitsyna, Acta Phys. Polonica. A. 117 (2010) 15-19.
- [30] C.V. Bhuvana, B. Viswanathan, M.V.C. Sastri, Indian J. Chemistry. 1A (1979) 385-387.
- [31] A. Sen, P. Pramanik, Mater. Lett. 50 (2001) 287-294.
- [32] C. Peng, L. Gao, S. Yang, J. Sun, Chem. Commun. 43 (2008) 5601-5603.
- [33] J.H. Ryu, S.M. Koo, J.W. Yoon, C.S. Lim, K.B. Shim, Mater. Lett. 60 (2006) 1702-1705.
- [34] R.P. Jia, Y.Q. Zhang, J. Nanopart. Res. 12 (2010) 2717-2721.
- [35] G. Tian, Y. Chen, W. Zhou, K. Pan, Y. Dong, C. Tian, H. Fu, J. Mater.

Chem. 21 (2011) 887-892.

[36] M. Hashim, C. Hu, Y. Chen, C. Zhang, Y. Xi, J. Xu, Phys. Status Solidi. A. 208 (2011) 1937-1941.

[37] J.C. Sczancoski, M.D.R. Bomio, L.S. Cavalcante, M.R. Joya, P.S. Pizani, J.A. Varela, E. Longo, M.S. Li, J.A. Andres, J. Phys. Chem. C. 113 (2009) 5812-5822.

[38] X. Cui, S.H. Yu, L. Li, L. Biao, H. Li, M. Mo, X.M. Liu, Chem. Eur. J. 10 (2004) 218-223.

[39] L.S. Cavalcante, J.C. Sczancoski, M. Siu Li, E. Longo, J.A. Varela, Coll. Surf. A. 396 (2012) 346-351.

[40] R. Jia, C. Zhang, J. Xu, Adv. Mater. Res. 624 (2012) 51-54.

[41] L. Wei, L. Xuan, W. Li, L. Xin, Chinese J. Lumin. 33 (2012) 1283-1288.

[42] D.A. Spassky, A.N. Vasilev, I.A. Kamenskikh, V.V. Mikhailin, A.E. Savon, Y.A. Hizhnyi, S.G. Nedilko, P.A. Lykov, J. Phys. Condens. Matter. 23 (2011) 365501-365510.

[43] R. Dovesi, V.R. Saunders, C. Roetti, R. Orlando, C.M. Zicovich-Wilson, F. Pascale, B. Civalleri, K. Doll, N.M. Harrison, I.J. Bush, P. D'Arco, M. Llunell, *CRYSTAL09 User's Manual* (University of Torino, Torino, 2009).

[44] A.D. Becke, J. Chem. Phys. 98 (1993) 5648-5652.

[45] C. Lee, R.G. Yang, R.G. Parr, Phys. Rev. B. 37 (1988) 785-789.

[46] http://www.crystal.unito.it/Basis_Sets/Ptable.html

[47] P.J. Hay, W.R. Wadt, J. Chem. Phys. 82 (1985) 270-283.

[48] A. Kokalj, J. Mol. Graph. 17 (1999) 176-179.

[49] J. Meullemestre, E. Penigault, Bull. Soc. Chim. France. 10 (1972) 3669-3674.

[50] H.M. Rietveld, Acta Cryst. 2 (1967) 65-71.

[51] <http://www.ing.unitn.it/~maud/>

- [52] L. Lutterotti, S. Matthies, H.R. Wenk, A.J. Schultz, J.J. Richardson, J. Appl. Phys. 81 (1997) 594-600.
- [53] K. Momma, F. Izumi, J. Appl. Crystallogr. 44 (2011) 1272-1276.
- [54] <http://en.wikipedia.org/wiki/Octahedron>
- [55] L.S. Cavalcante, J.C. Sczancoski, R.L. Tranquilin, J.A. Varela, E. Longo, M.O. Orlandi, Particuology. 7 (2009) 353-362.
- [56] M. Crane, R.L. Frost, P.A. Williams, J.T. Kloprogge, J. Raman Spectrosc. 33 (2002) 62-66.
- [57] R.L. Frost, L. Duong, M. Weier, Spectrochim. Acta Part. A. 60 (2004) 1853-1859.
- [58] L.H. Hoang, N.T.M. Hien, W.S. Choi, Y.S. Lee, K. Taniguchi, T. Arima, S. Yoon, X.B. Chen, I.S. Yang, J. Raman Spectrosc. 41 (2010) 1005-1010.
- [59] T.T. Basiev, A.Ya. Karasik, A.A. Sobol, D.S. Chunaev, V.E. Shukshin, Quant. Electron. 41 (2011) 370-372.
- [60] Y. Liu, H. Wang, G. Chen, Y.D. Zhou, Y. Gu, B.Q. Hu, J. Appl. Phys. 64 (1988) 4651-4653.
- [61] M.A.P. Almeida, L.S. Cavalcante, M. Siu Li, J.A. Varela, E. Longo, J. Inorg. Organomet. Polym. 22 (2012) 264-271.
- [62] M. Markova-Velichkova, R. Iordanova, Y. Dimitriev, Phys. Status Solidi C. 8 (2011) 3159-3162.
- [63] N.M. Hung, L.T. Hang, N.V. Khanh, D.T.X. Thao, N.V. Minh, J. Nonlin. Opt. Phys. Mater. Vol. 21, (No. 1) (2012) 1250002-1250012.
- [64] V.V. Fomichev, I. Kondratov, Spectrochim. Acta. 50A (1994) 1113-1120.
- [65] P. Siri Wong, T. Thongtem, A. Phuruangrat, S. Thongtem, CrystEngComm. 13 (2011) 1564-15969.
- [66] Y. Keereeta, T. Thongtem, S. Thongtem, J. Alloys Compd. 509 (2011) 6689-6695.

- [67] M.R.D. Bomio, L.S. Cavalcante, M.A.P. Almeida, R.L. Tranquilin, N.C. Batista, P.S. Pizani, M. Siu Li, J. Andres, E. Longo, *Polyhedron*. 50 (2013) 532-545.
- [68] K.M. Garadkar, A. Ghule, K.B. Sapnar, S.D. Dhole, *Mater. Res. Bull.* 48 (2013) 1105-1109.
- [69] M. Mancheva, R. Iordanova, Y. Dimitriev, *J. Alloys Compd.* 509 (2011) 15-20.
- [70] P. Kubelka, F. Munk-Aussig, *Zeit. Für. Tech. Physik.* 12 (1931) 593-601.
- [71] A.E. Morales, E.S. Mora, U. Pal, *Rev. Mex. Fis. S.* 53 (2007) 18-22.
- [72] V.M. Longo, L.S. Cavalcante, E.C. Paris, J.C. Sczancoski, P.S. Pizani, M.S. Li, J. Andres, E. Longo, J.A. Varela, *J. Phys. Chem. C*. 115 (2011) 5207-5219.
- [73] R. Lacomba-Perales, J. Ruiz-Fuertes, D. Errandonea, D. Martínez-García, A. Segura, *Eur. Phys. Lett.* 83 (2008) 37002-37006.
- [74] I.L. Validzic, T.D. Savic, R.M. Krsmanovic, D.J. Jovanovic, M.M. Novakovic, M.C. Popovic, M.I. Comor, *Mater. Sci. Eng. B*. 177 (2012) 645-651.
- [75] J. Ruiz-Fuertes, S. Lopez-Moreno, J. Lopez-Solano, D. Errandonea, A. Segura, R. Lacomba-Perales, A. Munoz, S. Radescu, P. Rodriguez-Hernandez, M. Gospodinov, L.L. Nagornaya, C.Y. Tu, *Phys. Rev. B*. 86 (2012) 125202-125211.
- [76] L.S. Cavalcante, V.M. Longo, J.C. Sczancoski, M.A.P. Almeida, A.A. Batista, J.A. Varela, M.O. Orlandi, E. Longo, M. Siu Li, *CrystEngComm*. 14 (2012) 853-868.
- [77] L.S. Cavalcante, M.A.P. Almeida, W. Avansi, Jr., R.L. Tranquilin, E. Longo, N.C. Batista, V.R. Mastelaro, M. Siu Li, *Inorg. Chem.* 51 (2012) 10675-10687.
- [78] L. Gracia, V.M. Longo, L.S. Cavalcante, A. Beltran, W. Avansi, M.S. Li, V.R. Mastelaro, J.A. Varela, E. Longo, J. Andres, *J. Appl. Phys.* 110 (2011)

043501-043512.

Chapter 5

Conclusions

Neste trabalho, formado por esses três artigos, pode-se concluir que:

Os calculos teóricos foram aplicados para fornecer informações que possam explicar o fenômeno da fotoluminescência. Com o método do DFT pode-se descrever os sistemas estudados por seus níveis de energia, densidade eletrônicas, estruturas de banda e densidades de estado através dos modelos de ordem-desordem.

Com relação ao CaMoO_4 , o material pode ser obtido experimentalmente com o método de hidrotermal/solvotermal com diferentes solventes, obtendo-se a fase pura.

As simulações teóricas e caracterizações experimentais mostraram defeitos intrínsecos no material com distorções nos clusters de $[\text{MoO}_4]$.

O espectros de UV-vis e as estruturas de bandas mostraram diferentes valores de band gap, associado a presença de níveis intermediários entre a banda de valência e a banda de condução, que são compostos basicamente pelos orbitais do oxigênios 2p e do molibdenios 4d, respectivamente.

Os calculos sugerem um gap direto de $(\Gamma - \Gamma)$, indicando que o sistema é bastante ordenado com poucas distorções nos clusters.

A análise do DOS indicaram a contribuição dos orbitais dos oxigênios 2p na banda de valência e os orbitais dos molibdênios 4d na banda de condução.

Os calculos da banda de estrutura e da densidade eletrônica mostraram que os estados eletrônicos são influenciados pelo deslocamento do átomo de Mo.

Sobre o MgTiO_3 , os filmes finos deste material pode ser preparados com sucesso pelo método de percusores poliméricos.

A estrutura de bandas mostraram gap indireto conferindo a diferentes tipos de defeitos do sistema, de modo a formar novos níveis eletrônicos relacionado ao efeito ordem e desordem.

Sintetizou-se com sucesso o $\beta\text{-ZnMoO}_4$ através do método de hidrotermal.

A estrutura de bandas mostrou um gap direto de Y para Y e os níveis de energia da banda de valência tem a contribuição dos oxigênios 2p e na banda de condução pelos orbitais do molibdênio 4d.

O mapa de densidade eletrônica mostra regiões não-homogêneas de densidade sobre os octaédricos distorcidos $[\text{MoO}_6]$ e $[\text{ZnO}_6]$. A PL pode ser explicada devido a distorções nos octaédricos, causando assim um defeito intrínscico da estrutura.

Chapter 6

Future perspective

Como perspectivas futuras, pode-se considerar que:

1. O estudo superficial do CaMoO_4 em diferentes planos de crescimentos e relacionar com os dados experimentais de morfologia estrutural;
2. O estudo com diferentes estados excitados (Singlete e Triplete) do CaMoO_4 e relacionar com o efeito ordem-desordem apresentado neste trabalho;
3. O estudo com dopagem do CaMoO_4 , substituindo-se o formador de rede Mo por W, fazendo para vários porcentagens de Mo e W na cela e comparando-se as propriedades óticas, eletrônicas e estruturais.

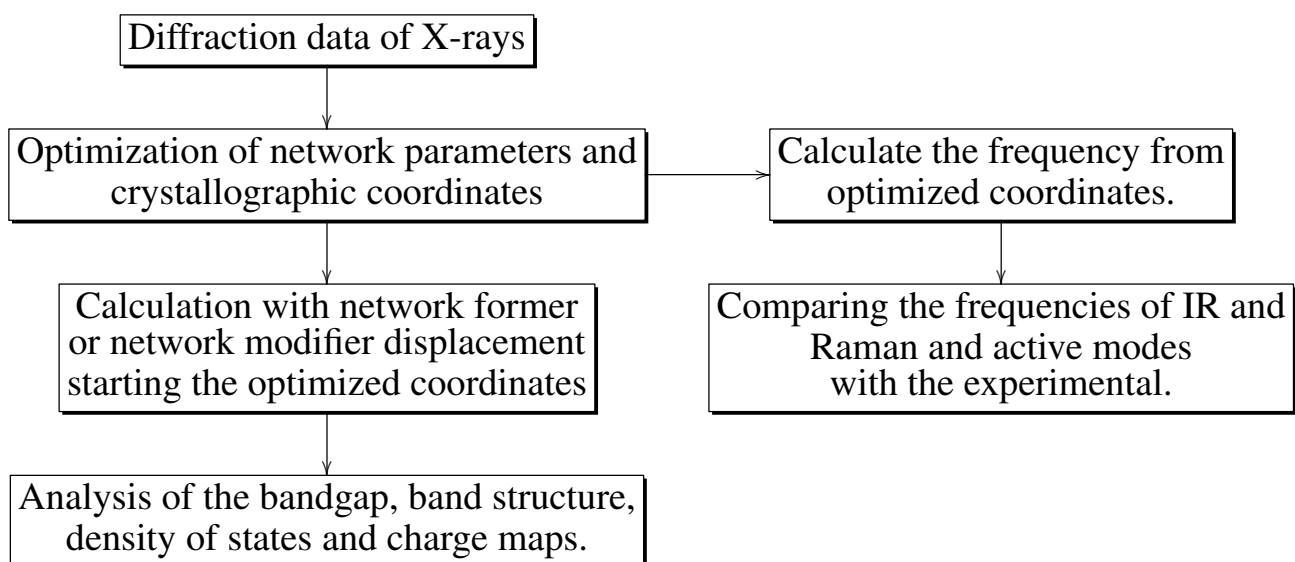
Bibliography

- [1] WHITESIDES,G.M.; "Nanoscience, Nanotechnology, and Chemistry".
Nanoscience and chemistry. v.1, n.2, p.172-179, 2005.
- [2] KLABUNDE,K.J. *Nanoscale Materials in Chemistry*. A John Wiley & Sons, Inc., Publication, 2001, p.1-7.
- [3] KAN,D.; TERASHIMA,T.; KANDA,R.;MASUNO,A.; TANAKA,K.; CHU,S.; KAN,H.; ISHIZUMI,A.; KANEMITSU,Y.; SHIMAKAWA,Y. and TAKANO,M.;"Blue-light emission at room temperature from Ar⁺-irradiated SrTiO₃".*Nature Materials*. v.4, p.816-819, 2005.
- [4] CAVALCANTE,L.S.; LONGO,V.M.; SCZANCOSKI,J.C.; ALMEIDA,M.A.P.; BATISTA,A.A.; VARELA,J.A.; ORLANDI,M.O.; LONGO,E. and LI,M.S.;"Electronic structure growth mechanism and photoluminescence of CaWO₄ crystal".*CrystEngComm*. v.14, p.853-868, 2012.
- [5] LONGO,E.; CAVALCANTE,L.S.; VOLANTI,D.P.; GOUVEIA,A.F.; LONGO,V.M.; VARELA,J.A.; ORLANDI,M.O. and ANDRÉS,J.;"Direct in situ observation of the electron-driven synthesis of Ag filaments on α -Ag₂WO₄ crystals".*Scientific Reports*. v. 3, n.1676, p.1-4, 2013.
- [6] SANTANA,Y.V.B.; GOMES,J.E.C; MATOS,L.; CRUVINEL,A.P.; PERRIN, A.; PERRIN, C.; ANDRÉS, J.; VARELA, J.A. and

- LONGO,E.;"Silver Molybdate and Silver Tungstate Nanocomposites with Enhanced Photoluminescence".*Nanomaterials and Nanotechnology*. v.4, n.22, p.1, 2014.
- [7] MONTOCELLO,F.; GUIDI,V.; MARTINELLI,G. and MALAGU,C.; MEINARDI,F.; "Near-infrared photoluminescence in titania: Evidence for phonon-replica effect".*Journal of Applied Physics*. v.94, n.3, p.1501-1505, 2003.
- [8] SOUZA,A.E.; SANTOS,G.T.A.; BARRA,B.C.; MACEDO,Jr.,W.D.; TEIXEIRA,S.T.; SANTOS,C.M.; SENOS,A.M.O.R.; AMARAL,L.; and LONGO,E.;"Photoluminescence of SrTiO₃: Influence of Particle Size and Morphology".*Crystal Growth & Design*. v.12, p.5671-5679, 2012.
- [9] BOMIO,M.R.D.; TRANQUILIN,R.L.; MOTTA,F.V.; PASKOCIMAS,C.A.; NASCIMENTO,R.M.; GRACIA,L.; ANDRÉS,J. and LONGO,E.;"Toward Understanding the Photocatalytic Activity of PbMoO₄ Powders with Predominant (111), (100), (011), and (110) Facets. A Combined Experimental and Theoretical Study".*The Journal of Physical Chemistry C*. v.117, p.21382-21395, 2013.
- [10] CHERMETTE,H.;"Density functional theory A powerful tool for theoretical studies in coordination chemistry".*Coordination Chemistry Reviews*. v.178-180, p.699-721, 1998.
- [11] DOVESI, V.R.S. et al., "CRYSTAL09 user's manual." 2009, University of Torino: Torino.
- [12] KROGER,F. and VINK,H.J.;"Relations between the Concentrations of Imperfections in Crystalline Solids". *Solid State Physics*. v.3, p.307-435, 1956.

Appendix A

Flowchart of the theoretical calculation of structures



Appendix B

Figures for the Supporting Information: Effect of different solvent ratios (water/ethylene glycol) on the growth process of CaMoO_4 crystals and its optical properties

FIGURE SI-1:

Viscosity of different solvent ratios ($\text{H}_2\text{O}/\text{C}_2\text{H}_6\text{O}_2$) employed in preparation of CaMoO_4 crystals.

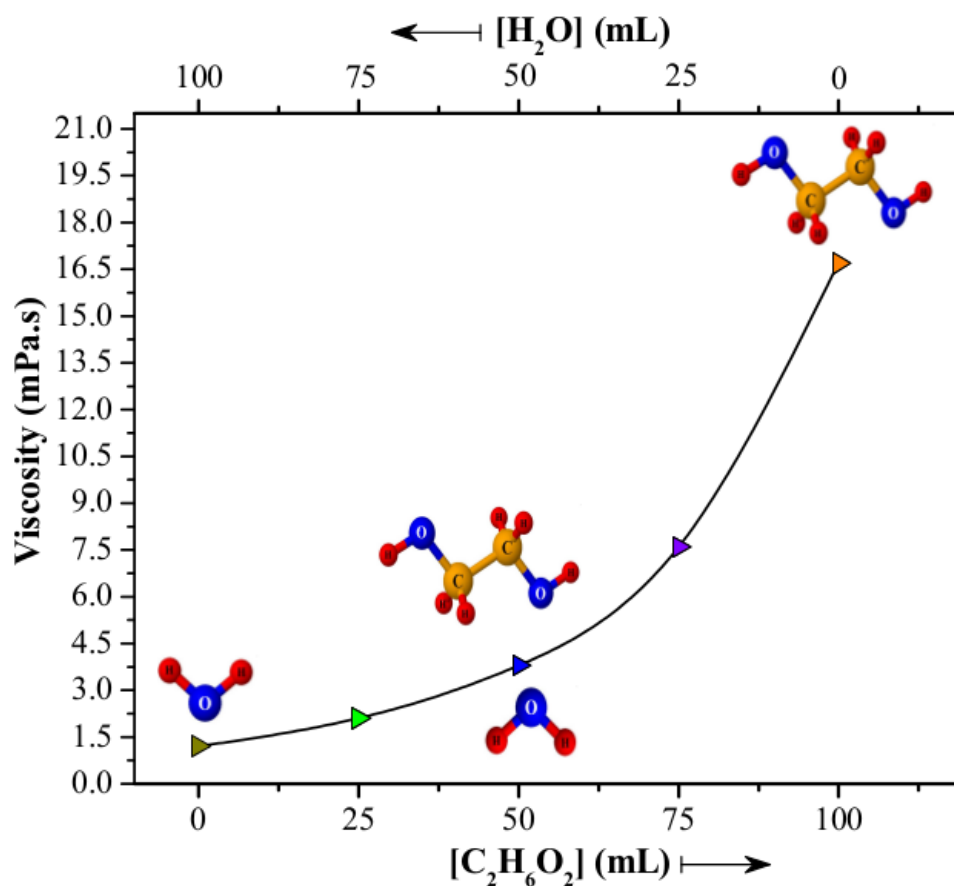


FIGURE SI-2:

Specific surface area of CaMoO_4 aggregated oriented, meso and nanocrystals prepared with different solvent ratios ($\text{H}_2\text{O}/\text{C}_2\text{H}_6\text{O}_2$) and processed in microwave-assisted hydrothermal/solvothermal system at 140°C for 1 h.

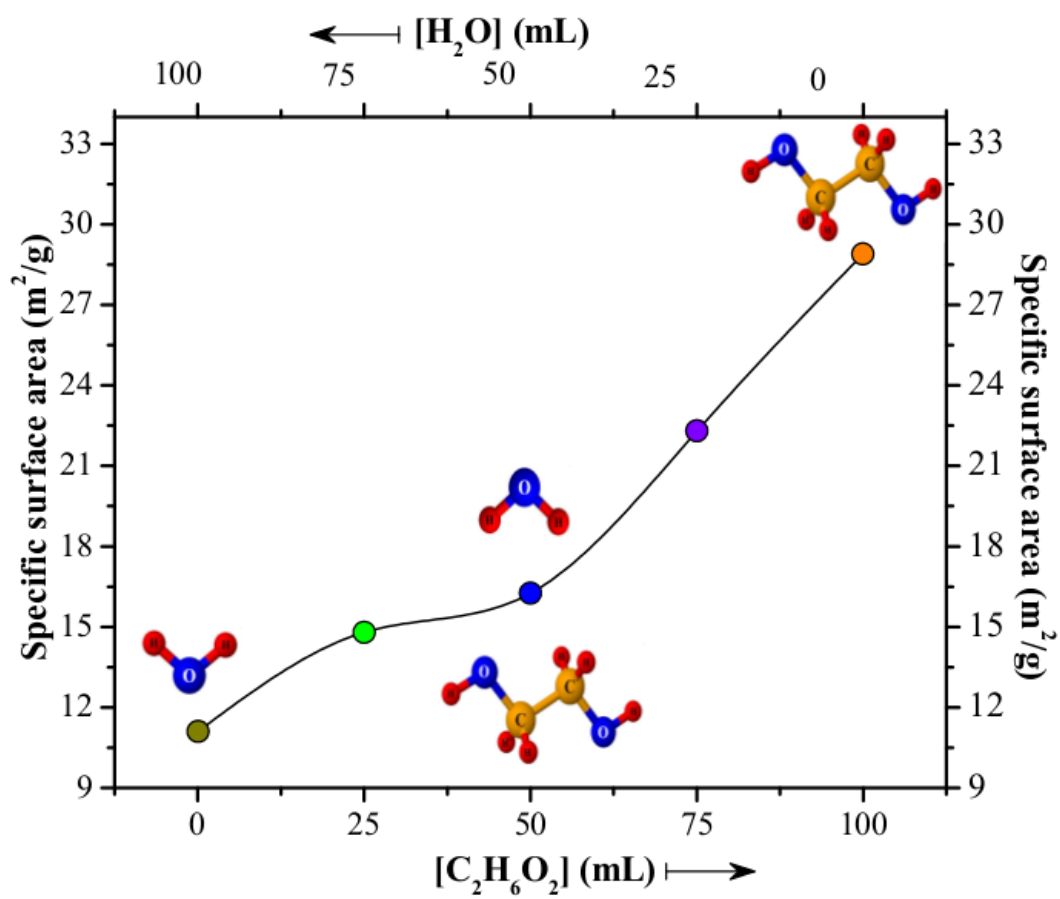


FIGURE SI-3(a-f):

N_2 adsorption-desorption isotherms of $CaMoO_4$ aggregated oriented, meso and nanocrystals prepared with different solvent ratios ($H_2O/C_2H_6O_2$) and processed in microwave-assisted hydrothermal/solvothermal system at $140^\circ C$ for 1 h.

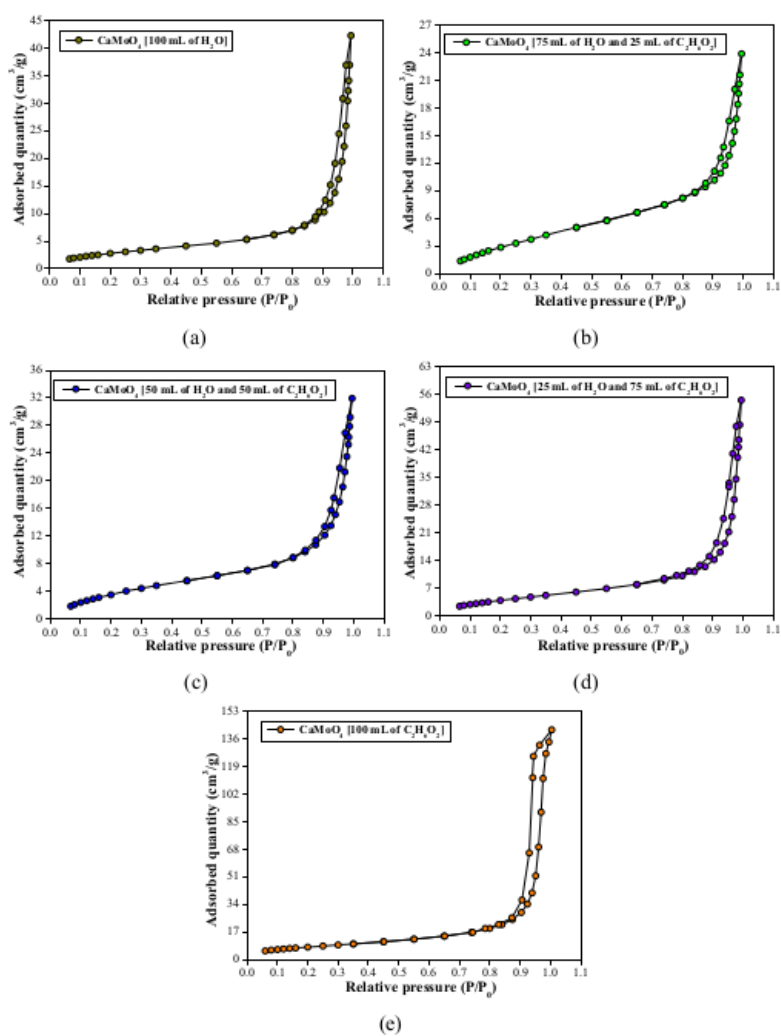


FIGURE SI-4(a-l):

TEM/HR-TEM micrographs and SAED of CaMoO_4 oriented aggregate, meso and nanocrystals prepared with different solvent ratios and processed in microwave-assisted hydrothermal/solvothermal system: (a-d) 100 mL of H_2O , (e,f) 75 mL of H_2O and 25 mL of $\text{C}_2\text{H}_6\text{O}_2$, (g,h) 50 mL of H_2O and 50 mL of $\text{C}_2\text{H}_6\text{O}_2$, (i,j) 25 mL of H_2O and 75 mL of $\text{C}_2\text{H}_6\text{O}_2$ and (k,l) 100 mL of $\text{C}_2\text{H}_6\text{O}_2$.

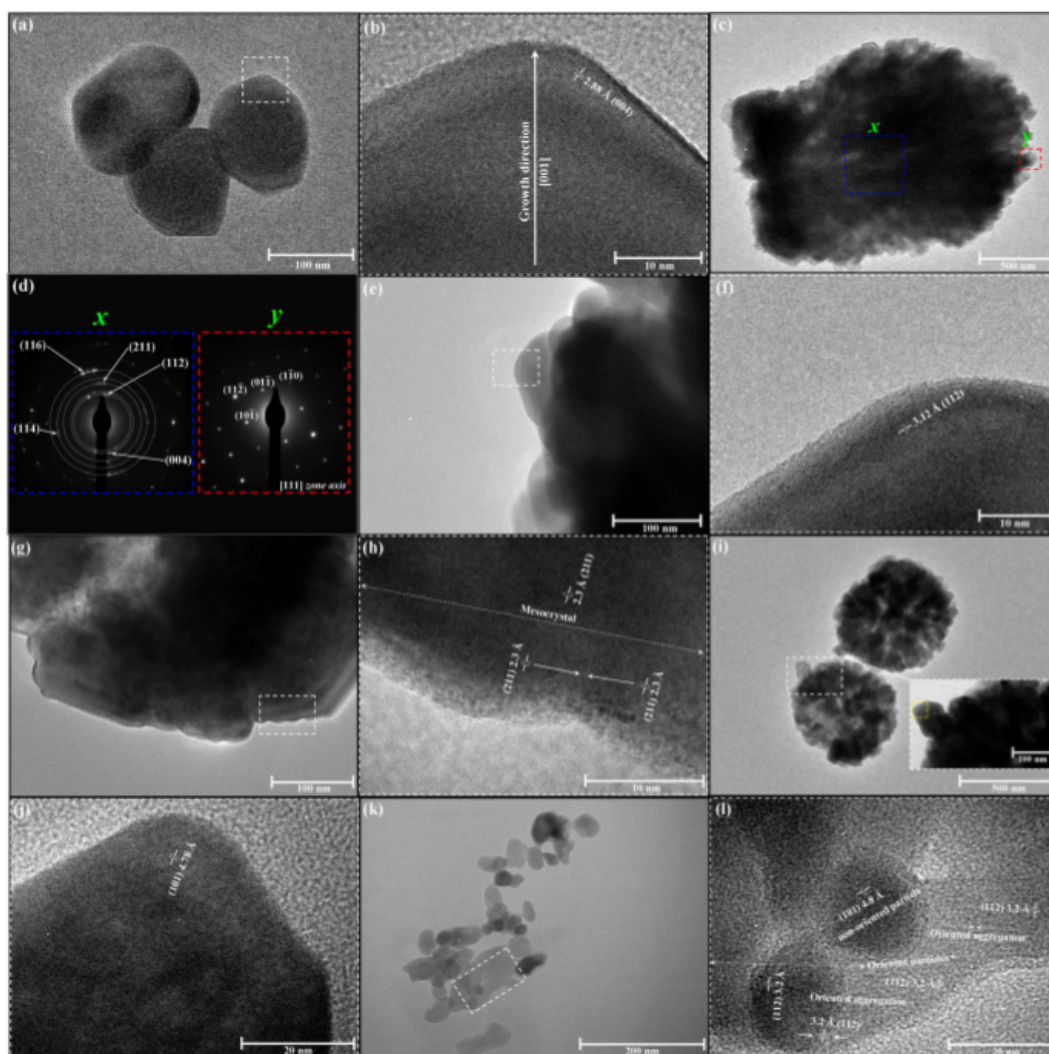


FIGURE SI-5(a-c):

Schematic representation of CaMoO_4 (a) oriented aggregate, (b) meso and (c) nanocrystals and possible relation of orientation of crystals with the photoluminescence properties. Insets shows the digital photos of crystals exhibited photoluminescence at room temperature when excited by laser ($\lambda = 350 \text{ nm}$).

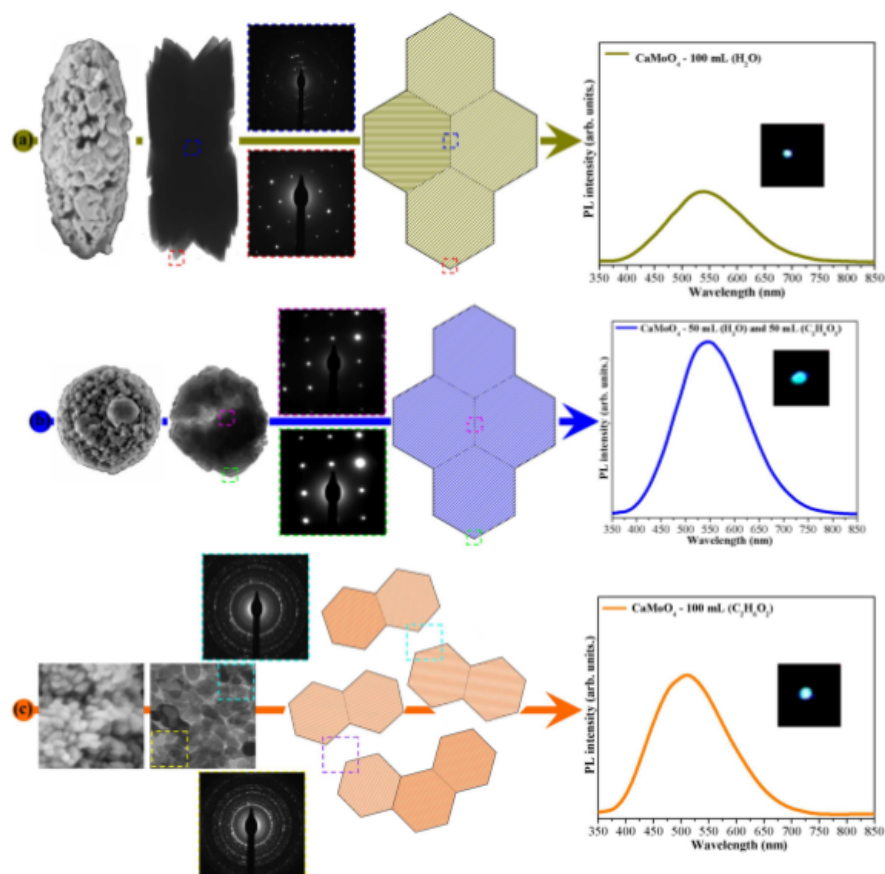


FIGURE SI-6:

Diagram of the primitive body-centered-tetragonal Brillouin zone.

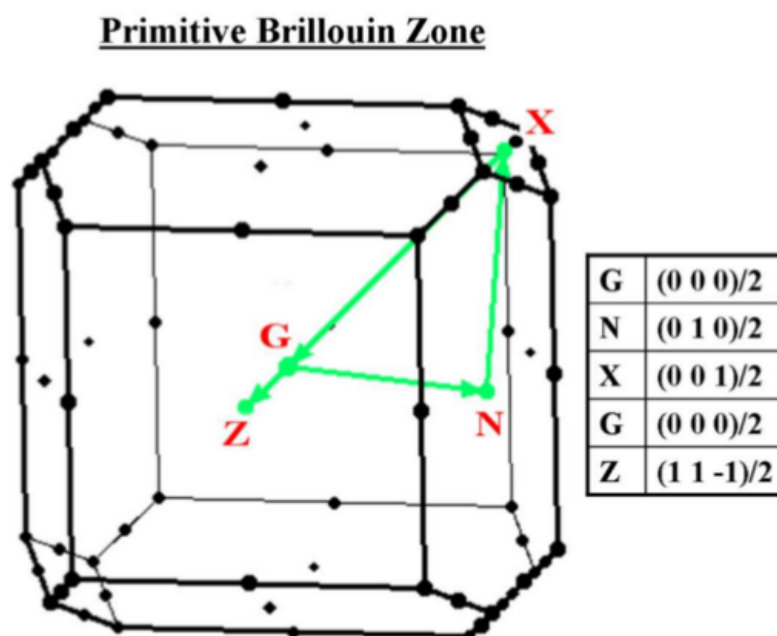


FIGURE SI-7:

Correlation of the experimental gap energy [$E_{gap(exp)}$] with the theoretical gap energy [$E_{gap(theo)}$] after the displacement of Mo atoms to deform the CaMoO_4 crystal.

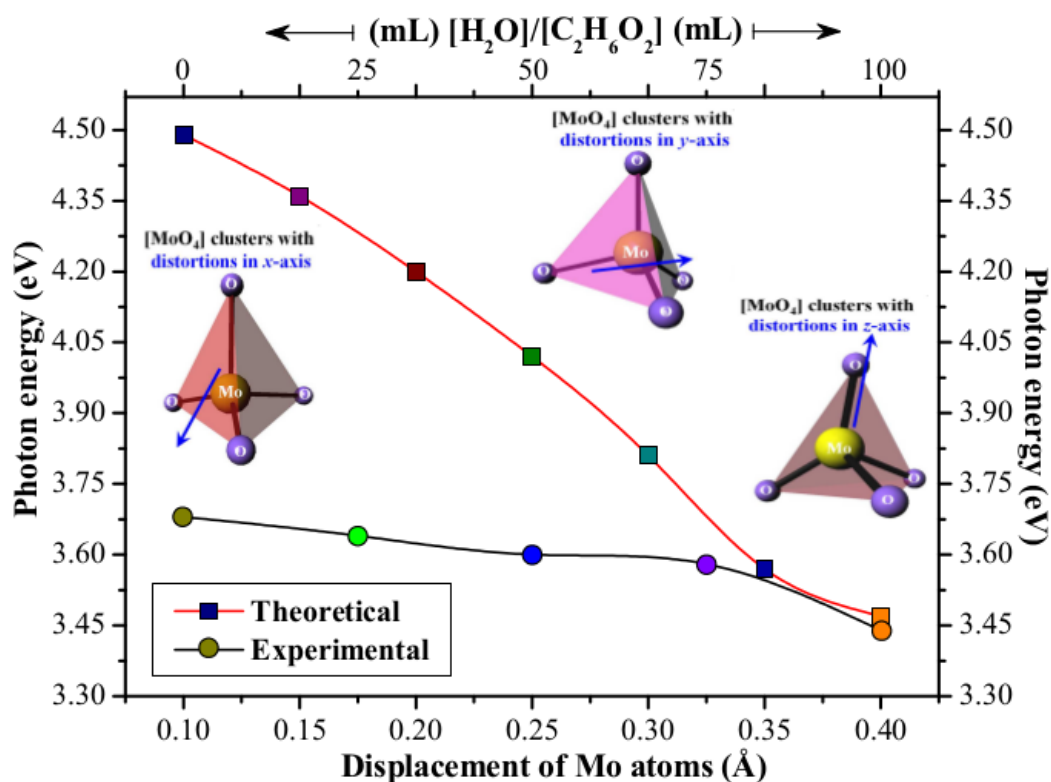


FIGURE SI-8:

DOS partial and total for each one of main atoms orbitals involved (Ca = 5s, 5p, Mo = 4d and O = 2p) of crystalline CaMoO₄ (a-c) without displacement on the Mo atoms.

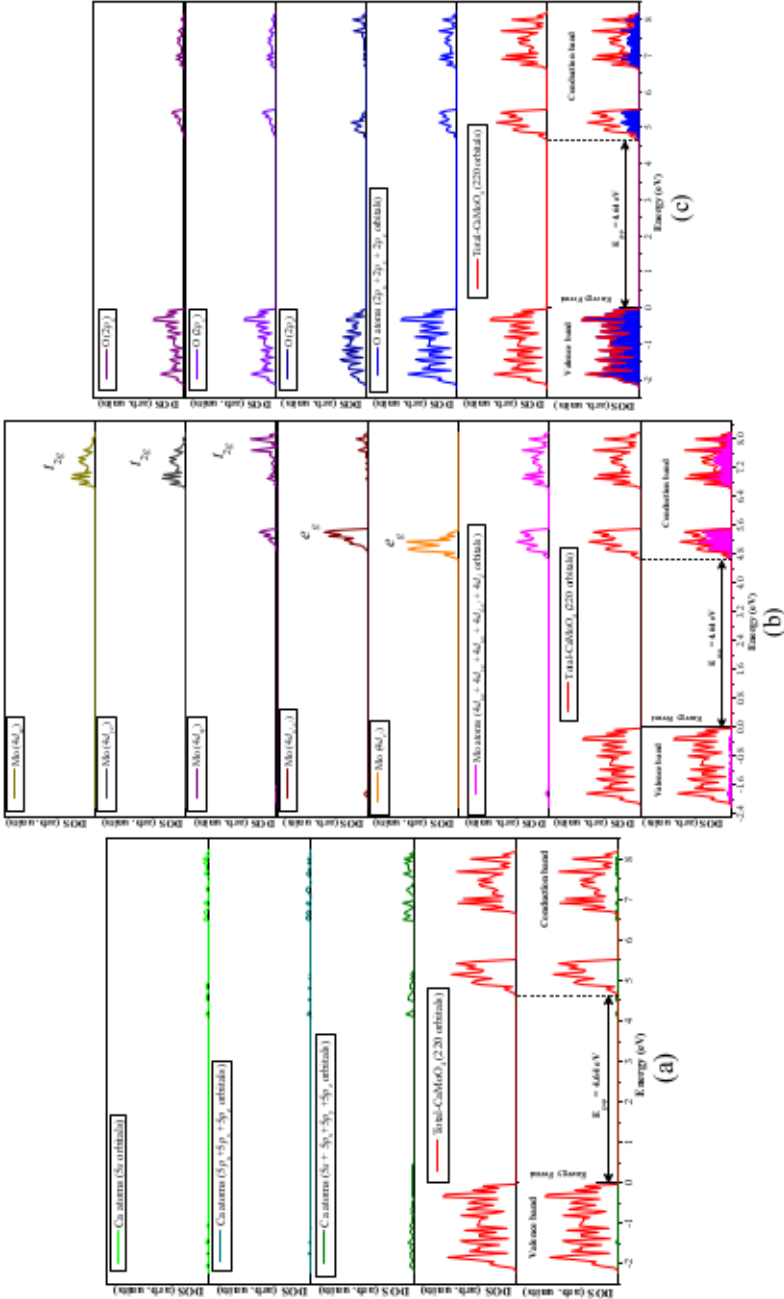
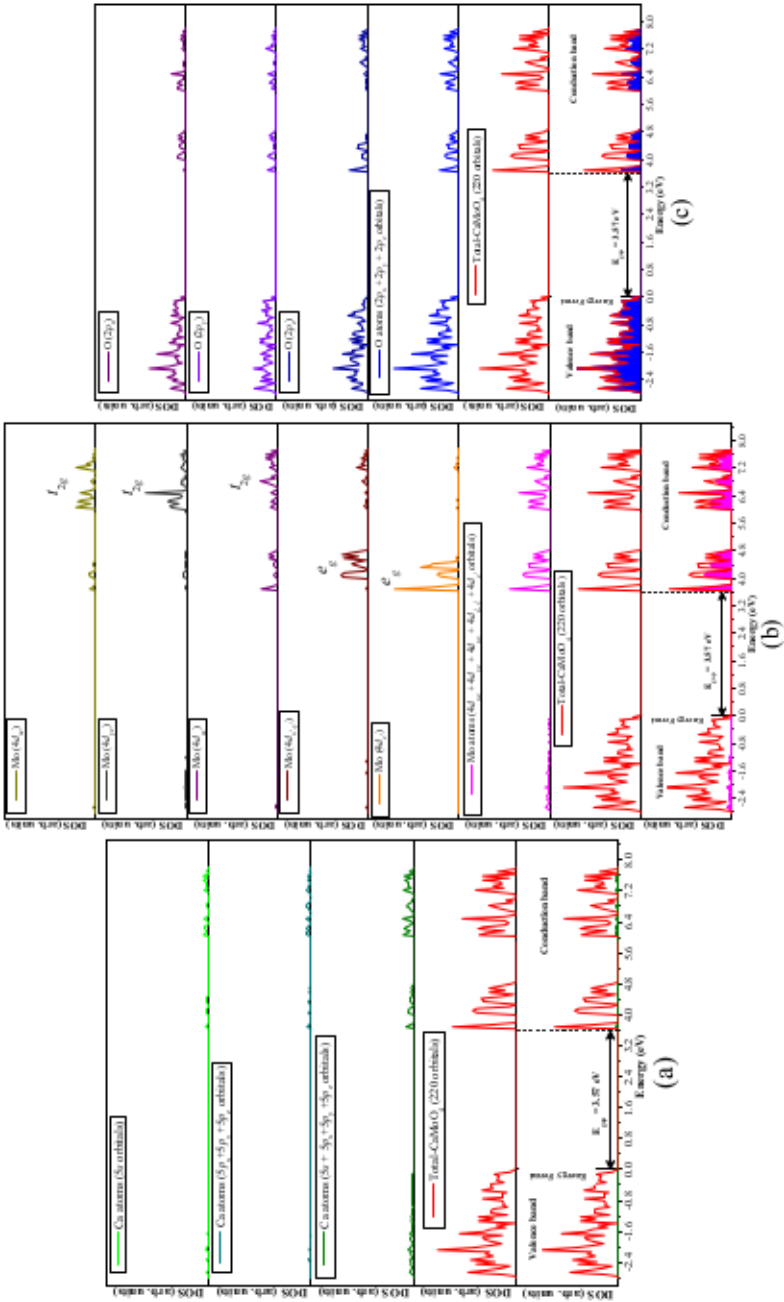


FIGURE SI-9:

DOS partial and total for each one of main atomics orbitals involved (Ca = 5s, 5p, Mo = 4d and O = 2p) of crystalline CaMoO₄ (a-c) with displacement of 0.35 Å on the Mo atoms.



Appendix C

Support Information: A combined theoretical and experimental study of electronic structure and optical properties of β -ZnMoO₄ microcrystals

Table C.1: Positions of active Raman-modes (experimental and theoretical)

Types of Raman-active modes	Specific positions of the experimental Raman-active modes from Raman spectrum (cm ⁻¹)	Calculated theoretically positions of the Raman-active modes from optimized electronic structure (cm ⁻¹)
B _g	95	103.5849
B _g	124	148.2214
A _g	172.4	150.881
B _g	191	186.1143
B _g	215	201.0578
A _g	223	219.1623
B _g	261	273.4511
A _g	268	277.8639
B _g	308	318.4282
A _g	333	321.3496
B _g	356	356.5429
A _g	393.3	415.5936
B _g	501	494.3778
A _g	522	520.5548
B _g	662	646.8233
A _g	701	692.8771
B _g	778	789.4412
A _g	877.6	887.4072

Table C.2: Positions of active IR-modes (experimental and theoretical)

Types of IR-active modes	Specific positions of the experimental IR-active modes from Raman spectrum (cm^{-1})	Calculated theoretically positions of the IR-active modes from optimized electronic structure (cm^{-1})
B_u	-	131.1691
B_u	-	168.419
A_u	-	178.2958
B_u	-	236.0248
B_u	257.14	266.022
B_u	-	285.2579
A_u	326.1	326.9627
A_u	359.03	335.8099
A_u	409.78	414.4855
B_u	453.18	445.3095
A_u	516.52	508.0691
B_u	-	544.1914
A_u	639.91	651.0359
B_u	711.68	774.8547
A_u	830.91	824.6096